Altered Morphology of YFP-Expressing Neurons In a Rett Syndrome Mouse Model

by

David P. Stuss
B.Sc. (Hons.), University of Victoria, 2005

A Thesis Submitted in Partial Fulfillment

MASTER OF SCIENCE

in the Department of Biology

© David P. Stuss, 2009
University of Victoria

All rights reserved. This thesis may not be reproduced in whole or in part, by photocopy or other means, without the permission of the author.

Supervisory Committee

Altered Morphology of YFP-Expressing Neurons In a Rett Syndrome Mouse Model

by

David P. Stuss
B.Sc. (Hons.), University of Victoria, 2005

Supervisory Committee

Dr. Kerry R. Delaney, Department of Biology
Supervisor

Dr. Robert L. Chow, Department of Biology
Departmental Member

Dr. Perry L. Howard, Departments of Biology and Biochemistry/Microbiology
Departmental Member

Abstract

Supervisory Committee

Dr. Kerry R. Delaney, Department of Biology
Supervisor

Dr. Robert L. Chow, Department of Biology
Departmental Member

Dr. Perry L. Howard, Departments of Biology and Biochemistry/Microbiology
Departmental Member

Rett Syndrome (RTT, OMIM 312750) is a pervasive autism spectrum disorder affecting 1 in 10,000 females. The majority of cases are caused by mutations in the X-linked gene *MECP2*. The RTT phenotype appears to be caused by impaired synapse maturation or maintenance, resulting in disrupted autonomic nervous system function, mental retardation, ataxia, apraxia, and movement stereotypies. While not a neurodegenerative disorder RTT is marked by region-specific reductions in brain volume. We examined the morphology of YFP-expressing Layer 5 pyramidal neurons in the motor cortex of a MeCP2 mutant RTT mouse model. Mutant mice exhibited smaller somata and reduced dendritic lengths in both the apical tuft and basal arbor. Basal dendritic branching was also reduced proximal to the soma. These changes are consistent with the motor deficits observed in mutant mice and in human RTT patients. Altered expression of a *Thy-1-YFP* reporter transgene in MeCP2 mutant mice is also described.

Table of Contents

List of Tables

List of Figures

Acknowledgments

I would like to thank Dr. Kerry Delaney for inviting me to join his lab and for his generous provision of support and resources for this thesis. The Rett Syndrome Research Foundation, Canadian Institutes of Health Research, and Michael Smith Foundation for Health Research provided funding support and training opportunities. My committee members, Drs. Bob Chow and Perry Howard, provided valuable suggestions and encouragement throughout. Special thanks to Dr. Chow for providing liberal use of his confocal microscope, the principal tool of my thesis work. Dr. Diana Varela also provided generous use of her inverted fluorescence microscope. Dr. David Levin provided support in the early phases of the project. Many people were involved in a technical capacity over the course of the project, including Kat Betke, Emilie Bousquet, Glen Manders, Daylin Mantyka, Amber Mjolsness, Maria Popova, Lindsay Richier, Richard Taylor, Jennifer Thompson, and Ian Wrohan; thank you all for your hard work. Dr. Jamie Johnston, Dr. Tom Money, Tom Harrison, and Ian Swan all contributed valuable suggestions and camaraderie. Finn Hamilton provided some critical statistical help and wrote the statistical code used in the appendix. Last, and very far from least, I'd like to thank Dr. Jamie Boyd, without whose programming skills this thesis would not have come to fruition.

Dedication

This thesis is dedicated to my parents, Don and Kaaren, for their unfaltering support, and to Dr. Don Dedrick and Dr. Jamie Doran for the remarkable encouragement they provided along the way.

Chapter 1: Introduction

Overview of Rett Syndrome

Rett Syndrome (RTT, OMIM 312750) is a pervasive developmental autism spectrum disorder first identified in 1966 by the clinician Andreas Rett and brought to international attention two decades later (Rett, 1966; Hagberg *et al.*, 1983; Hagberg *et al.*, 1985). RTT primarily affects females at a rate of 1 in 10 000, and patients are characterized as having classical or atypical RTT, depending on the timing and range of symptoms present. In classical RTT, clinical presentation proceeds through a sequence of stages and includes a broad and complex range of symptoms. Inclusion criteria for RTT diagnosis include normal appearance and development during infancy followed by reduction or loss of purposeful movement, reduced or lost speech and communication ability, mental disability, social withdrawal, ataxia, and distinctive stereotyped hand movements. Supportive criteria include breathing irregularities, seizures, bruxism, scoliosis, emotional disturbance, gastrointestinal dysfunction, and impaired nociception, among other symptoms (Hagberg, 2002; Trevathan and Naidu, 1988). Even though RTT is the second most common cause of severe mental retardation in females after Down's Syndrome, its recognition was complicated by the highly variable clinical presentation observed between individuals, in terms of both variety and severity (Hagberg, 1995).

The clinical features of the RTT phenotype are indicative of a neurological disorder, and neuroanatomical studies show alterations at both organ and cellular levels. The brains of RTT patients have been characterized as developmentally arrested at approximately one year of age (Armstrong, 2001). At the tissue level, multiple MRI studies have shown reductions in volumes of both gray matter and white matter (Casanova *et al.*, 1991; Subramaniam *et al.*, 1997; Naidu *et al.*, 2001; Saywell *et al.*, 2006). Reductions in white matter are globally uniform, but gray matter is affected in a region-dependent manner. Occipital cortex is consistently preserved, while the largest decreases in cortical volume occur in frontal regions. Frontal cortex is also unique among brain areas in that reductions in volume are correlated with measures of clinical severity (Carter *et al.*, 2008). Most studies have not found evidence of progressive degeneration, with the

exception of an age-dependent atrophy of the cerebellum (Murakami *et al.*, 1992). The reductions in brain volume are not due to neurodegeneration, however, but appear to arise from increased neuronal density caused by reduced soma size and dendritic arborization. Post-mortem studies of RTT patient brain tissue found selective reductions in dendritic branching in Layers 2/3 and 5 of frontal and motor cortex, as well as fewer dendritic spines (Belichenko *et al.*, 1994; Armstrong *et al.*, 1995; Bauman *et al.*, 1995a; Belichenko and Dahlstrom, 1995; Belichenko *et al.*, 1997; Armstrong *et al.*, 1998). As with MRI studies, no progressive degeneration was evident. Collectively, these structural changes are coherent with the motor, social, and attention-related deficits observed in RTT patients.

The Role of MeCP2 in RTT

In females with classical RTT, greater than 96% of cases are associated with mutations in the X-linked gene *MECP2* (methyl CpG-binding protein 2) (Amir *et al.*, 1999; Neul *et al.*, 2008). Consistent with the range and degree of symptom variability characteristic of RTT, the emerging picture of the role of MeCP2 in the nervous system is one of complex functional heterogeneity. This picture is far from complete, but has thus far been shown to involve multiple protein functions, dynamic regulation, and cell type-specific regulatory effects on gene expression. A further layer of complexity in the study of this disorder arises from the contributions of mutation type, X-chromosome inactivation, and modifier genes to the RTT phenotype.

Structure, Function, and Expression Patterns of MeCP2

MeCP2 belongs to a family of chromatin-associated vertebrate proteins sharing a highly conserved methyl-CpG-binding domain (MBD), which is necessary and sufficient for DNA binding (Nan *et al.*, 1993; Wakefield *et al.*, 1999; Ballestar and Wolffe, 2001). The *MECP2* gene encodes two transcripts, *MECP2_e1* and *MECP2_e2* (previously termed *MECP2B/Mecp2*α and *MECP2A/Mecp2*β in humans/mice, respectively) (Kriaucionis and Bird, 2004; Mnatzakanian *et al.*, 2004). *MECP2_e1* encodes a 498 amino acid (AA) protein and *MECP2_e2* encodes a 486 AA protein which differ in a short N-terminal sequence only, and otherwise share a nuclear localization signal (Nan *et al.*, 1996) and

all known functional domains (Fig. 1). In addition to the N-terminal MBD, these include a central transcriptional repressor domain (TRD) (Nan *et al.*, 1997), a C-terminal domain that aids in DNA-binding (Chandler *et al.*, 1999), and a WW domain that allows MeCP2 to participate in a number of protein-protein interactions (Buschdorf and Stratling, 2004). There are eight potential phosphorylation sites in or near these domains. Three have been shown to participate in neuronal activity-dependent phosphorylation, altering chromatin binding, nuclear translocation, and transcriptional control of target genes (Chen *et al.*, 2003; Miyake and Nagai, 2007; Chao and Zoghbi, 2009; Tao *et al.*, 2009; Zhou *et al.*, 2006). The structure of MeCP2 therefore has multifunctional potential and may undergo complex functional regulation.

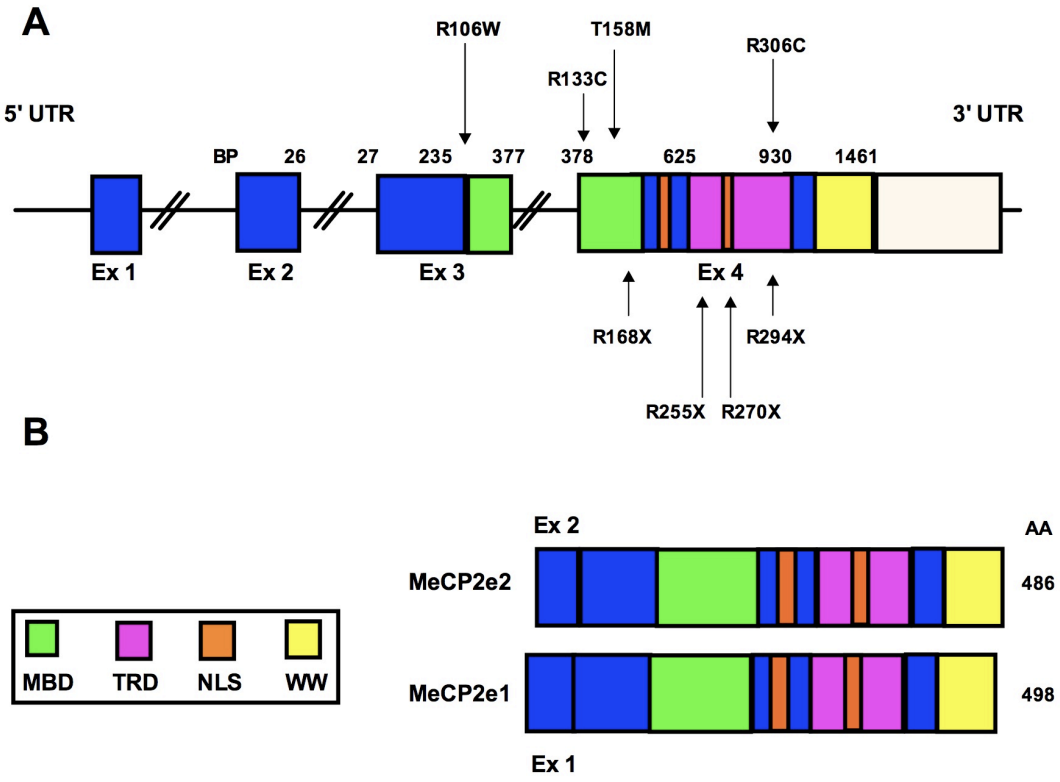

Figure 1. *MECP2* gene and protein isoforms.

A) The four-exon gene structure of *MECP2* showing the eight most common mutations in RTT females. B) The two protein isoforms are generated by alternative splicing in the N-terminal sequence. AA, amino acid; BP, base pair; Ex, exon; MBD, methyl-CpG-binding domain; TRD, transcription repression domain; NLS, nuclear localization signal; UTR, untranslated region; WW, WW domain; X, stop codon. Adapted from Bienvenu and Chelly (2006).

MeCP2 is distinct among the MBD-containing proteins in that it can bind a single symmetrical pair of methylated CpG dinucleotides (Lewis *et al.*, 1992). These dinucleotides are found in CpG-rich DNA sequences, called CpG islands, that preferentially occur near gene promoters (Gardiner-Garden and Frommer, 1987; Fatemi *et al.*, 2005). MeCP2 derives further target site binding selectivity based on the presence of adjacent A/T sequences {Klose 2005}. Early *in vitro* studies found that MeCP2 functions as a global transcriptional silencer that represses transcription after binding DNA distant from the transcription start site (Lewis *et al.*, 1992; Kaludov and Wolffe, 2000). Transcriptional silencing involves the Sin3a corepressor complex, which has a non-obligate interaction with the MeCP2 TRD and which mediates silencing by recruiting histone deacetylases (Jones *et al.*, 1998; Nan *et al.*, 1998; Kokura *et al.*, 2001; Klose and Bird, 2004). MeCP2 also binds non-methylated DNA (Nan and Bird, 2001), however, and more recent studies show that it binds promoter regions directly, both upregulating and downregulating gene expression, albeit in subtle ways (Chahrour *et al.*, 2008; Urdinguio *et al.*, 2008; Ben-Shachar *et al.*, 2009). Beyond transcriptional regulation, MeCP2 has also been shown to interact with mRNA splicing factors, and altered alternative splicing has been observed in a *Mecp2* mutant mouse model of RTT (Buschdorf and Stratling, 2004; Young *et al.*, 2005). This is of particular significance in CNS-based disorders because of the high degree of alternative splicing in ion channel and neurotransmitter receptor mRNAs, which alters their biophysical and regulatory properties (O'Donovan and Darnell, 2001).

MECP2 is ubiquitiously transcribed in all tissues, and is particularly abundant in the brain (Lewis *et al.*, 1992; Shahbazian *et al.*, 2002b; LaSalle *et al.*, 2001). The expression levels of the two isoforms varies with tissue type, with MeCP2_e1 being the more abundant isoform in the CNS (Kriaucionis and Bird, 2004). MeCP2 is detected most strongly in neurons, but also occurs in glia at much lower levels (Aber *et al.*, 2003; Ballas *et al.*, 2009; Maezawa *et al.*, 2009). As expected for a DNA-binding protein, MeCP2 staining is concentrated in the nucleus, but it is also detected in the perikaryon and post-synaptic compartment (Nan *et al.*, 1996; Aber *et al.*, 2003). In human brains, neurons fall into two distinctive groups, expressing either a high or low level of MeCP2 that varies by brain

region and cortical layer (LaSalle *et al.*, 2001; Mullaney *et al.*, 2004). The MeCP2_e1 isoform predominates in high-expressing cells (Samaco *et al.*, 2004). The relative levels of MeCP2 protein and RNA are poorly correlated across tissues, which suggests that the mRNA is post-transcriptionally regulated by tissue-specific factors (Reichwald *et al.*, 2000; Shahbazian *et al.*, 2002b). One likely mechanism is alternative polyadenylation of the 3'UTR, which results in four transcripts (1.8, 5, 7.2, 10.2 kb) that are differentially expressed in different tissue and cell types (D'Esposito *et al.*, 1996; Coy *et al.*, 1999; Balmer *et al.*, 2003). These transcripts have probable functional significance because several subregions of the 3'UTR are highly conserved across vertebrate species (Coy *et al.*, 1999). MeCP2 also appears subject to variable post-transcriptional regulation. MeCP2 contains multiple ubiquitinylation sites and two PEST sequences, which confer a predisposition to rapid proteolytic degradation (Thambirajah *et al.*, 2009). A functionally significant phosphorylation site resides within the C-terminal PEST sequence, suggesting the possibility of dynamic regulation of protein turnover. MeCP2 thus appears to be subject to multiple regulatory influences at a variety of pre- and post-translational levels (Samaco *et al.*, 2004).

The predominantly postnatal developmental timing of MeCP2 expression correlates with CNS maturation, and is region- and cell-specific. MeCP2 is first detected in the spinal cord and brain stem, and only later in cortex, hippocampus and cerebellum (Shahbazian *et al.*, 2002b; Mullaney *et al.*, 2004). Expression also parallels the developmental sequence of cortical laminae. In the cerebellum, where cell types can be discerned by well-defined morphologies and laminar locations, MeCP2 shows a cell-specific developmental pattern that is coincident with the initiation of synapse formation for each neuronal class (Mullaney *et al.*, 2004). MeCP2 does not appear to play any significant roles in neuronal specification, proliferation, or migration, but rather with postmigratory maturation, a period in which neurons are establishing the axonal projections, dendritic architectures, and synaptic connections critical to normal circuitry (Kishi and Macklis, 2004).

MeCP2 and Dysregulated Gene Expression in RTT

Current data suggest that the principal biological role of MeCP2 is the modulation of gene expression, in a manner concordant with its heterogeneity of expression and complex regulation. While early hypotheses proposed that RTT was a disorder of wide-scale transcriptional derepression in the CNS (Amir *et al.*, 1999; Nan and Bird, 2001), global gene-expression and proteomics studies found very few large and reproducible differences between normal and MeCP2-mutant brains (Traynor *et al.*, 2002; Tudor *et al.*, 2002; Matarazzo and Ronnett, 2004; Jordan *et al.*, 2007; Urdinguio *et al.*, 2008). One explanation for this is that MeCP2 mutation may not result in global loss of transcriptional repression due to redundancy and/or compensation by other methyl-CpG-binding proteins (Hendrich and Bird, 1998; Jorgensen and Bird, 2002). Alternately, the RTT phenotype could be expected to arise from either 1) the net impact of many mild effects in large numbers of genes, or 2) larger effects in restricted sets of genes that are differentially expressed in different cell types. Although redundancy and compensation effects have not been conclusively ruled out, evidence is emerging that supports both of the latter scenarios. Subsequent studies examining more precisely fractionated brain regions, such as the hypothalamus and cerebellum, indicate that MeCP2 acts as both a repressor and activator of gene expression, frequently with direct promoter interactions (Chahrour *et al.*, 2008; Ben-Shachar *et al.*, 2009). In the hypothalamus, expression of greater than 2100 genes (~85% of the total tested) was dysregulated, and nearly 500 of these overlapped with genes affected in the cerebellum. In all cases, misexpression was not greater than five-fold, with most gene expression altered by 50% or less. These differences may be even more dramatic if the resolution of fractionation is increased to include isolated cellular subpopulations within brain regions, as has already been demonstrated within the forebrain of normal adult mice (Sugino *et al.*, 2006). The heterogeneity of the gene-modulatory effects of MeCP2 appears necessary but not sufficient to account for range and variability of RTT symptoms, however. Three principal explanations exist to account for this phenomenon in human RTT patients: the effects of specific mutations, skewed X-inactivation, and the activity of modifier genes.

Over 200 mutations in MeCP2 have been documented, but eight common mutations account for 60% of RTT cases[1] (Fig. 1) (Miltenberger-Miltenyi and Laccone, 2003; Neul *et al.*, 2008). Point, frame shift, and nonsense mutations as well as truncating deletions have all been documented (Weaving *et al.*, 2003). The expansion of databases correlating *MECP2* genotype with phenotype (e.g. RettBASE) has allowed clinicians to correlate specific mutations with symptom pattern and severity (Christodoulou *et al.*, 2003; Christodoulou and Weaving, 2003; Fyfe *et al.*, 2003). Large deletions and mutations in the MBD tend to produce the most severe symptoms. Interestingly, specific mutations occasionally produced bimodal (mild and severe) effects in different symptoms, such as hand use, language use, and ambulation; one mutation was shown to selectively affect language capacity (Neul *et al.*, 2008). This work suggests that the different domains of MeCP2 may mediate dissociable and discrete functional roles. It should be noted, however, that the presence of *MECP2* mutation alone does not predict RTT; some carriers are virtually asymptomatic, while others have related disorders including autism, non-specific mental retardation, congenital encephalopathy, and Angelman-like syndrome (Carney *et al.*, 2003; Couvert *et al.*, 2001; Hitchins *et al.*, 2004; Hoffbuhr *et al.*, 2002; Shibayama *et al.*, 2004; Watson *et al.*, 2001; Zappella *et al.*, 2003).

MECP2 maps to Xq28 on the X chromosome and is subject to random X-chromosome inactivation (XCI), and consequently expression of the mutant gene is mosaic in female patients (Adler *et al.*, 1995; D'Esposito *et al.*, 1996; Sirianni *et al.*, 1998). XCI is the process in female mammals by which one of two X-chromosomes is randomly compacted into transcriptionally silent heterochromatin at the pre-implantation blastocyst stage, equalizing X-linked gene expression to that occurring in males (Chow *et al.*, 2005). XCI has also been proposed to explain the variable severity of RTT symptoms, which can even be observed in monozygotic twins having identical mutations (Zoghbi *et al.*, 1990; Schanen *et al.*, 2004). Skewed X-inactivation (defined as >80% inactivation of one MeCP2 allele in heterozygous females) appears to occur at a higher incidence in RTT than in control groups, and studies in mice indicate an apparent bias towards expression of the WT allele (Amir *et al.*, 2000; Bienvenu *et al.*, 2000; Hoffbuhr *et al.*, 2001; Young

[1]These are R106W, R133C, T158M, R168X, R255X, R270X, R294X, R306C.

and Zoghbi, 2004; Huppke *et al.*, 2006; Bao *et al.*, 2004). Early studies indicated that, in classic RTT, XCI had a more prominent effect on clinical severity than mutation type. As correlative genotype-phenotype databases have expanded, however, it now appears that the reverse is true, particularly when the full range of symptom presentations seen in both atypical and classical RTT are considered (Amir *et al.*, 2000; Shahbazian and Zoghbi, 2001; Neul *et al.*, 2008). The limited role of XCI is further emphasized by the range of phenotypic severity observed in males hemizygous for *MECP2* mutations. While these males do not fit the full set of diagnostic criteria that define RTT, and their symptoms are generally much more severe, they fall into three clinically distinct groups, defined as severe congenital encephalopathy, Rett-like syndrome, or mild to severe mental retardation (Bienvenu and Chelly, 2006). Thus, several lines of evidence suggest that XCI is not the principal cause of symptom variability in RTT.

The action of modifier gene alleles also appears to exacerbate or attenuate the effects of MeCP2 mutation. Healthy female carriers of *MECP2* mutations have been shown to exhibit either normal or highly positively skewed XCI, and mutations normally producing severe phenotypes can have mild effects even in the presence of balanced XCI skewing (Renieri *et al.*, 2003). Although this is a very recent area of investigation, there is evidence for influence by modifier genes. A common polymorphism in the BDNF (brain-derived neurotrophic factor) gene, which is itself regulated by MeCP2 (Chen *et al.*, 2003), has been shown to affect RTT symptom severity (Zeev *et al.*, 2009). A study in *Drosophila* demonstrated that several chromatin remodelling genes and Sin3a corepressor complex homologues could either compensate for or ameliorate abnormal phenotypes caused by MeCP2 overexpression (Cukier *et al.*, 2008). These emerging studies are of particular significance for RTT research using animal models, and emphasize the need for genetically well-characterized lines.

Mouse Models of RTT

Several lines of *Mecp2* mutant mice have been developed that have proven instrumental in elucidating the full complexity of the mechanisms underlying RTT. To date, three are commonly used, from the labs of Adrian Bird, Rudolph Jaenisch, and Huda Zoghbi

(Chen *et al.*, 2001; Guy *et al.*, 2001; Shahbazian *et al.*, 2002a). All recapitulate the RTT phenotype with varying degrees of severity, reflecting the range of symptoms observed in human patients. Symptoms include reduced brain volume, disordered breathing, seizures, gait ataxia, and hindlimb clasping, as well as cognitive, memory, and social learning deficits (Chen *et al.*, 2001; Guy *et al.*, 2001). For unknown reasons, in most respects the effects of *Mecp2* mutation are milder in mice compared to humans. Although it varies with each mouse line, *Mecp2* heterozygous females tend to appear normal through early maturity (up to 6 months) and may remain reproductively viable until very late stages (>18 months) but do gradually show an RTT-like phenotype (Chen *et al.*, 2001; Guy *et al.*, 2001). On the basis on symptom severity, hemizygous *Mecp2* mutant males have been considered a better experimental model for the many phenotypic features of the disorder, although heterozygous female mice are increasingly used because they model the mosaic expression of *Mecp2* that occurs in human RTT patients.

A critical finding in *Mecp2*-null animals showed that restoration of wild-type MeCP2 expression could rescue the RTT phenotype, even in highly symptomatic, mature mice, indicating that for some degree of normal CNS function, MeCP2 does not need to be expressed within a critical developmental window (Luikenhuis *et al.*, 2004; Guy *et al.*, 2007). This discovery energized a pragmatic emphasis within the field of RTT research by strongly suggesting the possibility of ameliorating, or perhaps eliminating, the disorder in humans. This emphasis aims to both investigate the basic neurobiology of MeCP2 and RTT and validate the animal models, establishing distinctive pathological alterations that can be used to quantify the effects of therapeutic interventions. The complexity and heterogeneity of MeCP2's role in RTT counsels an analysis at many levels: genomic, proteomic, morphological, physiological and behavioural.

Conclusion and General Aims

The aim of this thesis was to use a RTT mouse model to characterize a set of neurons previously shown to have reduced dendritic arborization in human RTT patients, the Layer 5 (L5) pyramidal output neurons of the motor cortex (Armstrong *et al.*, 1995; Armstrong *et al.*, 1998). A pragmatic goal of this work was to arrive at a quantitative

basis for evaluating therapeutic interventions involving *Mecp2* gene replacement, using a neuron-specific transgenic reporter mouse line. Motor cortex L5 pyramidal neurons were selected because of documented large reductions in brain volume associated with frontal regions, as well as the numerous motor deficits observed in RTT patients and in *Mecp2* mutant mice. We hypothesized that, as in human RTT patients, L5 pyramidal cells would exhibit significantly reduced dendritic arborization in both apical and basal compartments.

Our principal finding is that YFP-expressing L5 neurons show significant but selective reductions in morphological parameters in MeCP2 mutant mice relative to WT. Soma size is decreased and dendritic length is reduced in the basal arbor and in oblique dendrites in the apical tuft. We also find that the proportion of YFP-expressing neurons is altered in MeCP2 mutant mice, and assess the advantages and disadvantages of using this particular neuron-specific transgenic reporter mouse line, which is increasingly popular in the RTT research field.

Chapter 2: Altered Neuronal Phenotype in YFP-MeCP2 Mice

Introduction

The central hypothesis of this study was that cortical motor output neurons in MeCP2 mutant mice would exhibit altered neuronal morphology similar to that documented in human RTT patients (Belichenko *et al.*, 1994; Armstrong *et al.*, 1995; Bauman *et al.*, 1995b; Bauman *et al.*, 1995a; Belichenko and Dahlstrom, 1995; Belichenko *et al.*, 1997; Armstrong *et al.*, 1998). Several mouse lines have been developed to study RTT and MeCP2, and to date, three lines are commonly used, from the labs of Adrian Bird, Rudolph Jaenisch, and Huda Zoghbi (Chen *et al.*, 2001; Guy *et al.*, 2001; Shahbazian *et al.*, 2002a). All recapitulate the RTT phenotype with varying degrees of severity, reflecting the range of symptoms observed in human patients. Our studies used the Jaenisch mouse (*Mecp2*$^{tm1.1Jae}$/Mmcd), which expresses a mutant form of MeCP2 having a 116 amino acid N-terminal deletion comprising most of the MBD. This line was selected because both male and female mice exhibit moderate to severe symptoms, but females remain reproductively viable with reasonable litter sizes as a consequence of slow symptom progression. Although heterozygous female mice accurately model the mosaic expression of *Mecp2* in the CNS, male mice are considered phenotypically more similar to human RTT patients in terms of their earlier symptom onset and more rapid symptom progression. Furthermore, because males are hemizygous for *Mecp2*, they present a simplified experimental condition in which all cells express either the WT or mutant allele for a given mouse. We consequently elected to compare wild-type (WT) with *Mecp2* $^{-/y}$ males in these experiments.

To facilitate studies of neuronal structure, we crossed the Jaenisch *Mecp2* mutant mouse with a second transgenic line, B6.Cg-Tg(Thy1-YFPH)2Jrs/J (abbreviated "YH"), that expresses yellow fluorescent protein (YFP) in a restricted subset of Layer 5 pyramidal neurons in the neocortex (Feng *et al.*, 2000). The relatively sparse labelling of these cells permits the visualization of the dendritic architecture of individual neurons. The two original mouse lines were maintained on different mixed genetic backgrounds—

predominantly 129/Sv for the *Mecp2* mutants and C57BL/6 for the YH mice. The poor reproductive rate and early mortality that occurred in the inbred *Mecp2* mutant line led us to outcross incipient inbred males homozygous for *YFP* with 129/Sv females heterozygous for the *Mecp2* mutation. F1 generation mice were used in these experiments for several reasons: significantly improved litter sizes, an equivalent *YFP* transgene dosage in all offspring, and for litters from a given breeding pair, a common set of genes flanking both *Mecp2* and *YFP*. The latter point is significant because the chromosomal segment flanking the mutant or transgenic locus may contain thousands of genes from the embryonic stem cell donor strain, which may influence or alter the phenotypic effects of the target locus (discussed in Chapter 3) (Lipp and Wolfer, 2003). The principal caveat to the breeding program we pursued is that mouse genetic background can have pronounced effects on a mutant phenotype, either masking or enhancing changes in brain or behavior (Silva *et al.*, 1997; Wolfer *et al.*, 2002; Lipp and Wolfer, 2003). Therefore, prior to characterizing the effects on neuronal structure, we first examined our hybrid *YFP* $^{+/-}$ / *Mecp2* $^{-/y}$ (YHM) line for possible background effects relative to published data on the *Mecp2*$^{tm1.1Jae}$/Mmcd line. Variables considered in the hybrid were brain weight, body weight, neuron density, and symptom progression.

Previous studies comparing WT and MeCP2 mutant male mice from the *Mecp2*$^{tm1.1Jae}$/Mmcd line revealed significant reductions in the volume of motor cortex as well as reduced thickness in all cortical lamina excepting Layer 4 (Kishi and Macklis, 2004; Belichenko *et al.*, 2008). Laminar volume reduction was greatest in Layers 2/3, and pyramidal neurons from those layers showed reduced dendritic branching. Since the neurons in different cortical layers play distinct functional roles in cortical circuits, we exploited the neuronal labelling of the YFP-H line to expand the previous findings to include Layer 5 pyramidal neurons. Motor cortex was selected because of the prominent motor deficits observed in RTT patients and MeCP2 mutant mice.

The neurophysiological impact of abnormal dendritic morphology depends on the specific context of the local and projection circuits in which a given neuron participates. Cortical circuitry has many stereotypical features that have been recognized for over a

century in pioneering works by Ramon y Cajal and others, but the existence of a "canonical circuit" describing neuronal connectivity across cortical layers, as well as between different cortical regions and subcortical structures, remains a matter of active research and debate, as summarized by Bota *et al.* (2003):

> The brain's structural organization is so complex that 2,500 years of analysis leaves pervasive uncertainty about (i) the identity of its basic parts (regions with their neuronal cell types and pathways interconnecting them), (ii) nomenclature, (iii) systematic classification of the parts with respect to topographic relationships and functional systems and (iv) the reliability of the connectional data itself.

Bearing this daunting caveat in mind, a summary of current perspectives on the general organization of the neocortex will be presented to provide a context for the experimental findings in this study. This summary is based on several comprehensive reviews (Mountcastle, 1997; Mountcastle, 1998; Buxhoeveden and Casanova, 2002; Swanson, 2003; Douglas and Martin, 2004; Douglas and Martin, 2007).

Laminar and Columnar Organization of the Neocortex

The cerebral cortex has a six-layer laminar structure that forms during mid- to late embryogenesis. These layers emerge sequentially over cortical development and at maturity exhibit distinctive histological staining patterns, termed cytoarchitectonics, that reflect laminar and regional differences in the shapes, sizes, and densities of neuronal somata. Cortical layers are composed of several basic types of excitatory and inhibitory neuron, each having characteristic somatodendritic morphologies and axonal projection targets. In general, excitatory/glutamatergic neurons are pyramidal, having "tree-like" dendritic arbors and long axonal projections, while inhibitory/GABAergic neurons are stellate, and make local synaptic connections with neighbouring neurons. For clarity, only the organization of excitatory neurons will be described here.

Layer 1 (L1), or the molecular layer, is the most superficial layer of the cortex. L1 is sparsely populated with somata and contains horizontally extending axons from cortex and thalamus, axonal termini, and apical dendrites from neurons in deeper lamina. The

apical dendrites from pyramidal neurons in Layers 2-5 form fascicular bundles that terminate in L1. As a general rule, the basal dendrites of these same neurons tend to ramify within the same layer as their somata or the layer directly below. Layers 2/3 contain small pyramidal neurons with axons that project both vertically (across lamina) as well as laterally. Layer 2 (L2) pyramidals are small and tend to form associational (intrahemispheric) lateral projections, while Layer 3 (L3) neurons are larger and generate both associational and commissural projections to the contralateral hemisphere, mainly to L5. Commissural corticocortical projections primarily target L1-3. Layer 4 (L4) is the primary relay for inputs from the thalamus and other subcortical structures to other cortical neurons. Excitatory spiny stellate L4 neurons form predominantly local-circuit projections, mainly to L3.[2] Layers 5 and 6 (L5, L6) contains the largest pyramidal neurons. L5 apical dendrites extend into L1-3 and basal dendrites ramify primarily within L5. L5 axons mainly project to L6 and to subcortical structures including striatum, thalamus, brainstem, and spinal cord nuclei. L6 neurons, which include both pyramidal and multiform morphologies, receive inputs from all cortical layers and project primarily to the thalamus. The thickness of each cortical layer varies by brain region, and has been shown to vary substantially between mice of different genetic backgrounds (Lev and White, 1997; Kishi and Macklis, 2004; Altamura *et al.*, 2007).[3]

The dominant interactions between these neurons follow a stereotypical vertical/ translaminar sequence of excitation that may be roughly conceptualized as using L4 for thalamic input, L2/3 for higher-order cortical computations, and L5-6 for cortical output (Swanson, 2003). The sequence of thalamic input to L4 that eventually proceeds to L5-6 output back to thalamic nuclei forms a feedback loop that is considered one of the fundamental circuits involved in cortical function. There is substantial evidence that this translaminar vertical pathway is organized into narrow, repeating columnar groups of neurons that compose modular computational units, termed minicolumns (Mountcastle

[2]Some cortical areas lack a distinct Layer 4, and are called agranular or dysgranular due to the characteristic Nissl staining pattern resulting from a low density of stellate L4 neurons. M1 motor cortex has a thin L4 and is considered agranular (Shipp, 2005).

[3]The average laminar thickness in M1 motor cortex in mice of mixed genetic background similar to that used in these studies (129-CD1-C57BL/6J) is presented in Fig 1. (Altamura *et al.*, 2007).

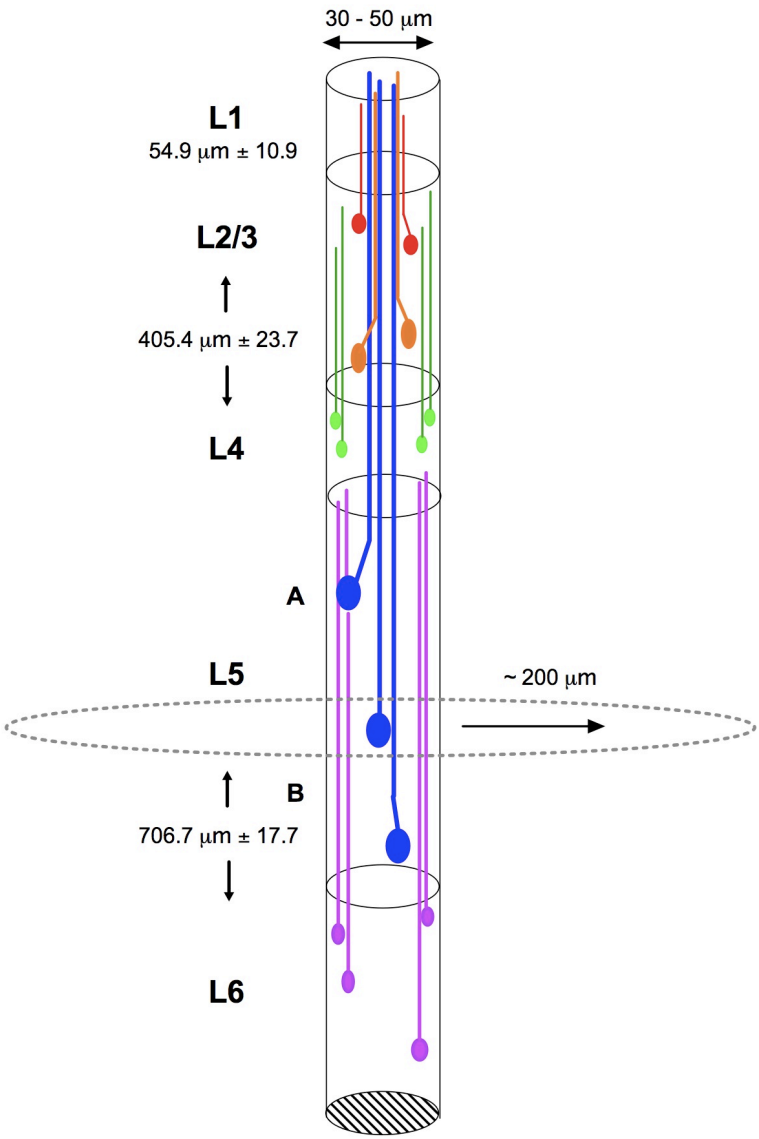

Figure 2. Minicolumn structure in mouse motor cortex.

Minicolumns are organized around bundles of apical dendrites (AD) with patterned projections from each cortical layer. For clarity, inhibitory interneurons and lateral dendrites (basal and apical tuft) are omitted. The central axis of the minicolumn is composed of AD from L5, which fasciculate and extend to L1. L2-3 AD add to the central bundle and also extend to L1. L6 AD project at the column periphery, and terminate at the lower boundary of L4. L4 AD terminate at the lower boundary of L1 and also remain peripheral. An estimated lateral extent of L5 basal dendrites in motor cortex is shown as a dotted ring.[4]

[4]Adapted from Lev and White (1997) with additional data from Favorov and Kelly (1994), Tsiola *et al.* (2003), Altamura *et al.* (2007), Hattox and Nelson (2007).

1997; Buxhoeveden 2002; Douglas 2004). The structure of a typical minicolumn is shown in Fig. 2 (adapted from Lev & White, 1997).

Each minicolumn is composed ~ 80 – 100 cells, which are organized into a central vertical array of excitatory neurons surrounded by a circumferential zone of inhibitory interneurons (Mountcastle, 1997). Cells in minicolumns respond with small latency differences to specific inputs. In sensory cortex, where minicolumns have been widely studied, the group firing patterns of neurons in minicolumns correlate with sensory receptive fields. Minicolumns mediate local processing of input strength, sharpening of output contrast by lateral inhibition, and recruitment or inhibition of other brain regions relevant to a particular behavior or task (Jones, 2000). Minicolumns may also be arranged into larger functional macrocolumns, as occurs in the well-studied barrel fields of the rodent somatosensory cortex; one macrocolumn may contain 40-80 minicolumns (Favorov and Kelly, 1994; Fox, 2008). While minicolumns are well-characterized in certain cortical regions, both structurally and electrophysiologically, their comprehensive definition remains a matter of debate, due to high variability in their size, cellular components, synaptic connectivity and function (Buxhoeveden and Casanova, 2002; Rakic, 2008). Anatomical and physiological studies indicate a size range of 20 - 60 μm in many mammalian species, with measurements in mice ranging from 30 – 50 μm (Lev and White, 1997; Favorov and Kelly, 1994; Buxhoeveden and Casanova, 2002). Each minicolumn is also surrounded by a soma-poor region, the peripheral neuropil space, that contains dendrites, unmyelinated axons, and synapses (Buxhoeveden and Casanova, 2002). A recent estimate put the mean value of intercolumnar distance at 80 μm (Buldyrev *et al.*, 2000). At present, there are comparatively few studies examining the structure of minicolumns in motor cortex, although characteristic axonal bundling occurs in mice (Lev and White, 1997), and an ordered mapping of directionally tuned minicolumns has been demonstrated in monkeys (Georgopoulos *et al.*, 2007). These issues notwithstanding, columnar organization is a defining characteristic of the cortex, and relevant to the consequences of *Mecp2* mutation on neuronal architecture.

Results

Characteristics of YHM Mouse Line

To assess for genetic background effects in the YHM hybrid mouse line, the weights of fixed brain tissue from WT and MeCP2 mutant males were obtained over a large range of ages (Fig. 3). The mean weight of fixed brain tissue in mature (≥ 4 week old) MeCP2 mutant male mice is significantly reduced (14.7%) compared to WT (0.396 g ± 0.004 vs. 0.464 g ± 0.003, respectively; $t_{103} = 12.64$, $P < 0.0001$, $n_{WT} = 55$, $n_{Mut} = 48$) (Fig. 3B).[5] A linear regression was performed to probe for any age-dependent trends in brain weight using animals between 1.5 and 23 weeks of age ($n_{WT} = 66$, $n_{Mut} = 61$) (Fig. 3A). Neither slope differed significantly from zero, indicating no progressive changes in brain weight for either genotype. These trends are roughly comparable with previous findings in both the *Mecp2*$^{tm1.1Jae}$/Mmcd line and in human RTT patients (Chen *et al.*, 2001; Armstrong, 2005). The mean brain weights of mature mice for both genotypes appear larger, have a wider range of values, and show a higher degree of overlap between genotypes in the YFM line compared to that seen in *Mecp2*$^{tm1.1Jae}$/Mmcd mice.[6] The apparent increase in mean brain weight in both genotypes suggests the possibility of heterosis or hybrid vigor arising from the mixed genetic background of the YHM mice (Lipp and Wolfer, 2003), but because the relative difference between genotypes is preserved, it is likely that, on average, both mutant and WT mice are equally affected. The increased range of values and greater overlap in distributions suggests a larger degree of variability within each genotype, however, that may reflect differential effects from the mixed genetic background. We also assessed the correlation between body and brain weights in mature WT vs mutant mice (~8 - 18 weeks old) (Fig. 4, Table 1). WT body and brain weight values were more tightly clustered than those seen in mutants. Mutant mice were more inclined to exhibit either weight gain or loss with increasing symptom severity, indicating that the reduction in brain weight is not strictly a consequence of smaller overall body size resulting from systemic developmental arrest.

[5] All measurements presented as mean ± SEM unless otherwise indicated.

[6] Mean brain weight values were not provided, but the range of mature brain weights was ~ 375 – 425 mg for WT and ~ 325 – 400 mg for mutant mice (Chen *et al.*, 2001).

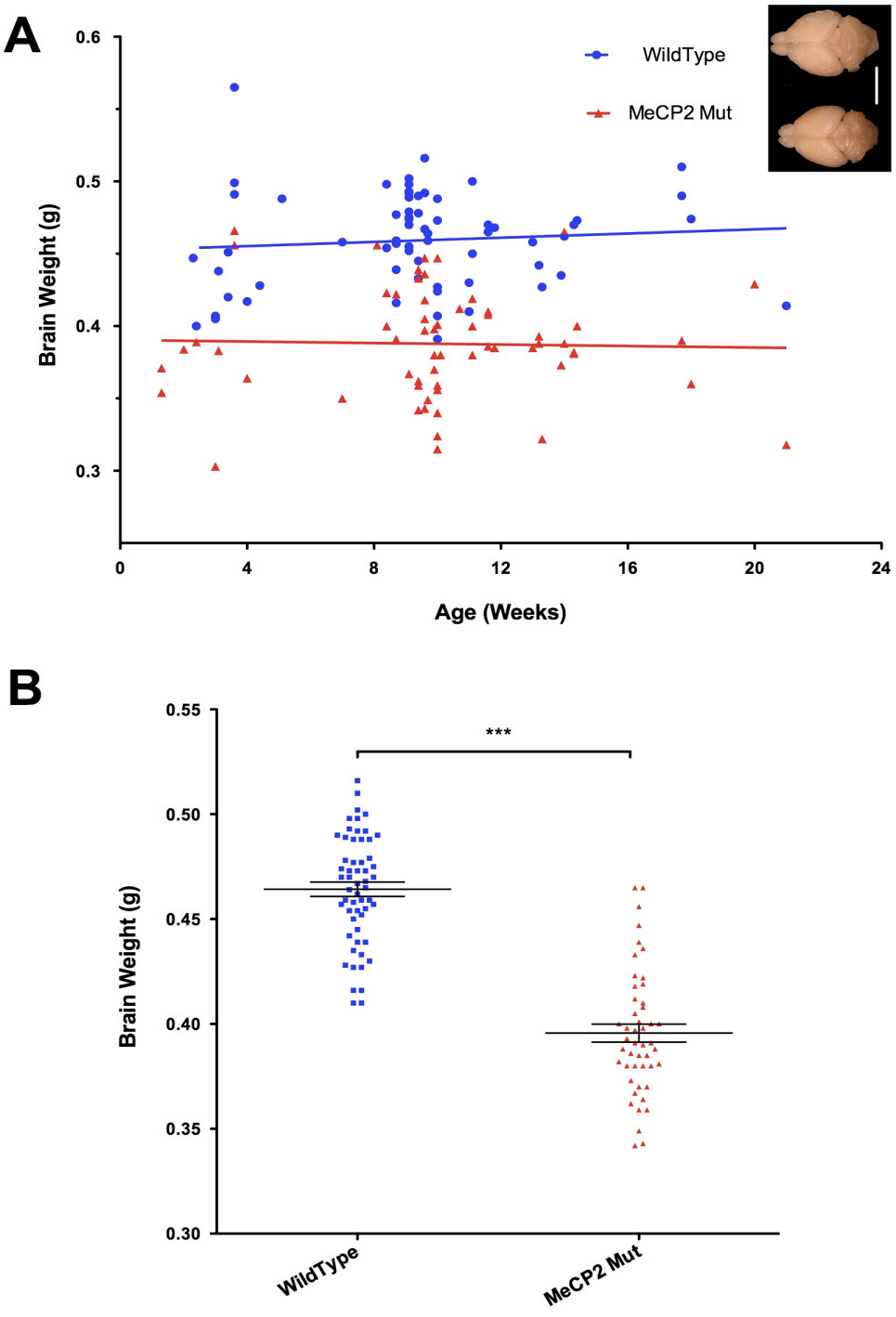

Figure 3. Brain weight is reduced in MeCP2 mutant mice.

A) Brain weight as a function of age in WT and MeCP2 mutant mice. Horizontal lines indicate a linear regression and suggest no age-dependent effect. Inset: Mouse brain size is visibly reduced in a mature (9 week) MeCP2 mutant male mouse (lower) relative to the WT littermate. Scale bar = 5 mm. B) Mean brain weight in mature MeCP2 mutant mice is significantly lower than in WT.

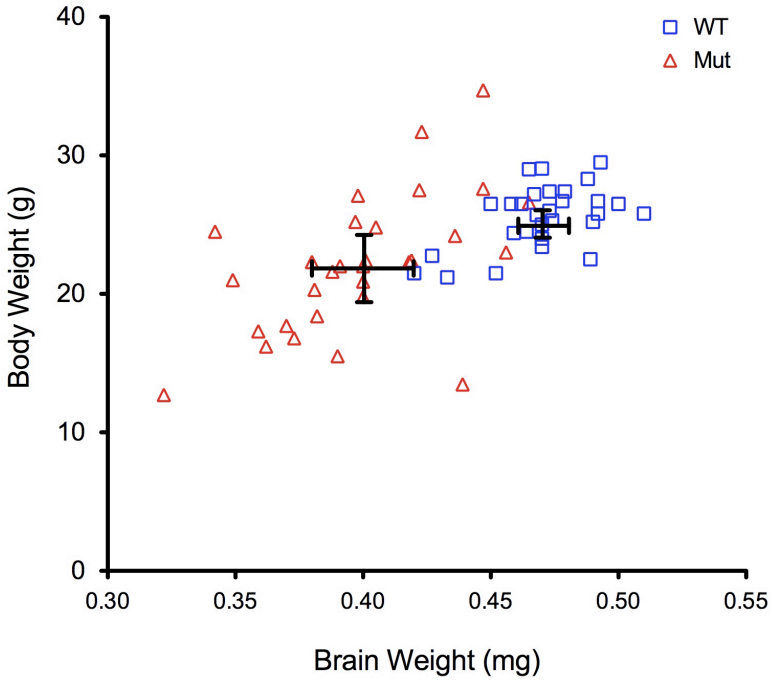

Figure 4. Body weight vs. brain weight in MeCP2 mutant mice.
Bars indicate mean ± SD.

	WT	Mut
Brain Weight (mg)	0.47 ± 0.004	0.399 ± 0.007
Body Weight (g)	25.6 ± 0.433	22.1 ± 0.942

Table 1. Body weight vs brain weight in YHM Mice.
Values are mean ± SEM (n_{WT} = 28, n_{Mut} = 29).

We next assessed the rate of symptom progression in MeCP2 mutant YHM mice by weekly monitoring until sacrifice or death (Fig. 5, n = 29). Three broad tiers of symptom level (mild, moderate or severe) were defined as follows: mild symptoms included slight curling or clasping of hindpaws without crossing legs, slower movements, and slightly delayed reactions to handling. Moderate symptoms included weight gain, partial hindlimb clasping, periods of hypoactivity with recovery after handling, and shivering. Severe symptoms included extreme lethargy, kyphosis, periodic hyperventilation, substantial

weight gain or loss, severe hindlimb clasping with full crossing of back legs, and little or no recovery of activity after handling. Symptom progression was highly variable and sometimes extremely rapid (with a few weeks between symptom onset to severe symptoms or death). The mean onset of mild symptoms was 8.67 weeks ± 1.32; of moderate symptoms, 10.3 weeks ± 2.65; and of severe symptoms, 10.7 weeks ± 3.43 (SD). The low number of instances of severe symptoms is likely a result of animals having been sacrificed prior to having reached the most advanced stage (most experimental animals were used at 9-11 weeks of age).

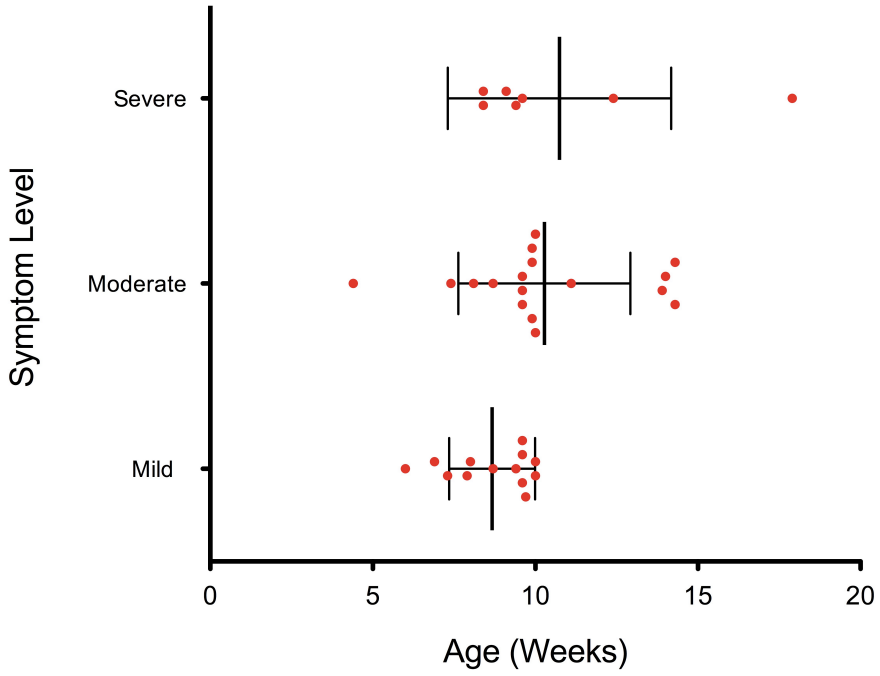

Figure 5. Symptom progression in MeCP2 mutant mice.
Data points indicate the first instance of each level of severity. Bars indicate mean ± SD.

The original symptom progression described for *Mecp2*$^{tm1.1Jae}$/Mmcd mice notes that most mutants developed symptoms by 5 weeks, showed physical deterioration by 8 weeks, and died at 10 weeks (Chen *et al.*, 2001). Similar to the increased mean brain weight, the delayed symptom progression we observe also suggests that some heterosis is occurring in the YHM line. Symptom severity showed a general progression but some mice would oscillate between intermittent periods of higher and lower severity. (For visual clarity, only the first recorded instance of a given symptom level is plotted for each

mouse in Fig. 5). The rate of progression was also highly variable; some mice would progress from mild to severe symptoms within a few weeks, while others maintained stable mild symptoms until sacrifice. There was no relationship between symptom severity and brain weight (data not shown). These results reveal a high degree of phenotypic variability in features of the RTT phenotype in mice having an identical *Mecp2* mutation.

Neuronal density was compared in symptomatic MeCP2 mutant males relative to their WT littermates in the YHM line. Coronal sections containing frontal, motor, or retrosplenial cortex (see Fig. 15) were stained with a neuron-specific stain (Neurotrace 530/615) and boundaries of L5 were established with reference to the somata of YFP-expressing pyramidal cells. One-way ANOVA revealed significant density differences between brain regions and genotypes ($F_{5,12} = 3.689$, $P < 0.0001$). Post-hoc Bonferonni multiple comparison tests showed that neuronal density in L5 is significantly higher in MeCP2 mutant mice in all three areas: 46% in frontal cortex, 32% in motor cortex and 24% in retrosplenial cortex (Fig. 6; Table 2). Within each genotype, a similar rostrocaudal increase in neuronal density across cortical regions was observed, with a higher cell density in retrosplenial cortex relative to frontal association and motor cortex ($t_5 > 4.670$, $P < 0.01$ for all pairs tested). The mean cell densities were not significantly different between frontal and motor cortex within both genotypes. These data extend previously published data in human and mouse brains (Bauman *et al.*, 1995a; Chen *et al.*, 2001) and are consistent with frontal regions being the most severely affected (Carter *et al.*, 2008).

	Mean Neuronal Density ± SD (neurons / 100 μm^3)	
Cortical Region	**WT**	**Mut**
Frontal Association	17.39 ± 0.35	25.42 ± 1.04
Motor	19.84 ± 0.58	26.28 ± 0.15
Retrosplenial	25.14 ± 1.29	31.22 ± 0.69

Table 2. Increased neuronal density in MeCP2 mutant mice.

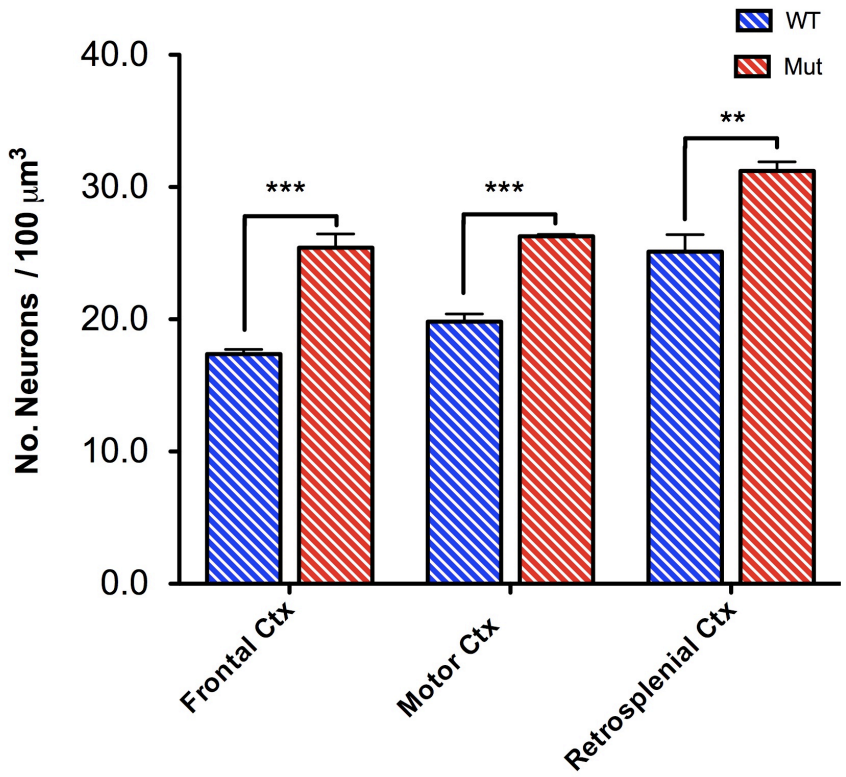

Figure 6. Increased neuron density in MeCP2 mutant mice

Layer 5 neuronal density is significantly increased in MeCP2 mutant males mice relative to WT littermates in three cortical regions. Significant differences between regions within genotype not shown for visual clarity.

Morphological Analysis of YFP-Expressing Layer 5 Pyramidal Neurons: Soma Size

We examined the effect of MeCP2 mutation on the size of neuronal cell bodies in L5. Soma traces were performed on the same mice used in neuron morphology experiments with an additional mouse used in the mutant condition (Fig. 7A). Mean soma size was significantly smaller (24.1%) in MeCP2 mutant mice (WT: 181.1 μm^2 ± 11.08, Mut: 137.4 μm^2 ± 9.028; $n_{WT} = 6$, $n_{Mut} = 5$; $t_9 = 3.097$, $P = 0.0128$). This is consistent with the reduced brain weight and increased neuronal density observed in the mutants.

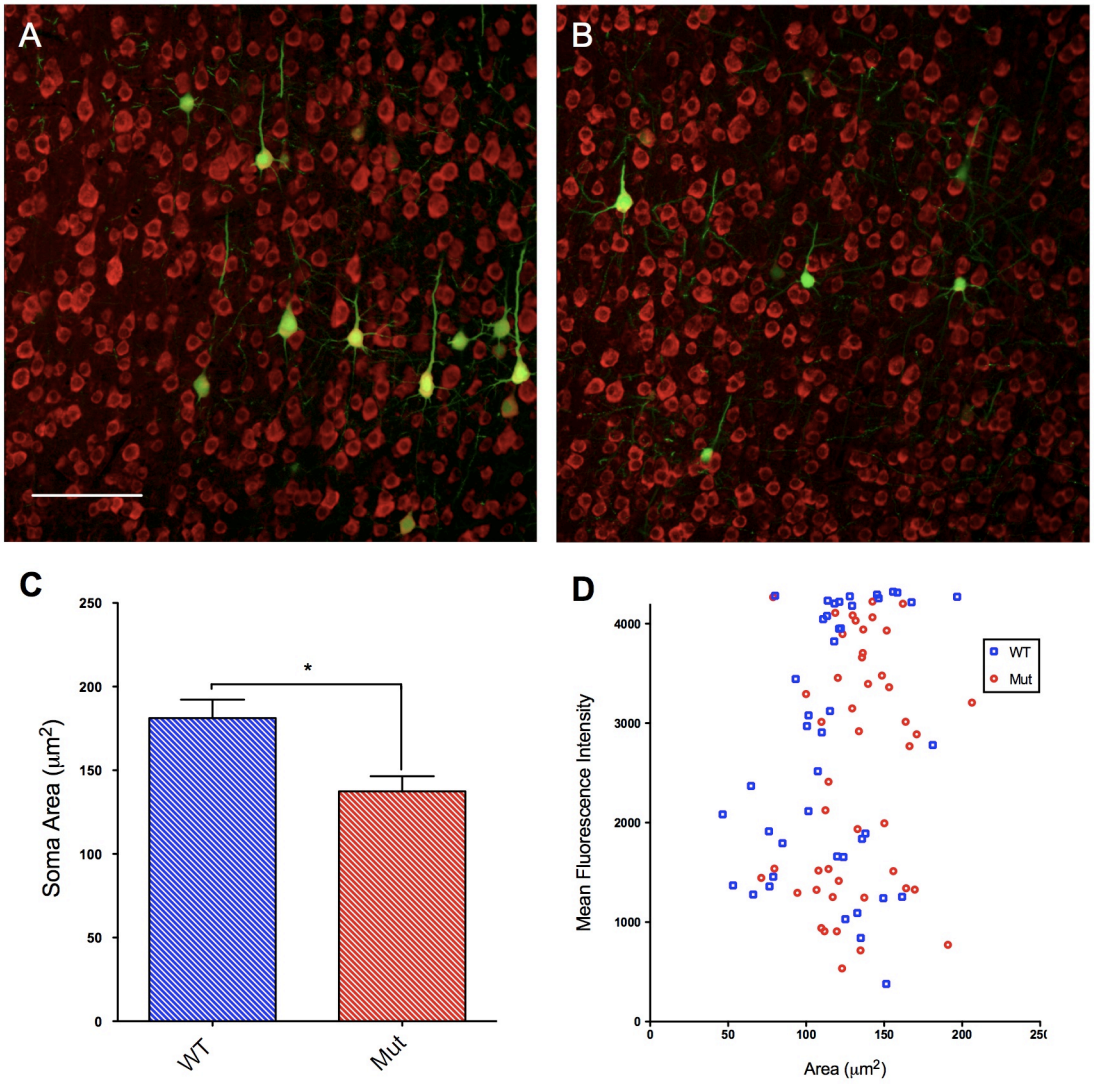

Figure 7. Reduced soma size in L5 pyramidal neurons in MeCP2 mutant mice

YFP-positive L5 pyramidal cells in motor cortex Scale bar = 100 μm. C) Mean somatic area of YFP-expressing Layer 5 pyramidal neurons is reduced in MeCP2 mutant mice relative to WT. D) Plot of YFP fluorescence intensity as a function of somatic area. Fluorescence intensity is measured on a 12-bit grayscale.

The intensity of YFP fluorescence in these neurons was highly variable, which suggested the potential for observer bias in the tracing of soma perimeters: faint cells could be judged as smaller due to diminished contrast of the soma boundary with the background. We tested for this using a post-hoc control by plotting soma area against the mean grayscale intensity value for each soma (Fig. 7B; $n_{WT} = n_{Mut} = 1$, WT: 46 replicates; Mut:

43 replicates). Imaging conditions were established which provided the greatest range of subsaturating fluorescence intensities for somata. No significant correlation was detected between soma area and fluorescence intensity for either genotype (mutant $R^2 = 0.02286$, WT $R^2 = 0.06471$). This indicates that fluorescence intensity was not likely to introduce significant bias in estimates of somatic perimeters.

Analysis of Dendrite Morphology

We next examined the dendrite morphology of YFP-expressing L5A pyramidal neurons in the motor cortex of WT and MeCP2 mice. Image stacks were obtained for both apical and basal compartments. The basal compartment was defined to include the first 100 μm of the primary apical dendrite and its secondary branches. Preliminary investigations revealed substantial variability in neuronal size and degree of dendritic branching within each animal, so we elected to perform a large number of replicates to ensure adequate representation of intrasubject variation (n = 52 traces per compartment). Three-dimensional reconstructions were made of the complete dendritic arbor for all neurons passing exclusion criteria. Individual reconstructions were subjected to a 3D Sholl analysis of dendrite crossings (Fig. 8A, 8B) (Sholl, 1953), which quantifies dendritic branching as a function of distance from the origin. In the basal compartment, 3D Sholl analysis centers on the cell body and applies a set of concentric spherical shells at regular intervals (10 μm), and then counts the number of dendritic intersections through each sphere (cartoon inset in Fig. 8C). We adapted the Sholl analysis to the apical compartment by defining the Sholl origin as a point on the apical dendrite 300 μm from the pial surface, with 20 μm radial intervals. In both mutant and WT motor cortex, this is situated within L3, and corresponds to a distance of ~100 – 200 μm from L5A somata for WT mice, and slightly less in the mutant. The Sholl cross analysis is ideally suited to stellate patterns of radially distributed dendrites, as typically occurs in pyramidal neuron basal arbors, but it may not capture the full extent of dendritic ramification in non-stellate, tangentially projecting arbors, as occurs in the apical tuft or in secondary apical dendrites close to the soma. We consequently performed a modified Sholl analysis to include the summed dendritic length per radius (Fig. 8C, 8D). Traces were analyzed using a repeated measures ANOVA with genotype and distance from origin as predictor

variables and Sholl crossing or length as the response variable. Differences at specific radii were analysed using Bonferroni post-test *t*-tests.

Following the Sholl analysis we also examined the cumulative total dendritic length as function of the Sholl radius (Fig. 9A, 9B), percentage dendritic length by branch order, (Fig. 9C, 9D), and the maximum Sholl radius for both compartments. Branch order gives a measure of the "bushiness" of the dendritic arbor by quantifying the percentage of total dendritic length at each level of branching. First order dendrite segments are those emerging from the soma (including the apical dendrite), while higher orders are comprised of segments that follow each branch bifurcation (inset, Fig. 9D). More "bushy" neurons thus have the majority of dendritic length in branch orders > 1.

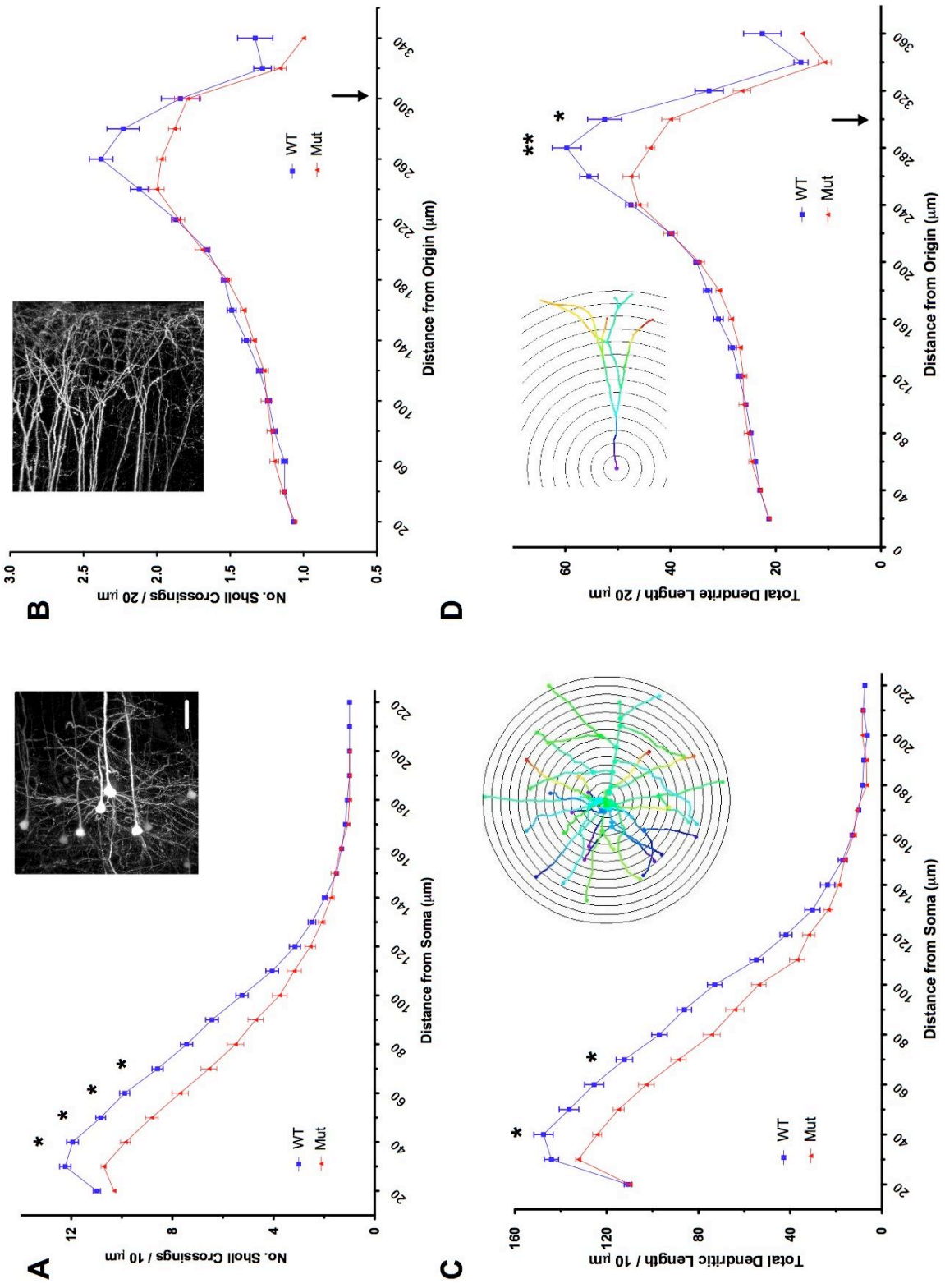
A
No. Sholl Crossings / 10 μm
Distance from Soma (μm)
WT
Mut
B
No. Sholl Crossings / 20 μm
Distance from Origin (μm)
WT
Mut
C
Total Dendritic Length / 10 μm
Distance from Soma (μm)
WT
Mut
D
Total Dendrite Length / 20 μm
Distance from Origin (μm)
WT
Mut

Figure 8. 3D Sholl analysis of L5 pyramidal neurons in motor cortex.

Sholl analysis showing the number of dendrite crossings or summed dendritic length as a function of radial distance in the apical (B, D) and basal (A, C) compartments. Sholl crossings (A, B) indicate the number of dendrites intersecting each Sholl radius. Sholl lengths (C, D) indicate the summed lengths of all dendritic segments within a given radial band. Inset images in A, B show maximum intensity projections of representative confocal stacks of YFP-expressing neurons in the basal and apical compartment. Scale bar = 30 μm. Inset cartoons in C, D show similar examples of Sholl analysis traces in each compartment. Depth in the z-axis is colour-coded. Arrows in B, D show the point corresponding to the pial surface of motor cortex.

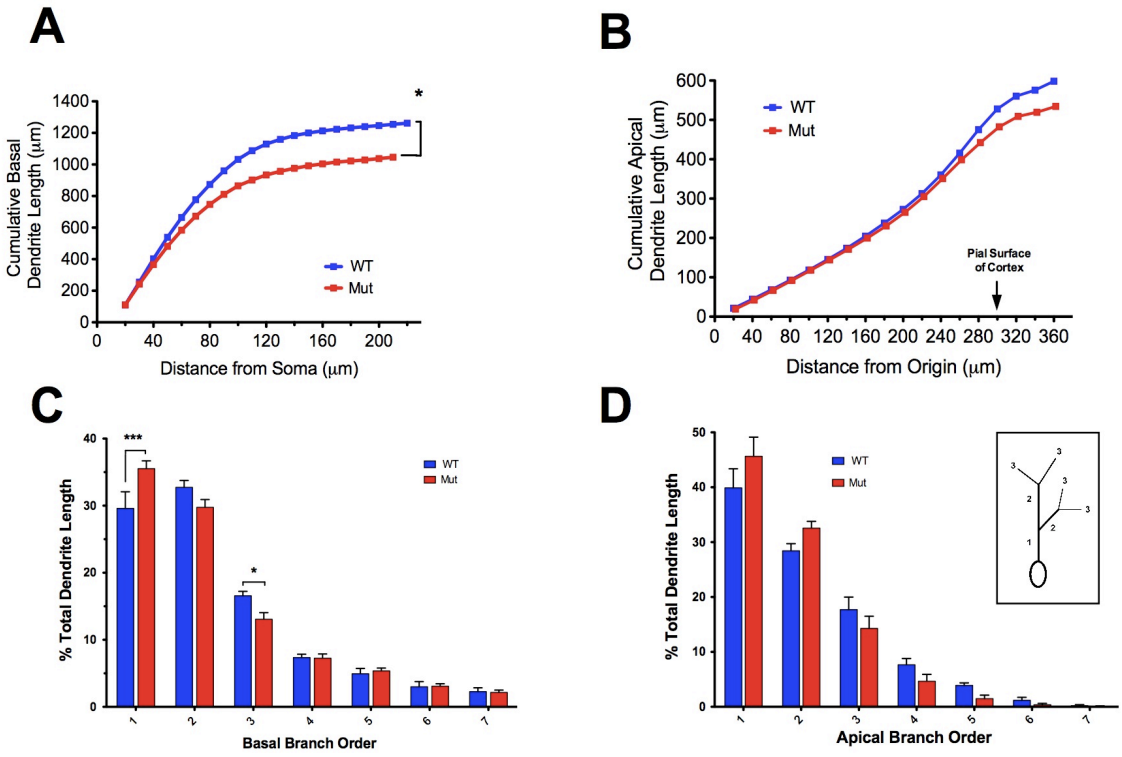

Figure 9. Total dendrite length and branch order

A) Cumulative total dendritic length as a function of distance from the soma in the basal compartment. B) Cumulative total apical dendritic length as a function of distance from a defined origin on the apical dendrite, 300 μm from the pial surface of motor cortex. C) Percent total dendritic length per branch order in the basal compartment. Higher branch orders represent dendrite segments that follow successive bifurcations of the primary dendrite. D) Percent total dendritic length in the apical compartment. Inset: diagram illustrating branch order hierarchy.

Basal Compartment

Dendritic traces were analyzed by comparing the summed lengths of all basal dendrites, including the first 100 μm of the apical dendrite and its secondary branches. The mean total basal dendritic length in WT neurons was 1192 μm ± 61.54. Total length in mutant neurons was significantly reduced by 18.6%, giving a mean total length of 969.8 μm ± 65.54 (t_8 = 2.472, P = 0.0386). We consequently examined the morphological changes underlying this difference.

The total dendritic length is determined by the degree of dendritic branching, but also by the maximum length of individual dendrites. The average maximum Sholl radius was significantly shorter (9.1%) in mutant neurons (128.1μm ± 3.463) compared to WT (140.9 μm ± 3.782, t_8 = 2.490, P = 0.0375). Mutant neurons also showed significant reductions in dendritic branching as a function of distance from the soma. The basal Sholl crossing analysis (Fig. 8A) revealed an interaction between distance and genotype ($F_{14,112}$ = 3.908, P < 0.0001). WT neurons had significantly more dendritic crossings over distances of 40-70 μm from the soma (t_8 > 2.999, P < 0.05). The trend for both genotypes shows a similar number of primary dendrites, followed by divergence with a peak number of crossings at 30 μm (WT = 12.24 μm ± 0.22; mutant = 10.72 μm ± 0.10) and a similar rate of decay until ~ 80 μm with convergence at ~ 150 μm. An interaction between distance and genotype was also found in the Sholl length analysis ($F_{15,120}$ = 3.508, P < 0.0001), with the summed dendritic length per Sholl radius significantly higher in WT neurons at 40 and 70 μm from the soma (t_8 > 3.021, P < 0.05). Sholl lengths follow a similar pattern to crossings with the exception that the peak mean WT value (147.59 μm ± 4.20) occurs at 40 μm from the soma, while the mutant peak value (132.3 μm ± 1.14) occurs at 30 μm. Relative to the number of primary basal dendrites, WT neurons have an increased number of branches up to ~ 50 μm from the soma, while mutant neurons have both fewer branches and a shorter peak branching radius (~30 – 40 μm from the soma). WT neurons therefore maintain a larger number of dendritic branches over a larger volume in proximal portions of the basal arbor.

This is reflected in the cumulative basal dendritic length and the percentage total dendritic length per branch order (Fig. 9A, 9C). Branch order analyzed by two-way repeat measures ANOVA showed a significant interaction between branch order and genotype ($F_{6,28} = 6.849$, $P = 0.0001$). Bonferroni post-tests showed a significantly greater percent dendritic length (5.93%) within the first branch order for mutant neurons ($t_6 = 5.053$, $P < 0.01$), and significantly less at the third branch order (3.5%) ($t_6 = 2.987$, $P < 0.05$). WT neurons show a trend towards a greater proportion of total dendritic length in the second and third branch orders. The cumulative plot of basal dendritic length (Fig. 9A) also reflects the differences in early branch orders, with mutant and WT curves beginning to diverge at approximately 30 μm from the soma. Cumulative dendritic length increases at a higher rate in WT neurons up to ~ 130 μm from the soma, after which point the neurons from both genotypes increase slowly at a similar rate. The percentage of total dendritic length in branch orders > 3 shows no trend favouring either genotype. This may reflect the small numbers (< 10%) of very large, highly branched neurons that were observed within both WT and mutant animals.

These data indicate that the total basal dendritic length of L5A pyramidal neurons is reduced in MeCP2 mice, and that this is a consequence of both shorter dendrites as well as a reduced number of higher order branches. One important caveat to these findings relates to our imaging method. Neurons in the basal compartment were selected for tracing when the somata were located within a defined central volume of the confocal stack. We imaged 200 μm thick slices of brain tissue. Ignoring shrinkage effects from tissue processing and mounting, a neuron at the exact center of the confocal stack would have ~ 150 μm to extend laterally in the x-axis in both directions and ~ 80 μm in the z-axis. We observe that the difference in the number of Sholl crossings in outer radii (Fig. 8A) begins to converge at ~ 80 μm, and converges at ~ 150 μm. Individual dendrite traces were sometimes observed to extend to the image boundary as well. Previous studies of smaller L2/3 pyramidal neurons in MeCP2 mutant mice has shown a similar convergence at a shorter distance (beginning at ~ 100 μm from the soma), but pyramidal cell basal dendrite arbors in other brain regions have lateral extents of ≥ 200 μm, and motor cortex is known to contain some of the largest pyramidal neurons in the brain

(Kishi and Macklis, 2004; Ballesteros-Yanez *et al.*, 2006; Benavides-Piccione *et al.*, 2006; Hattox and Nelson, 2007)**.** Consequently, we cannot rule out truncation artifacts. Given the differences we observe at short distances from the soma, however, the findings presented here suggest that if this method introduces a bias into the dataset, it will favour the null hypothesis by collapsing differences between neurons in WT and mutant mice.

Apical Compartment

Relative to the basal compartment, neurons in mutant mice showed much more subtle changes in the distal parts of the apical dendrite. The mean total dendritic length was not significantly different for the apical arbor between genotypes (WT: 526.1 μm ± 28.86; Mut: 472.9 μm ± 22.07; t_8 = 2.472, P = 0.1809). Further Sholl analysis (Fig. 8B, 8D) revealed a tightly overlapping trend in both genotypes indicating increasing bifurcation of the apical dendrite up to 60 μm from the pial surface, a region corresponding to the boundary between L1 and L2. At this point the apical tuft fans out in the WT neurons, with branching increasing into the molecular layer. In mutant neurons, the apical branching peaks (at ~ 2 branches) 60 μm from the pia, then drops off as it approaches the molecular layer. The Sholl cross analysis did not detect any significant interaction between distance and genotype, however ($F_{15,120}$ = 1.195, P = 0.285). Nevertheless, as the cartoon in Fig. 8D illustrates, a substantial degree of dendritic branch length can be subsumed within the outer Sholl radii, as a consequence of lateral dendritic spread of the apical tuft in L1. Consistent with this, a significant interaction was detected for Sholl lengths ($F_{16,128}$ = 2.143, P = 0.01), with WT neurons showing significantly greater dendritic lengths at Sholl radii of 280 and 300 μm (t_8 > 3.174, P < 0.05).

As expected the cumulative average dendritic lengths only diverge close to the pial surface, to a final difference of 10.3% (Fig. 9B). There was significant interaction between branch order and genotype ($F_{6,28}$ = 2.547, P = 0.0428), but no significant differences were detected at any specific branch order. These findings indicate a general trend toward higher-order branching in WT neurons, but also reflect a larger tangential spread. As with the basal compartment, an important caveat must be mentioned with regard to these findings. We imaged the apical and basal compartments of L5 neurons

separately in order to better resolve fine dendritic structures in thick tissue sections. Neurons from the upper blade of layer 5 (L5A) were selected to maximize the extent of dendritic arbor imaged across both compartments. It is possible that in some neurons imaged in the apical compartment, the primary apical dendrite bifurcated at distances closer to the soma than was captured in our image stacks, i.e. at distances > 300 μm from the pial surface. Depending on the proportion of neurons having early bifurcations in each genotype, this could significantly alter several measures in the apical compartment. The relative decrease in laminar thickness that occurs in MeCP2 mice suggests that if early bifurcation was occurring, it would be more commonly detected in mutant neurons. As with the potential truncation artifact in the basal arbor, the existence of this bias would likely tend to favour the null hypothesis.

Discussion

We examined the effects of MeCP2 mutation on neuronal structure in a hybrid YFP transgenic MeCP2 mutant mouse line. Brain weight, body weight, symptom progression and neuronal density measures were used to test for heterosis effects arising from the mixed genetic background in F1 generation hybrids. We find that the relative differences between mutant and WT animals are largely preserved, in accord with previously published findings, with MeCP2-deficient males having smaller brains and dysregulated body weights as well as increased neuronal density in several brain areas. The means and distributions of brain weights appeared higher in both genotypes, however, and the rate of symptom onset and progression was delayed and extended relative to the *Mecp2*$^{tm1.1Jae}$/Mmcd line. Consequently, it is possible that the introduction of new genetic material in these hybrid mice both increases phenotypic variability and mitigates phenotypic severity due to hybrid vigour. These issues notwithstanding, we demonstrate that *Mecp2* mutation still has significant effects on neuronal structure. L5A pyramidal neurons in the mutant condition had smaller, more densely packed somata. Dendritic architecture was more severely affected in the basal compartment, with less secondary and tertiary branching near the soma and shorter dendritic lengths. Changes in the apical tuft were more subtle, revealing a reduction in lateral branch length in the molecular layer. The potential functional significance of these alterations can be analyzed with reference to neuronal circuits as well as synaptic connectivity.

Alterations in dendritic morphology alone will alter the electrotonic properties of neurons, and may alter firing rate (Mainen and Sejnowski, 1996). Differences in pyramidal cell dendritic branching alters the coincidence detection of inputs from different cortical layers (Schaefer *et al.*, 2003). Similarly, dendritic morphology exerts substantial effects on the propagation of dendritic action potentials (APs), as well as the degree to which the APs can be affected by modulation of ion channel density. Critical factors include the number of dendritic branch points and the relative diameters of parent and daughter dendrites at the branch points (Vetter *et al.*, 2001). Backpropagating dendritic APs can alter both integration of synaptic inputs as well as synaptic plasticity (Stuart *et al.*, 1997b; Stuart *et al.*, 1997a). The interactions of these factors are complex and are not trivially modelled, but make the point that morphological changes can alter the functionality of MeCP2-deficient neurons prior to any considerations of synaptic connectivity.

The most significant consequence of reduced dendritic branching in mutant mice is likely to be how it affects the patterns of synaptic input. The majority of excitatory synapses on L5 pyramidal neurons occur in the basal dendrites and, to a lesser extent, the tangential dendrites of the apical tuft (Larkman, 1991). Although both apical tuft and basal dendrites have been shown to summate excitatory inputs by a similar mechanism using NMDA spikes (Larkum *et al.*, 2009), the pattern of inputs to each compartment is largely segregated and distinct. Both have been shown to operate as semi-independent compartments, a feature critical to the computational power of individual pyramidal cells (Spratling, 2002). Basal dendrites receive predominantly local recurrent inputs from neighbouring pyramidal neurons (Markram *et al.*, 1997), and thus integrate inputs from within functional columns as well as between neighbouring columns. Input to the L5 apical tuft, by contrast, arrives from higher cortical areas and thalamocortical pathways (Cauller *et al.*, 1998; Rubio-Garrido *et al.*, 2009). Selective alterations in each compartment may thus affect the function of local circuits as well as long-range feedback and control systems.

We found that lateral branches in the apical tuft were significantly shorter in MeCP2 mutant neurons, with a trend towards less higher-order branching. The molecular layer is commonly considered a field for intracortical projections, where other cortical regions exert long-range influences on the "top-down" control of information processing (Douglas and Martin, 2007; Kuhn *et al.*, 2008). Recently findings in rat neocortex show that L1 also receives massive and highly convergent excitatory input from thalamic nuclei (Rubio-Garrido *et al.*, 2009). These afferent "M-type" thalamic neurons are from a population distinct from those projecting to L4, and their high synaptic density in L1 is the result of large numbers of overlapping, minimally branched, tangentially widespread axons. These structural features are suggested to play a role in the modulation of cortical firing and the spread of coherent firing across large neuronal ensembles. Apical tufts display complex active properties in response to different forms of input. Synchronous summation of multiple inputs can generate calcium spikes which drive somatic firing via nonlinear interactions with backpropagating APs; weak asynchronous input can strongly increase the gain (input/output relationship) in L5 pyramidal cells by shifting firing patterns from isolated action potentials to bursts (Larkum *et al.*, 2004). Synaptic plasticity near the soma may also be signalled by subthreshold asynchronous inputs to the apical tuft (Dudman 2007). The reduced tangential lengths observed in the distal apical branches of mutant L5 neurons may therefore affect functional properties at both cellular and network levels. Diminished modulatory inputs and altered synaptic plasticity could reduce the functional repertoire of individual neurons. Fewer inputs from distal corticocortical and thalamocortical afferents could both weaken the functional binding of multiple cortical areas as well as recruitment of larger local sets of neurons into coherent groups, compromising the capacity to generate complex sequences of motor output.

Loss of MeCP2 had even more dramatic effects in L5 basal dendrites. Total dendritic length was significantly reduced by 18.6%, as a consequence of both shorter individual dendrites and reduced higher-order branching. Excitatory synapses on basal dendrites are predominantly recurrent inputs from all cortical layers within a neuron's respective minicolumn (Schubert *et al.*, 2001). It is currently unknown whether minicolumn structure is changed in the motor cortex of RTT patients, although reduced minicolumn

width was documented in temporal cortex in one limited study (Casanova *et al.*, 2003). Based on the reduced soma size and dendritic branching shown in our data and that of others, it is reasonable to hypothesize that minicolumn structure, and its relationship with L5 basal dendrites, could be diminished in mutant motor cortex.

Previous data have shown that in WT animals the peak complexity of pyramidal basal dendrite branching occurs between ~ 50 – 75 μm from the soma; dendritic spine density also varies with distance, peaking at Sholl radii of ~ 50 – 130 μm (Elston and Rosa, 2000; Ballesteros-Yanez *et al.*, 2006).[7] Minicolumn width in murine motor cortex is likely to fall in the range of ~ 30 – 50 μm (Lev and White, 1997; Favorov and Kelly, 1994; Buldyrev *et al.*, 2000).[8] Our findings suggest that the basal dendrites of mutant L5 pyramidal neurons exhibit significant branching reductions near the periphery of their respective columns. Reduced dendritic branching into the peripheral neuropil space and adjacent minicolumns is also likely. Depending on the exact relationship between minicolumn width and branch pattern, this could lessen the number of synaptic inputs either within minicolumns or between them, with many potential functional consequences. Reduced intracolumnar excitation could diminish the net output of individual columns, reducing the capacity for fine tuning of motor commands. Shorter dendritic extensions into neighbouring minicolumns could also limit the capacity for recruitment and binding of multiple minicolumns into larger functional macrocolumns, thereby weakening the concerted output necessary for initiating or controlling directed movements. It can be speculated that a diminished number of total synapses within the minicolumn relative to those outside of the column might also reduce intercolumnar contrast, leading to more synchronous activity in larger groups of neurons; this could in

[7]These data are from L5 pyramidals in macaque visual cortex and L3 pyramidals in murine motor cortex. Systematic differences in dendritic branching and spine densities occur between brain areas and species (BenavidesPiccione 2002; Elston 2005a; BenavidesPiccione 2006), so the values are intended to provide a general range of reference and may not quantitatively represent exact values in murine motor L5 pryamidal neurons.

[8]There are very few studies on minicolumn structure in motor cortex relative to somatosensory cortex, and quantitative measures can be heavily influenced by tissue processing—some common methods can result in volume shrinkages of over 80% (Robins 1956)—so these values are also a general estimate.

turn contribute to the conditions underlying the frequent epileptic seizures observed in RTT patients (Huppke *et al.*, 2007).

MeCP2 mutant neurons exhibited an altered distribution of basal dendritic lengths per branch order, with significantly less branch length in proximal Sholl radii. The proximal and distal segments of basal dendrites exhibit different responses to neuronal activity; high-frequency action potential bursts cause supralinear increases in calcium influx in distal segments only, which is believed to play a role in spike-timing-dependent synaptic plasticity (Kampa and Stuart, 2006). Reduced dendritic branching could change the manner in which back-propagating action potentials invade basal dendrites, altering the degree of NMDA receptor activation, and therefore long-term potentiation (LTP), in the distal branches. Reduced (LTP) has been demonstrated in L2-3 pyramidal neurons in MeCP2 mutant motor cortex and hippocampus (Asaka *et al.*, 2006; Moretti *et al.*, 2006). LTP induction mechanisms appear to be intact in the L5 pyramidals of symptomatic MeCP2 mutant mice, indicating that reduced excitatory connectivity precedes deficits in synaptic plasticity (Dani and Nelson, 2009). Nevertheless, MeCP2 mutation has demonstrated few consistent effects on glutamatergic synaptogenesis and synapse maintenance, with variable findings reported between human patients and from different mutant mouse lines. In the *Mecp2*$^{tm1.1Jae}$/Mmcd line used in our experiments, only spine morphology, and not spine density, was altered in L2/3 pyramidal neurons relative to WT, although spine density in another mouse line was significantly reduced (Kishi and Macklis, 2004; Belichenko *et al.*, 2009). Even on the assumption of equal spine density in L5A pyramidal neurons across genotypes, spine density is likely to peak over the Sholl radii where the branching of mutant neurons shows the greatest divergence from WT. This supports previous findings showing that the balance of spontaneous synaptic input favours inhibition over excitation in MeCP2 deficient L5 cells (Dani *et al.*, 2005).

Neuronal Subtypes in L5

It is relatively common practice in neurophysiological studies to pool measurements from multiple animals and use individual neurons as the statistical unit of replication. This is arguably appropriate when studying neurons from congenic animals that have been raised

in controlled conditions, as the inter-animal differences should be comparatively negligible. The breeding protocol used in our experiments, and those in many published studies using RTT mouse models, resulted in a multi-strain mixed genetic background, with an unknown degree of genetic heterogeneity between animals. Since there is accumulating evidence that an unknown number of modifier gene alleles can alter the severity of the RTT phenotype, we elected to take a conservative statistical approach that compared the values of a typical "average neuron" for each animal (discussed in Appendix I). While this circumvents issues of pseudoreplication and minimizes the likelihood of Type I errors (Hurlbert, 1984), it also masks a functionally significant heterogeneity.

Two major classes of L5 pyramidal neurons have been recognized for several decades: regular spiking (RS) and intrinsically burst spiking (IBS) (Connors *et al.*, 1982; Chagnac-Amitai *et al.*, 1990). Each class is distinguished by dendritic thickness, degree of branchiness, axonal projection patterns, and intracolumnar / transcolumnar synaptic connectivity; one example is the 10-fold higher ratio of excitatory to inhibitory inputs seen in IBS relative to RS neurons (Schubert *et al.*, 2001). More recently, the suite of L5 neuron subtypes has begun to expand dramatically. Rigorous quantitative methods using principal component analysis of large numbers of morphological variables have revealed 5 major morphological classes of L5 pyramidal cells in murine visual cortex; each group is characterized by specific clusters of structural features (Tsiola *et al.*, 2003). In a study of retrograde-labelled corticocortical-, corticotrigeminal-, and corticostriatal-projecting L5 neurons, the morphology, intrinsic membrane properties, firing properties, and afterpotentials were shown to be distinctive and highly stereotyped depending on the axonal projection target (Hattox and Nelson, 2007). Afferent excitatory projections *to* subtypes of cortical pyramidal neurons also appear to show a high degree of subcellular specificity in synaptic connectivity (Petreanu *et al.*, 2009). L5 neurons also appear to fall into different classes of transcriptional profiles. Distinctive gene expression profiles have been demonstrated for specific subpopulations of fluorescently labelled neurons from the mouse forebrain, including significant differences between L5 pyramidal cells from cingulate or somatosensory cortex (Sugino *et al.*, 2006). Over nine types of L5

pyramidal cells can now be distinguished on the basis of molecular markers (Molnár and Cheung, 2006). The coherent unification of a categorical system that incorporates developmental sequence, brain region, morphology, synaptic connectivity, circuit properties, electrophysiological behaviour, and transcriptional profile is in its infancy. Nevertheless, it appears likely that MeCP2 plays a central role in this diversity, consistent with its remarkable degree of complexity and diversity in function, expression, and regulation.

On this basis, it can be speculated that MeCP2 exerts highly differential effects in different subtypes of neuron; it is also possible that mutations in MeCP2 alter the proportions and relative distributions of different neuronal classes in the brain. Rett Syndrome has been called the Rosetta Stone for autism spectrum disorders (LaSalle *et al.*, 2005) because its monogenic nature facilitates the probing of extremely complex phenotypic effects. Investigations into both of the above-mentioned alternatives will not only help explain the pathophysiological effects of MeCP2 mutation but may also provide significant insights into the complex ordering of the central nervous system.

Perhaps most significantly for the data presented in the current study, it has recently been shown that the YFP-positive L5A neurons from the motor cortex of YFP-H mice represent a distinct population, with different excitatory inputs and electrophysiological properties as compared to adjacent unlabeled cells and YFP-positive neurons in L5B (Yu *et al.*, 2008). The significance of this finding is discussed in Chapter 3.

Chapter 3: Interaction of MeCP2 with *Thy-1-YFP*

Introduction

The YFP-H line (B6.Cg-Tg(Thy1-YFPH)2Jrs/J) was selected for our neuron morphology studies because of its selective and relatively sparse labeling of Layer 5 pyramidal cells throughout the neocortex (Feng *et al.*, 2000). YFP, a red-shifted GFP variant, is a useful cell marker for many reasons: it is bright and resistant to photobleaching, requires no chemical cofactors, has no obvious toxicity, and can diffuse into all cellular compartments (Shaner *et al.*, 2005; Tsien, 1998; Wachter *et al.*, 1998). The latter feature is of exceptional utility in neuromorphology studies because it allows the full extent of a neuron to be visualized, including dendritic spines, without requiring laborious dye injection (Chen *et al.*, 2000; Elston *et al.*, 1996). Furthermore, as a transgenic marker, it can be combined with tissue- or cell-specific promoters, permitting a high degree of selectivity for the study of multiple subpopulations of cells in the CNS (Nolte *et al.*, 2001; Sugino *et al.*, 2006).

A distinctive feature of transgenic reporters, both useful and potentially problematic, is the unpredictable behavior of the transgene after insertion into genomic DNA. Variegated gene expression has been demonstrated in several transgenic mouse lines, and appears to depend on the random conditions of copy number and chromosomal insertion site that obtain during the primary transgene integration event (Walters *et al.*, 1995; Dobie *et al.*, 1996; Dobie *et al.*, 1997; Graubert *et al.*, 1998; Opsahl *et al.*, 2002). Different expression patterns are observed across founder lines in spite of identical regulatory sequences in the transgene expression cassette. Some transgenic DNA sequences appear to be more sensitive to variegation effects than others (Festenstein *et al.*, 1996; Caroni, 1997). This sensitivity can be fruitfully exploited, as demonstrated with the neuron-specific *Thy-1* promoter: in addition to the YFP-H line, 25 other lines were generated, each expressing distinct patterns of GFP, YFP, or CFP in terms of brain regions, cortical layers, cell types, and density of labeling (Feng *et al.*, 2000).

Sparse labeling of individual neurons is required in neuromorphological studies because of the often complex and extensive dendritic arbors involved. The principal caveat in using a sparsely labeled mouse line like YFP-H is whether the set of neurons expressing the transgene are representative of the cell type under study. As discussed in Chapter 2, it is increasingly apparent that Layer 5 pyramidal neurons are not a unitary class, although the extent of this diversity is not yet fully understood. Since the specific cause(s) of variegation in a given transgenic line are generally not known, this issue is of pronounced significance for studies involving MeCP2 mutation. The potential causes of variegation include alterations in chromatin conformation, accessibility to transcriptional regulators, and gene silencing by methylation (Dobie *et al.*, 1997)—all phenomena in which MeCP2 may play a role. Consequently, any study of the neuromorphological effects of MeCP2 mutations that relies on a transgenic reporter must determine whether there is any interaction between the mutation and the transgene, to control for the introduction of systematic bias into the data.

Results

We first did a qualitative survey of cortical YFP expression patterns in mature mice from the hybrid YHM (Mecp2$^{tm1.}$/B6.Cg-Tg(Thy1-YFPH)2Jrs/J) mouse line. YFP expression varied in two significant ways (summarized in Fig. 10). First, the density of labelling varied with cortical region (Fig. 10D). The boundary between two adjacent areas of different YFP labelling density often closely corresponded to the cortical subregions denoted in the reference mouse brain atlas (Paxinos *et al.*, 2001). The highest densities of YFP expression tended to occur in rostral and medial regions such as motor, cingulate, and retrosplenial cortex, while the lowest densities tended to occur in caudal and lateral regions, such as visual, ectorhinal, entorhinal, and piriform cortex (see Fig. 10B and Fig. 15 in Chapter 5). Second, in most cortical regions, YFP density tended to be lower in MeCP2 mutant littermates relative to WT siblings (Fig. 10A-D). Certain regions also tended to be much more strongly affected than others. Figures 10A & 10C show a near absence of transgene expression in mutant visual and auditory cortex (red arrows), while adjacent retrosplenial and somatosensory cortex exhibit comparatively mild reductions. The severity of these differences was not always consistent between different breeding lines of YHM mice. Fig. 10D shows a qualitative heat map of median values for several major cortical regions from an examination of five WT/MeCP2 mutant littermate pairs obtained from five separate breeding lines.

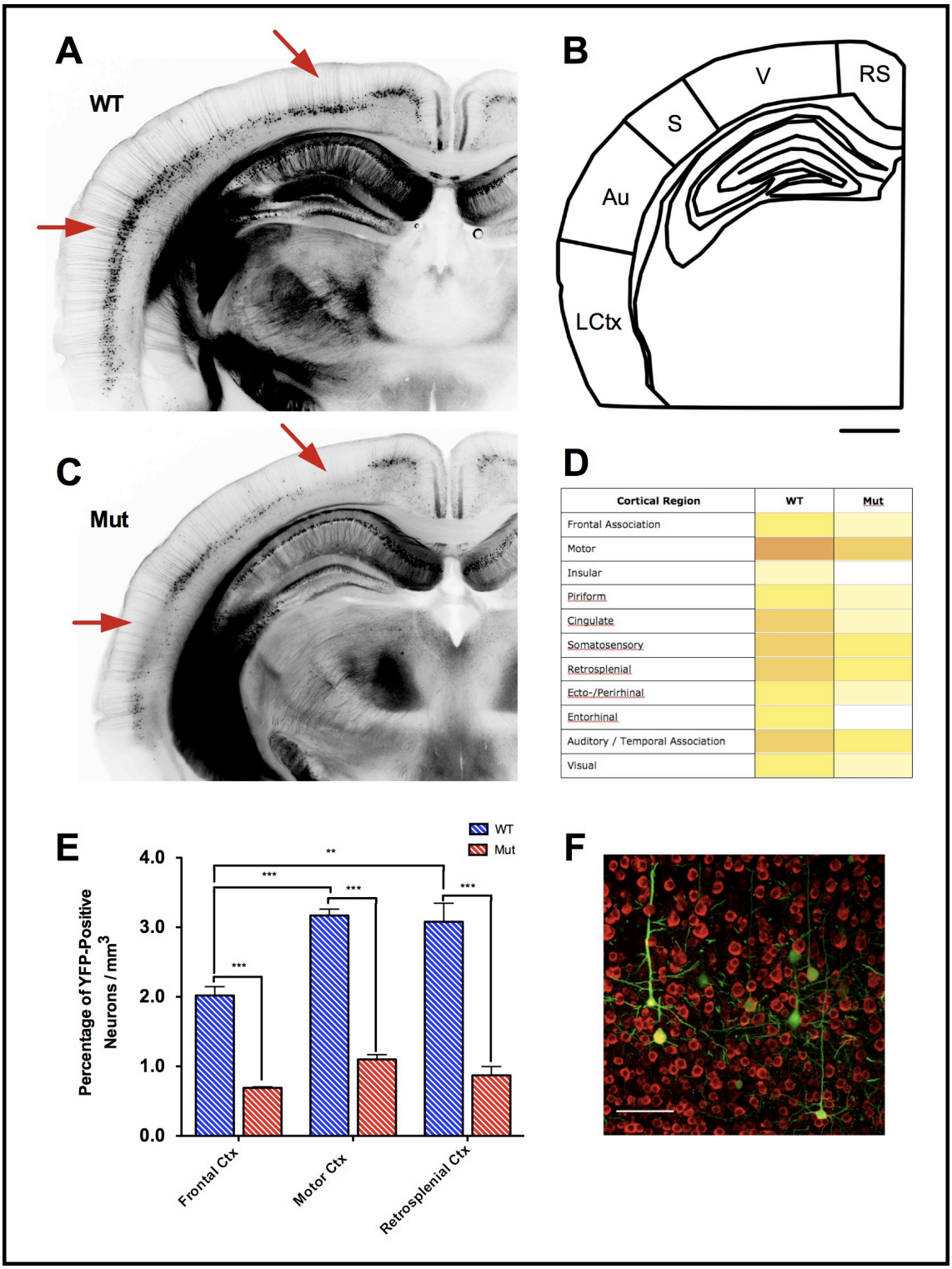
A
WT
B
V
RS
S
Au
LCtx
C
Mut
D
Cortical Region
WT
Mut
Frontal Association
Motor
Insular
Piriform
Cingulate
Somatosensory
Retrosplenial
Ecto-/Perirhinal
Entorhinal
Auditory / Temporal Association
Visual
E
WT
Mut
Percentage of YFP-Positive Neurons / mm3
4.0
3.0
2.0
1.0
0.0
**
***
***
***
***
Frontal Ctx
Motor Ctx
Retrosplenial Ctx
F

Figure 10. YFP expression varies with cortical region and MeCP2 status.

A, C) Coronal sections from WT YHM mouse (A) and MeCP2 mutant littermate (C). The grayscale values are inverted for visual clarity. All coronal sections shown correspond to ~ -2.1 mm ± 0.1 from Bregma. Red arrows indicate corresponding cortical regions showing striking differences in the density of YFP expression. B) Schematic of cortical regions most closely matching brain slices in A and C. Note that these broad cortical regions have further subdivisions (not shown) which frequently correspond to abrupt changes in YFP density seen in the tissue sections. Scale bar = 1 mm. RS, retrosplenial; V, visual; Au, auditory; LCtx, lateral cortex (including temporal associational, ectorhinal, perirhinal, entorhinal, and piriform cortex). D) Qualitative heat map showing median YFP expression in different cortical regions (white represents few to no cells; dark orange represents the highest estimated density). E) Percentage of YFP-expressing neurons in 3 cortical regions. YFP density is significantly lower in all 3 areas. In WT mice, YFP density is also lower in frontal association cortex relative to motor and retrosplenial cortex. F) Layer 5 motor cortex in a MeCP2 mutant mouse showing Neurotrace Nissl stained somata and YFP-expressing pyramidal neurons**.** Scale bar = 100 μm.

We quantified the percentage of YFP-positive neurons in three cortical areas (frontal association, motor, and retrosplenial, Fig. 10E, Table 3). A significant interaction was detected by one-way ANOVA ($F_{5,17}$ = 63.36, P < 0.0001). In all three regions, the percentage of YFP-expressing neurons was significantly lower in mutant mice relative to WT (Bonferroni's multiple comparison test; t_5 > 6.751, P < 0.001 in all pairs). Within WT animals, the percentage of YFP-positive neurons was also lower in frontal cortex relative to motor and retrosplenial cortex ($t_5 \geq 5.381$, P < 0.01). No significant difference was found between cortical regions in the mutant mice. It should also be noted that the reduced proportions of YFP-expressing neurons observed in mutant mice were detected in spite of the increased neuronal densities in L5 (Chapter 2, Fig. 6). These data were not normalized since a significant difference was already detected. In summary, these results confirm that MeCP2 mutation reduces expression of the *Thy-1-YFP* transgene in the YHM line. The qualitative observations of stark region-specific silencing also suggest a substantial heterogeneity of this interaction depending on cortical region (Fig. 10A, 10C). This is not strongly indicated by the quantitative data, which examined only a limited number of regions, but would likely be detected if quantification measures were repeated in areas such as visual cortex.

	Percentage YFP Expression (% / mm^3)	
Cortical Region	**WT**	**Mut**
Frontal Associational	2.02 ± 0.13	0.69 ± 0.02
Motor	3.17 ± 0.09	1.1 ± 0.07
Retrosplenial	3.08 ± 0.27	0.87 ± 0.13

Table 3. Percentage of YFP-expressing neurons in different cortical regions.

MeCP2 is known to participate in non-specific gene silencing as well as direct promoter interactions, and has been shown to both upregulate and downregulate gene expression (Nan and Bird, 2001; Chahrour *et al.*, 2008; Urdinguio *et al.*, 2008; Ben-Shachar *et al.*, 2009). The reduced YFP expression observed in the MeCP2 mutant animals could therefore be a consequence of either of two effects: altered patterns of silencing of the YFP transgene, or a general downregulation of YFP levels, such that weak expressors are sufficiently faint to fall below the level of detection by fluorescence imaging. Given the similar imaging conditions used for all our tissue samples, casual observation of the confocal fluorescence image data strongly suggests the first scenario. As previously shown in Chapter 2 (Fig. 7B), YFP fluorescence intensity occurs over similar ranges of very bright and faint cells in both genotypes, independently of cell size. The frequency distribution of these data is shown in Figure 11. Although there are approximately twice as many WT cells in the highest-intensity bin, this relationship is inverted at slightly lower intensities in the next two bins; the number of cells for each genotype in the highest quartile is nearly identical. The distributions in the two groups did not significantly differ (WT median = 2710; Mut median = 2649; Mann–Whitney U = 830, $n_{WT} = 43$, $n_{Mut} = 46$, $P > 0.05$). While these data are not statistically adequate (only two animals were examined) they support our informal observations in all animals that YFP is not merely fainter in the mutant mice; rather, the transgene has failed to express in a larger proportion of cells relative to the WT.

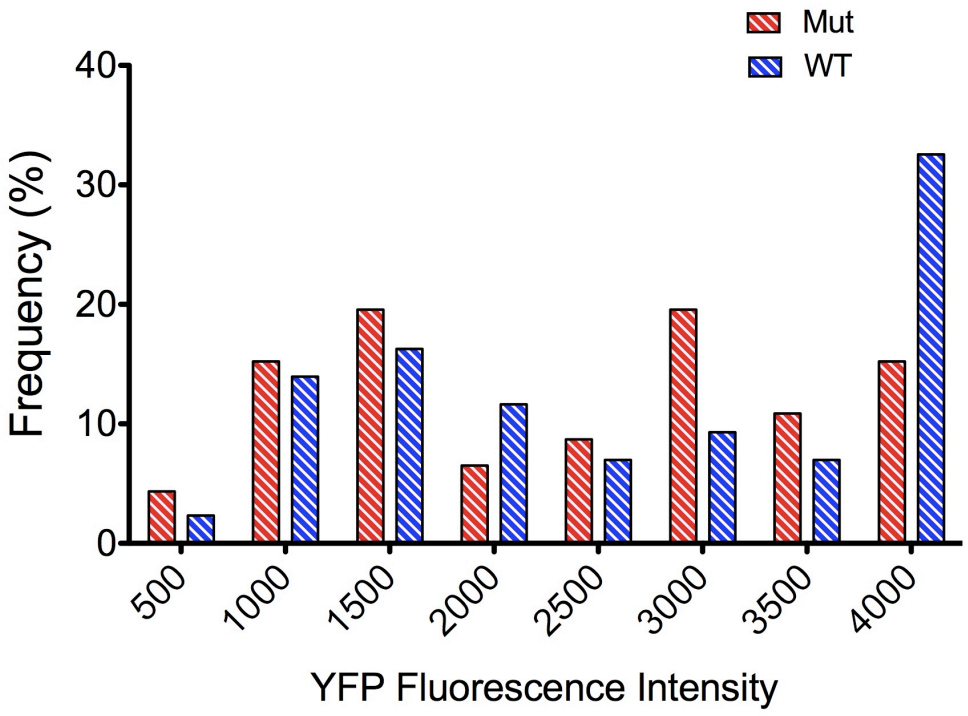

Figure 11. Frequency distribution of L5 pyramidal cell YFP fluorescence intensities. Distribution based on the fluorescence intensity data presented in Fig. 7B. $n_{WT} = n_{Mut} = 1$, with 46 cells in the WT and 43 cells in the mutant.

We hypothesized that if the reduction in YFP expression in mutant mice from the YHM line was the result of a non-obligate, promoter-dependent interaction, then a similar reduction in YFP should be observed in a second *Thy-1-YFP* transgenic line. We tested this possibility by crossing MeCP2 mutant mice with the YFP-16 line (B6.Cg-Tg(Thy1-YFP)16Jrs/J) (Feng *et al.*, 2000). The YFP-16 line has the same *Thy-1-YFP* expression cassette as YFP-H, but expresses YFP in the majority of cortical neurons (Fig. 12B). As a result of the high background, individual neurons cannot be easily counted in the YFP-16 brain sections, so YFP levels were quantified by measuring the mean cortical fluorescence over a large area incorporating cingulate, motor and somatosensory cortex (Fig. 12A). The normalized levels of YFP fluorescence did not significantly differ between the two genotypes (WT: 21.63 % ± 4.06; Mut 15.42 % ± 2.163; $n_{WT} = 7$, $n_{Mut} = 6$; $t_{11} = 1.282$, $P = 0.2262$). Although we cannot rule out the possibility that different

patterns of transgene multimerization and insertion site alter interactions with transcriptional machinery, this result also suggests that a direct promoter interaction is not the source of reduced YFP expression in mutant YHM mice, either via MeCP2 or indirectly via another transcriptional regulator downstream of MeCP2.

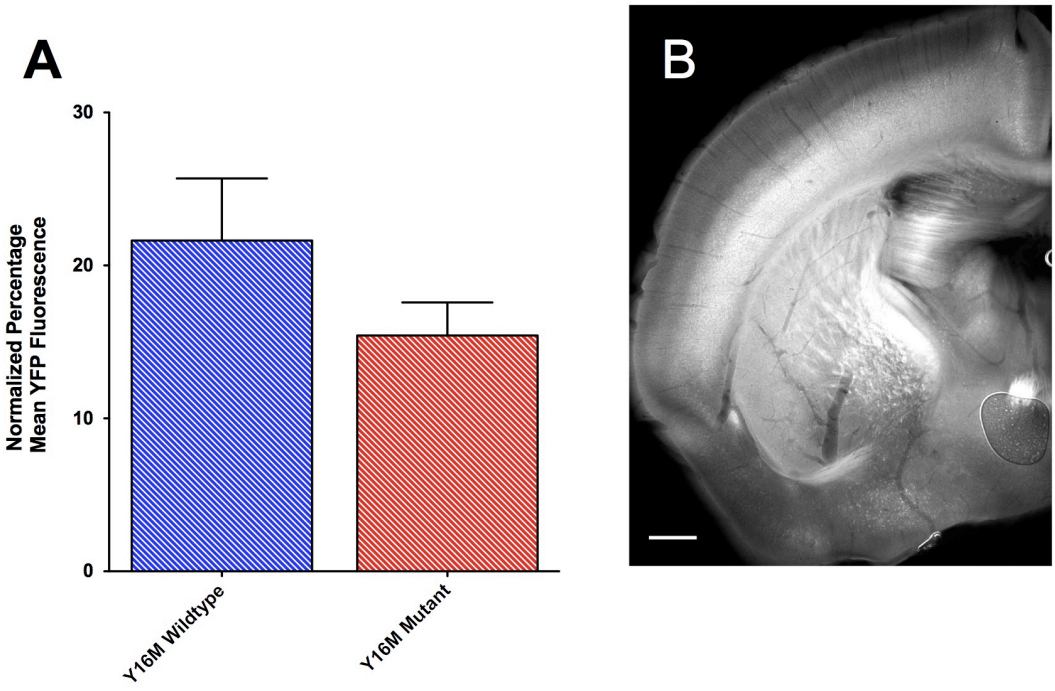

Figure 12. YFP intensity is independent of MeCP2 status in the YFP-16M line.

A. Normalized intensity of YFP fluorescence is not significantly different in 9-week old MeCP2 mutant mice relative to WT (n = 6 Mut, 7 WT). B. Coronal section from Y16M WT mouse. YFP is expressed all cortical neurons. Scale bar = 0.5 mm.

Discussion

We find that MeCP2 mutation results in a significant reduction in the number of YFP-expressing neurons in the hybrid YHM line that does not appear to be replicated in a second line that expresses the same *Thy-1-YFP* transgene in a different population of neurons. The observed reductions in YHM mutant mice also appeared to vary depending on the cortical regions involved. The unique expression patterns from *Thy-1-XFP* constructs (where X is a GFP-based fluorophore) have previously been considered

stochastic effects arising from the random chromosome insertion site and transgene copy number for a given transgenic mouse line (Feng *et al.*, 2000). In this context, the effect of MeCP2 mutation on YFP expression was an unexpected consequence of our breeding program. *Mecp2* mutation alters both neuronal morphology as well as expression patterns of the reporter transgene, so this introduces a very important caveat to these results. A consistent and ordered effect on YFP expression suggests the possibility of a systematic bias which must be addressed when interpreting the data. The recent finding showing that the YFP-expressing cells in the motor cortex YFP-H mice constitute a functional subclass of L5 pyramidal cells (Yu *et al.*, 2008) raises the possibility that YFP expression is at least partially non-stochastic, in which case the interaction of *Thy-1-YFP* with mutant MeCP2 could turn out to be both informative and experimentally valuable. This scenario is discussed in Chapter 4.

Establishing the mechanism of the interaction between MeCP2 and *Thy-1-YFP* was beyond the scope of this thesis, and as such the principal aim of the experiments described in this chapter was to assess whether there was a consistent quantitative effect of MeCP2 mutation on YFP expression. Nevertheless, the Thy-1 protein itself exhibits a host of properties that are tantalizingly suggestive of a potential interaction between the *Thy-1* gene and MeCP2, and a brief discussion is warranted.

Thy-1, also called CD90, is a cell surface glycoprotein that is widely expressed in the CNS neurons (Raff *et al.*, 1979; Brown and Waneck, 1992). Thy-1 expression is regulated by DNA methylation (Sneller and Gunter, 1987; Szyf *et al.*, 1990) and is largely postnatal, increasing into adulthood (Morris, 1985; Barlow and Huntley, 2000). Like MeCP2, the complex spatiotemporal patterning of Thy-1 expression suggests a variety of roles in structural/functional maturation that proceed independently of the timing of neurogenesis, migration, dendritic & axonal growth, but which are compatible with synapse generation and maintenance (Bolin and Rouse, 1986; Barlow and Huntley, 2000; Barlow *et al.*, 2002). Expression is developmentally regulated in terms of cell compartments, suggesting a role in the stabilization of neurites. Thy-1 appears on somata and dendrites earlier than axons, where it is detected only after axonal growth is complete

(Xue *et al.*, 1990; Xue *et al.*, 1991; Xue and Morris, 1992; Morris *et al.*, 1992). Thy-1 interactions with astrocytic integrins trigger the formation of focal adhesions, which appear to participate in neurite stabilization through interactions with the surface membrane and/or underlying cytoskeleton (Mahanthappa and Patterson, 1992a; Mahanthappa and Patterson, 1992b; Avalos *et al.*, 2002; Avalos *et al.*, 2004). Thy-1 is also detected in some populations of synaptic vesicles (Stohl and Gonatas, 1977; Jeng *et al.*, 1998).

The patterns of *Thy-1-XFP* transgene expression tend to be in subsets of cells that normally express Thy-1 (Feng *et al.*, 2000), and elevated *Thy-1* expression has been specifically demonstrated in isolated populations of YFP-expressing L5 pyramidal neurons in cingulate and somatosensory cortex, as well as hippocampus and amygdala (Sugino *et al.*, 2006). Nevertheless, no RTT gene expression study to date has revealed any dysregulated expression of *Thy-1* in human beings or in MeCP2 mutant mice. It remains to be determined whether this will be the case for transcriptional profiling analyses of more precisely fractionated populations of neuronal subtypes. The trend thus far suggests it's worth a bet.

Chapter 4: Conclusions & Future Directions

We examined a population of YFP-expressing Layer 5 pyramidal neurons in a Rett Syndrome mouse model. Neurons in *Mecp2*$^{-/y}$ mice exhibited morphological alterations including reduced soma size and selective alterations in apical and basal dendritic arbors. While most dendritic variables examined revealed a general trend towards reduced size and complexity in mutant cells, statistically significant differences were predominantly found the basal compartment. In mutant neurons, somatic area was reduced by 24.1%, total basal dendritic length was 18.6% shorter, and the maximum length of individual dendrites was 9.1% shorter relative to the wildtype. The largest differences in basal dendritic branching occurred proximal to the soma, the region of greatest synaptic connectivity in WT L5 pyramidal cells. The apical compartment was less severely affected but did show significantly shorter dendritic lengths in the apical tuft, reflecting less tangential branching in the molecular layer. Consistent with these data, the brains of mutant mice had increased neuronal density in Layer 5 in motor cortex, as well as in frontal and retrosplenial cortex. These results extend and confirm previous findings in MeCP2 mutant mice and human RTT patients.

We also report an unexpected interaction between the *Thy-1-YFP* reporter transgene and MeCP2 that resulted in a reduction in the number of YFP-expressing neurons in MeCP2 mutant mice. This effect was restricted to hybrid YFP-MeCP2 mice descended from the YFP-H line, B6.Cg-Tg(Thy1-YFPH)2Jrs/J. No significant effects were detected in mice descended from a related *Thy-1-YFP* transgenic line, YFP-16 (B6.Cg-Tg(Thy1-YFP)16Jrs/J). Previous studies have shown that the *Thy-1* promoter cassette is highly sensitive to multimerization and/or chromosome insertion site effects. We conclude that reduced number of YFP-expressing cells in the MeCP2 mutant condition is most likely the result of non-specific effects arising from altered chromatin conformation.

Future Directions

The principal consequence of reduced dendritic branching in *Mecp2* mutant L5 pyramidal neurons that remains to be determined is the degree to which it alters synaptic

connectivity. The effects of MeCP2 deficiency on dendritic spine density should be examined by conducting spine counts in each dendritic compartment, including proximal and distal basal dendrites, the primary apical dendrite, and higher-order branches in the apical tuft. Based on previous findings in other cortical layers, it is likely that spine density is not significantly different in L5 pyramidal neurons, but the shorter dendritic branching would still reduce total synaptic connectivity. The reduced branching and soma size shown in our data suggest the likelihood of smaller minicolumns in *Mecp2* mutant mice, but this also remains to be determined. Assessing minicolumn widths in conjunction with proximal and distal synaptic densities in these neurons would generate a number of testable hypotheses regarding the functional consequences on local intra- and transcolumnar connectivity and columnar output, as discussed in Chapter 2. Several techniques have been demonstrated in electrophysiological studies of acute slices from sensorimotor cortex, which could also be used to examine patterns of synaptic input at many levels: in subcellular compartments of single cells, between pairs of connected neurons, or at the columnar level, involving thousands of neurons (Shepherd *et al.*, 2005; Schubert *et al.*, 2007; Petreanu *et al.*, 2009). These experiments will be instrumental in establishing the relationships between altered neuron morphology, connectivity, and physiology in MeCP2-deficient cells.

The present study examined a subpopulation of YFP-expressing neurons in the motor cortex. Although the pattern of YFP expression in these cells was originally considered stochastic, recently published data and our own informal observations indicate that these may be composed of one or more neuronal subtypes (Yu *et al.*, 2008). Consequently an important experimental goal will be to determine whether the reduced expression of *Thy-1-YFP* we observe in YFP-H – MeCP2 mutant mice is restricted to one or more subsets of neurons. If the proportion of L5 subtypes that express YFP is similar between *Mecp2* genotypes, then *Thy-1-YFP* can be considered an unbiased marker for these cells. Alternately, if the reduced YFP expression is ordered, and not simply a stochastic consequence of dysregulated chromatin remodelling, then it is possible that YFP could function as a highly specific reporter gene for MeCP2 status in a very restricted neuronal

subpopulation. This raises the intriguing possibility that MeCP2 deficiency results in an imbalanced distribution of L5 pyramidal subtypes.

There are multiple avenues of approach for the question of the relationship between YFP expression and distributions of L5 pyramidal neuron subtypes which could be particularly fruitful if used in conjunction with each other. At a morphological level, neurons expressing YFP could be compared with randomly labelled neurons using methods such as single-cell injection of Lucifer Yellow or biocytin (Benavides-Piccione *et al.*, 2006; Belichenko *et al.*, 2009). Multidimensional principal component analysis of these data in both WT and MeCP2 mutant mice would ascertain whether YFP expression is stochastic or differentially restricted in morphological subtypes (Tsiola *et al.*, 2003). Different projection classes of L5 neurons could also be identified by retrograde labelling from multiple distal axonal projection sites such as the thalamus, striatum, tectum or contralateral cortex or by immunolabeling distinctive molecular markers (Voelker *et al.*, 2004; Hattox and Nelson, 2007). In conjunction with electrophysiological studies, these experiments could therefore simultaneously address questions regarding the degree of stochasticity of *Thy-1-YFP* expression, the distributions of L5 pyramidal neuron subtypes in WT and MeCP2 mutant mice, and whether these subtypes are differentially affected by MeCP2 deficiency. The latter two questions are of particular relevance to elucidating the complex role of MeCP2 in the CNS.

Although somewhat tangential to the principal focus of this thesis, it should be noted that the interaction MeCP2 with *Thy-1-YFP* could also provide a fruitful avenue of research, especially in light of the increasing use of *Thy-1-XFP* transgenic mice in RTT mouse model studies (e.g. (Belichenko *et al.*, 2009)). One obvious question to be addressed is whether there are any direct promoter-specific interactions between MeCP2 or some downstream effector with the neuron-specific transgenic *Thy-1* expression cassette or the *Thy-1* gene itself. Since one of the roles of MeCP2 is to silence genes via heterochromatin condensation, the fact that YFP expression is *decreased* in MeCP2 mutant mice raises some interesting possibilities. Chromatin immunoprecipitation assays

would be a valuable inroad to identifying any protein-DNA interactions that could be involved.

As a final consideration, the data presented in this study were obtained from male mice. Since MeCP2 is an X-linked gene, this represents a simplified experimental condition because all neurons in these animals are hemizygous for either the WT or mutant allele. Rett Syndrome is a disorder that primarily affects females, however, and as a result, a long-term goal of these experiments will be to establish how the mosaic expression of MeCP2 affects individual neurons. Both cell-autonomous and nonautonomous effects have been documented in female mice heterozygous for *Mecp2* (Belichenko *et al.*, 2009). In addition to the effects of modifier genes and mutation types, an interesting question remains as to whether there are non-linear effects on the physiology and morphology of neurons in the females as a result of skewed X chromosome inactivation. Skewed XCI may have more extreme effects in mutant neurons due to competition with WT neurons. This may be of particular significance for small populations of neurons with widespread regulatory effects or control of vital autonomic functions, such as those in brainstem nuclei (Viemari *et al.*, 2005; Taneja *et al.*, 2009).

Chapter 5: Methods

Animal Breeding

Mecp2 $^{-/+}$ heterozygous female mice (*Mecp2*$^{tm1.1Jae}$/Mmcd) on a mixed, predominantly 129/Sv background (Chen *et al.*, 2001) were obtained from the Mutant Mouse Regional Resource Center (MMRRC; UC Davis) and crossed with WT 129S2/SvPasCrl males (Charles River, Raleigh NC). Backcrossed littermates produced very small litters with a high rate of cannibalism, so F1 *Mecp2* $^{-/+}$ heterozygous females were bred with an independently maintained 129S2/SvPasCrl line. *Mecp2* allele status was determined by genotyping (Fig. 14).

Male transgenic mice from the "YFP-H" line (B6.Cg-Tg(Thy1-YFPH)2Jrs/J) (Feng *et al.*, 2000), on a C57BL/6J background and heterozygous for the YFP transgene, were crossed with an independently maintained C57BL/6J line (both from Jackson Laboratory, Bar Harbor, ME). *YFP* $^{+/-}$ littermates were bred to homozygosity for the YFP transgene for 2 - 3 generations. *YFP* status was established by earclip phenotype (Fig. 13) or by genotyping (Fig. 14).

All neuron morphometry experiments used F1 hybrid *YFP* $^{+/-}$ / *Mecp2* $^{-/y}$ or *Mecp2* $^{+/y}$ males (STOCK Tg(Thy1-YFPH) 2Jrs *Mecp2*$^{tm1.1Jae}$, referred to as "YHM"). Hybrid line nomenclature follows recommendations in Eppig (2006). These mice were generated by crossing *YFP* $^{+/+}$ males with *Mecp2* $^{+/-}$ females. The *YFP* $^{+/+}$ males used were obtained from the second or third inbred generation. A second line of "YFP-16" transgenic mice (B6.Cg-Tg(Thy1-YFP)16Jrs/J, Jackson Laboratory) was also obtained for experiments assessing the effect of *Mecp2* status on the YFP transgene under the *Thy-1* promoter. Heterozygous *YFP* $^{-/+}$ males were bred against *Mecp2* $^{-/+}$ dams and YFP-positive F1 male littermates expressing either WT or mutant MeCP2 were used in experiments.

Mouse colonies were maintained at the University of Victoria Animal Care Unit using protocols approved by the Animal Care Committee, consistent with Canadian Council on Animal Care and Use guidelines. Animals were fed Laboratory Rodent Diet 5001 (Lab Diets; St. Louis, MO), had water *ad libitum*, and were kept at 21°- 22°C under 12 hour light/dark cycles. To reduce the incidence of infanticide and cannibalism, breeding cages with *Mecp2* $^{-/+}$ females were left undisturbed and Black Oil Sunflower seeds were added to cages for three days pre- and postparturition (Jugloff *et al.*, 2006).

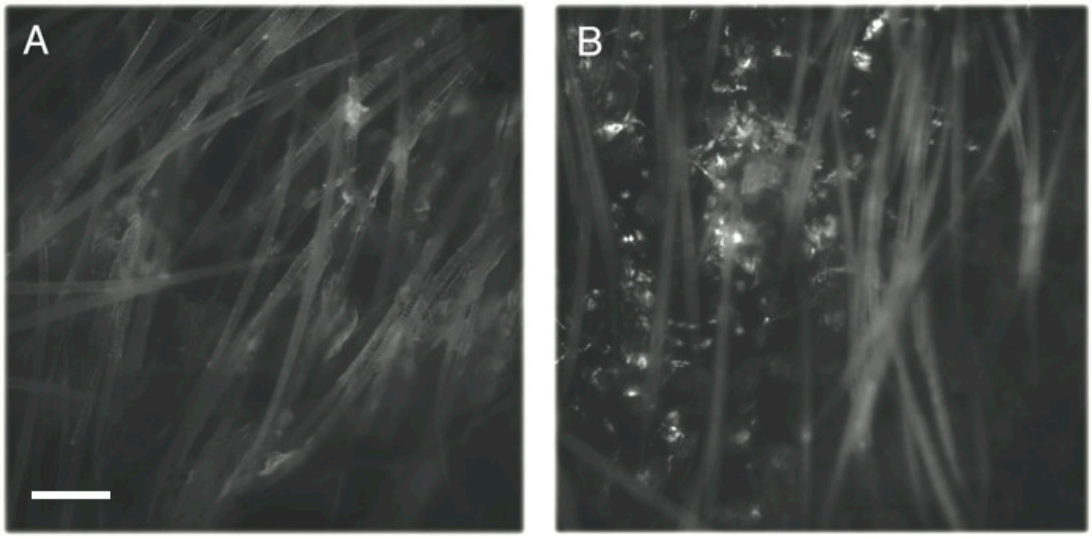

Figure 13. Phenotypic identification of YFP-positive transgenic mice.

A) No YFP fluorescence is observed in wild-type mice (hairs exhibit autofluorescence). B) YFP punctae from sensory neurons are seen in mice heterozygous for the YFP transgene. Scale bar = 0.5 mm.

Genotyping

Genomic DNA was extracted from ear clips using a Qiagen QIAmp DNA Mini Kit (Hilden, DE). PCR amplifications were performed using a Biometra T3 Thermocycler (Göttingen, DE) using PCR primers from Alpha DNA (Montreal, QC).

PCR amplification of *Mecp2* sequences used 0.5 u Phusion High-Fidelity DNA Polymerase (Finnzymes, Espoo, FI), 1X Phusion HF buffer (F-518), 200 µM dNTPs, 1

μM each of forward and reverse primers and 10 – 25 ng of genomic DNA in a final reaction volume of 25 μl. Phusion polymerase permitted simultaneous amplification of both the mutant and WT *Mecp2* sequences. Forward and reverse primer sequences were [5'– cac cac aga agt act atg atc –3'] and [5'- atg ctg aca agc ttt ctt cta –3'], respectively. The PCR program was 30s initial denaturation at 98°C; 7 cycles of 10 s denaturation at 98°C for 10s, 30 s annealing at 65°C to 59°C (decreasing 1°C per cycle), and 90s elongation at 72°C, followed by twenty-three cycles of 10 s denaturation at 98°C, 30 s annealing at 58°C, and 90 s elongation at 72°C . A final elongation at 72°C for 5 minutes was performed then the product was kept at 4°C for up to 24 h. A 3 kb amplicon indicated the WT allele and a 250 bp amplicon indicated the mutant allele (Fig. 14).

PCR amplification of *YFP* was performed using 1 u Taq polymerase (Invitrogen, Carlsbad, CA), 1X Taq buffer, 200 μM dNTPs, 2 mM $MgCl_2$, 1 μM of each primer, and 10 – 25 ng of genomic DNA in a 25 μl final reaction volume. Forward and reverse primers were ThyF1 [5'- tct gag tgg caa agg acc tta gg -3'] and E-YFP R1 [5'- cgc tga act tgt ggc cgt tta cg –3'], respectively. The Touchdown PCR program was 150 s initial denaturation at 94°C; 5 cycles of 20 s denaturation at 94°C, 30 s annealing at 60°C to 56°C decreasing by 1°C each cycle, and 30 s elongation at 72°C; followed by twenty-five cycles of 20 s denaturation at 94°C, 30 s annealing at 55°C , and 30 s elongation at 72°C. A final 60 s elongation step at 72°C was performed then the product was kept at 4°C for up to 24 h.

PCR amplification products were run with a 1Kb DNA ladder (Invitrogen) on a Tris-acetate-EDTA (TAE) 1% agarose gel. Gels were stained with 1X Sybr Safe (Invitrogen) and visualized in a UVP BioDoc-It Imaging System UV transilluminator (Upland, CA).

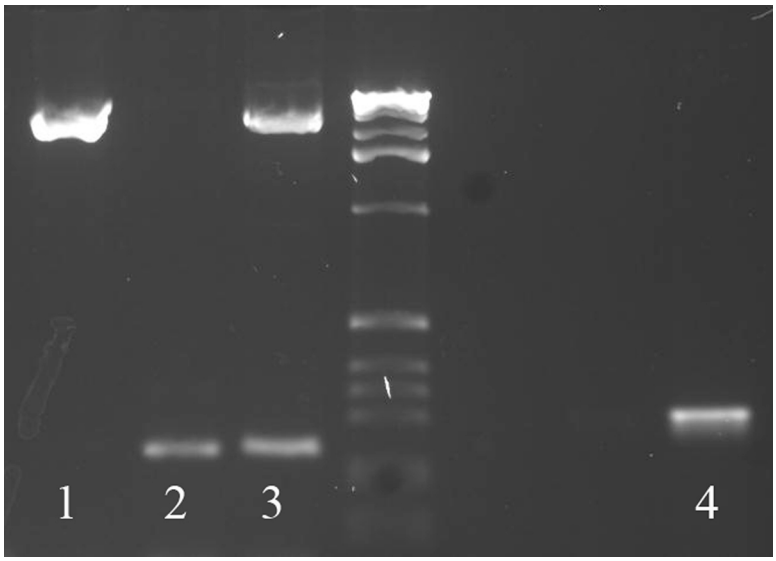

Figure 14. Genotyping for *Mecp2* and *YFP* sequences.

1) 3 kb band, *Mecp2* wildtype 2) ~250 bp band**,** hemizygous *Mecp2* mutant male 3) 3 kb and 250 bp band, heterozygous *Mecp2*$^{+/-}$ female 4) 300 bp band, YFP transgene.

Perfusion and dissection

Anaesthesia was induced by placing mice in a sealed chamber containing ~ 0.5 ml isoflurane dabbed onto a kimwipe. Mice were then given an i.p. injection of ~ 0.5 ml urethane (0.15 g / ml). Depth of anaesthesia was tested by paw-pinch. With the animal pinned through the front paws in dorsal recumbency, the fur was wetted with 70% ethanol and a cut was made along the midline of the ventral skin to above the ribcage. Two more lateral cuts were made in the skin just below the ribcage followed by a small cut the in diaphragm to collapse the lungs. Lateral cuts in the diaphragm parallel to the midline were made on each side of the ribcage. The xiphoid cartilage was clamped with a hemostat and folded back to expose the heart. An ~ 1mm incision was made into right atrium to allow blood to exit the circulatory system, and remaining blood was rinsed out by injection of 10 ml ice cold phosphate buffered saline (PBS), pH 7.4, into the left ventricle (10mL syringe, 27.5 gauge needle) over ~ 60 - 120 s. Exsanguination was confirmed by a change in liver colour from deep burgundy to tan. 10 ml of room temperature 4% paraformaldehyde in PBS, pH 7.4 (hereafter 4% PFA) was perfused in similar fashion. Mice were decapitated, and the dorsal surface of the brain case was removed. The entire skull with exposed brain tissue was soaked in 4% PFA at RT for 2 h

then overnight at 4°C. Brains were dissected out, rinsed in PBS, and returned to fresh 4% PFA for 24 h at 4°C. Following fixation brains were washed 3X in PBS. Brain weight measurements were taken after blotting with kimwipes to wick liquid out of cerebral fissures, and cutting the spinal cord at the medulla. Brains were stored in a 30% sucrose PBS solution with 0.01% sodium azide at 4°C until sectioned and mounted.

Sectioning, Counterstaining, and Mounting of Brain Slices

Brains were blocked and embedded in 2.5 % agar in PBS and 200 μm coronal sections cut on a on Vibratome Series 1000 (Speed 0.5, amplitude 6.5, blade angle 18°) and stored in PBS until mounted. In some brain slices, neuron somata were counterstained using Neurotrace 530/615 (Invitrogen). Slices were permeabilized in PBS, pH 7.2 with 0.1% Triton-X (ICN Biomedicals, Aurora OH) for 1 hr, washed 3 x 5 min in PBS, then incubated in 1:100 Neurotrace in PBS in dark conditions for 2 h at RT. Slices were washed 3 x 5 min then washed overnight at 4°C. Sections were mounted on aminosilane-coated slides with Shandon Immunomount (Thermo Scientific, Pittsburgh, PA), covered with 170 μm (No. 1.5) coverslips, cured overnight at room temperature in dark conditions, then sealed with nail polish.

Fluorescence Imaging

All confocal image stacks used for morphological and density analysis were obtained using a Nikon Eclipse TE2000-U confocal microscope and Nikon EZ-C1 3.60 software. For reconstructions of apical and basal compartments of YFP-H neurons, 1024 x 1024 pixel images were obtained using a 1.30 NA 40X Nikon S Fluor oil immersion lens using a consistent range of imaging conditions (433 nm laser, scan speed of 1.68 – 3.94 μs/pixel, z-step of 400 nm, gain 5.5 – 6.5, averaging of 2, 30 μm pinhole). Laser power and gain were manually adjusted during imaging to maintain maximal subsaturation pixel intensities at the apical dendrite. Image stacks were converted to 16-bit .tif files using ImageJ software (http://rsbweb.nih.gov/ij/).

1600 x 1200 pixel widefield images of cerebral hemispheres for YHM and Y16M mice were obtained using an Olympus IX70 inverted epifluorescence microscope (Center

Valley, PA), and photographed with a Retiga 2000R digital CCD camera (QImaging, Surrey, BC).

Morphological Analysis of YFP-Expressing L5 Pyramidal Neurons

Soma traces and dendritic analyses were performed on 10 YHM mice ($n_{WT} = n_{Mut} = 5$) in mature mice 8-18 weeks old. Three WT/mutant pairs of mice were littermates. One additional 13-week old MeCP2 mutant mouse was used in the soma tracing. Soma and dendritic traces were independently performed by a single observer blind to age and genotype. Coronal sections containing motor cortex were identified with reference to two brain anatomical markers, the corpus callosum and the anterior commissure (see Fig. 15). All confocal stacks were obtained from brain sections between the section immediately anterior to the first appearance of the corpus callosum to the last section in which the anterior commissure bridges the two hemispheres (~2 mm). The cortical volume occupied by motor cortex over this rostral-dorsal range is sufficiently broad to ensure that imaged neurons were not from adjacent cortical regions.

Soma traces were performed using ImageJ software. All YFP-positive somata were outlined and areas measured using Image J. Somata were outlined in the focal plane where each cell has its maximum in-focus area. Partially occluded cell bodies at the image boundaries were not used. Prior to outlining each cell, the image was zoomed 12X. Post-hoc analysis of the mean signal:background ratio defining the cell boundary was determined by examining 12 neurons randomly selected from previous traces in two YHM littermates ($n_{WT} = n_{Mut} = 1$). The YFP fluorescence intensity was ≥3X background with a mean of 7.8X.

Dendrite traces were performed on confocal image stacks using Igor Pro 6.05 software (Wavemetrics, Lake Oswego, OR) with the Migor 4 plug-in developed by Dr. Jamie Boyd (UBC). 3D traces of apical or basal compartments were generated using Migor with a Cintiq 21 UX interactive pen display (Wacom, Vancouver, WA). Apical and basal compartments were separately imaged to allow adequate resolution of fine dendritic branches in YFP-positive neurons. For basal compartments, image stacks were oriented

such that somata of YFP-positive Layer 5A pyramidal neurons were centered along the y-axis, to permit capture of the maximum length of dendritic branching possible, as well as a minimum of 100 μm of the apical dendrite. Somata were selected from a sub-volume of the z-stack defined by a zone of exclusion comprising ~100 μm from the outer edges of the x and y axes and the central 100 μm within the z-axis. At 40X magnification the field of view in the x-y axes is 318 μm^2. Due to variable shrinkage in the z-axis during the mounting process the excluded z-axis "guard zones" were of variable length but typically ~ 25 μm. Traces of the first 100 μm of the primary apical dendrite (and any secondary branches) were included as part of the basal compartment. For apical compartment traces, the pial surface of the brain was aligned parallel and contiguous with the upper boundary of the x-axis in the image plane, permitting capture of apical dendrite into deep Layer 3. A standard reference point for comparing dendritic structures was established by initiating all traces 300 μm from the pial surface. Traces were not included if obvious truncations of lateral branches occurred. 260 traces were completed for each compartment in each genotype (52 traces per compartment per animal, n = 5 mice in each condition).

The following morphological parameters were analyzed using Migor:

- 3D Sholl analysis was performed by counting the number of dendrites intersecting a series of concentric spherical radii at 10 and 20 μm intervals for basal and apical dendrite compartments, respectively.
- Sholl lengths were measured by summing all of the segments of dendrite length occurring between two consecutive concentric spheres (e.g. the sum total of all dendrite segments traced between 10 - 20 μm, 20 - 30 μm intervals etc.). Analysis of Sholl length was included to account for the possible occurrence of branching patterns not captured by Sholl cross analysis, particularly within the apical compartment, where near the pial surface, extensive lengths of lateral branches could be present that did not cross the defined Sholl interval.
- Total dendrite length measured the summed length of all dendrites in each compartment.

- Percent dendritic length as a function of branch order for apical and basal compartments. Branch order is defined by the number of branch nodes occurring following a given primary node. Dendrites with fewer branches will have more proportionally more branch length in lower branch orders.
- Maximum Sholl radius in the basal compartment measured the largest Sholl radius crossed by at least one dendrite. In the basal compartment values have a minimum radius of 100 μm because of the inclusion of the proximal 100 μm of the apical dendrite.

Analysis of YFP Cortical Expression Patterns and Neuron Density

Fixed brain tissue was obtained from 5 WT/mutant YHM littermate pairs 11-13 weeks old. 200 μm coronal sections of the entire brain (excluding the olfactory bulbs and cerebellum) were serially mounted for each mouse and imaged using widefield epifluorescence. The relative rostrocaudal position of each slice was determined with reference to coronal plates in the Paxinos Mouse Brain Atlas (Paxinos *et al.*, 2001) and approximately corresponded to atlas Figures 4-70. Due to the marked volume reduction in the mutant mouse brains, several distinctive anatomical features were used as reference points: fusion of the medial orbital cortex to the anterior olfactory bulb; disappearance of the rhinal fissure; fusion of the genu of the corpus callosum; emergence of the anterior commissure and third ventricle; appearance of the dentate gyrus; and appearance and separation of the medial mammillary nucleus. Cortical regions were then determined with reference to the brain atlas. In several instances the YFP expression patterns produced sharply delineated regions that corresponded closely to the boundaries indicated in the atlas. The general locations of the brain regions examined in detail in these experiments are shown in Fig. 15. After establishing the range of tissue sections over which a cortical region occurred, each region was assigned a score from 0 to 4 as a qualitative estimate of the number of large YFP-positive pyramidal cells. A score of 0 reflected very few or no cells and 4 indicated very dense labelling. These estimates provide a qualitative estimate only and represent subjectively obvious differences of how YFP expression varied from region to region. A median value of the score for each cortical region was taken from all

mice within each genotype and plotted using a heat map, where white = few to no cells and dark orange = highest density of YFP-expressing neurons.

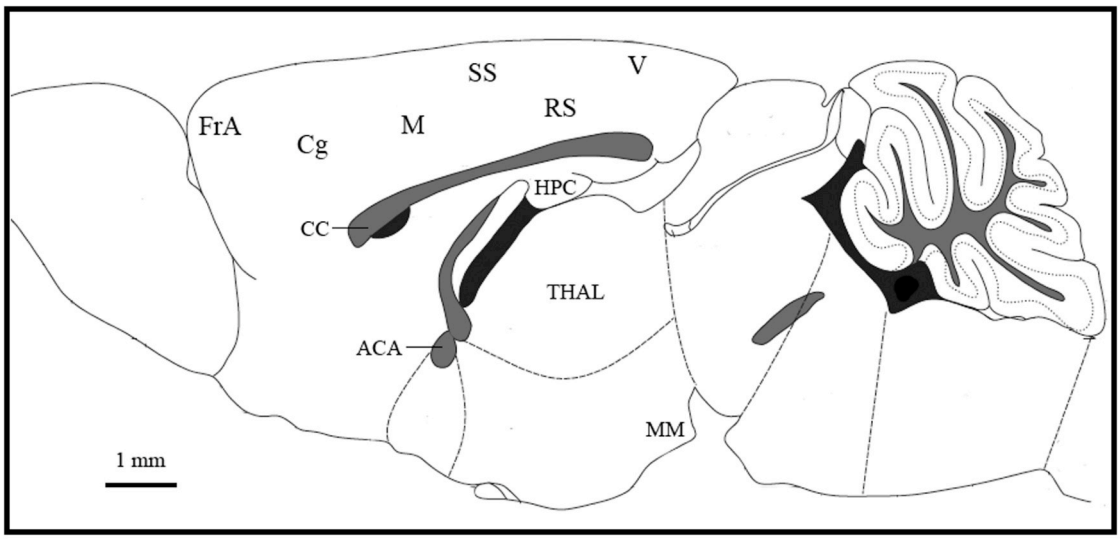

Figure 15. Brain regions examined in YHM mice.

Figure shows a schematic sagittal section of mouse brain illustrating brain regions examined or referenced in these experiments. Not all relevant cortical regions are shown. Labelled cortical regions indicate relative rostrocaudal position for illustrative purposes only and are not anatomically accurate. (Many in the diagram would not appear in the corresponding tissue section, ~ 0.25 mm lateral from the midline). Rostral regions are left, beginning with the olfactory bulb. Caudal regions are right, bounded by cerebellum and brainstem. Dorsal regions are at the top. Relative mediolateral positioning of cortical regions is approximately indicated by label position, with more lateral-tending regions (SS, V) shown above more medial-tending regions (Cg, M, RS). Labelled non-cortical structures are anatomically accurate. Black regions indicate ventricular spaces and grey regions indicate white matter fibre tracts. ACA, anterior commissure; CC, corpus callosum; Cg, cingulate cortex; FrA, frontal association cortex; HPC, hippocampus; M, motor cortex; MM, medial mammillary nucleus; RS, retrosplenial cortex; SS, somatosensory cortex; THAL, thalamus, V, visual cortex. Adapted from the Paxinos Mouse Brain Atlas (Paxinos *et al.*, 2001).

For measurements of neuron density and percentage of YFP-positive neurons, confocal stacks of 1024 x 1024 pixel images were obtained using an Nikon Plan APO NA 0.95 20X air lens with a consistent range of imaging conditions (simultaneous dual-channel excitation with 433 and 543 nm lasers, scan speed of 1.68 – 3.94 μs/pixel, z-step of 10 x 1 μm, gain 5.5 – 6.5 per channel, averaging of 2, 30 μm pinhole). Image stacks were

centered on Layer 5, distinctly visible as a double-blade of YFP-positive neurons (Yu *et al.*, 2008).

Neuron density and percentage of YFP-expressing cells were measured using a subset of the above brain slices that were labelled with the neuron-specific Nissl-type stain Neurotrace 530 / 615. Three WT/mutant littermate pairs were used. Five image stacks were obtained per brain for frontal association and retrosplenial cortex and 10 stacks per brain for motor cortex. Within each z-stack, the 5 (of 10) consecutive images with the brightest and most even Neurotrace staining were selected and flattened into a maximum intensity projection (MIP). Neurons were counted using the ImageJ CellCounter plugin. The count inclusion criteria were that cells must not be occluded by the image boundary, and that the Nissl stain must surround a clearly delineated nucleus, eliminating partially imaged cells from above and below the planes included in the MIP. For YFP cell counts, YFP-positive cells whose Nissl stains did not fit these criteria were similarly excluded.

Y16M Imaging

Coronal sections were prepared from 9 week-old Y16M mice ($n_{Mut} = 7$, $n_{WT} = 8$). One additional littermate from each MeCP2 genotype lacking the YFP-16 transgene was used for measurements of background tissue fluorescence. Images were taken from a series of five coronal sections defined by morphological markers observed in the coronal plane: the slice immediately anterior to the emergence of the corpus callosum, to the last slice in which the anterior commissure bridges the two hemispheres. These regions contain cingulate, motor, and somatosensory cortices. An entire hemisphere of each brain slice was imaged at 2X magnification. To eliminate fluorophore fading artifacts, brain slices other than those used for analysis were used to establish illumination conditions covering the greatest subsaturating range of grayscale pixel intensity values. All images were captured under identical illumination conditions (100% illumination, 150 ms, gain 1, no averaging). To compensate for signal dropoff in the corners of the image (relative to the center), an image mask was also generated to simulate flat illumination conditions across the entire image field. 10 μl of 10 mM fluorescein was centrifuged for 10 min (to pellet bright precipitate). 5 μl was withdrawn from the upper layer of solution, sandwiched

between two 22 mm^2 coverslips and imaged. The mask image was imported into ImageJ and converted to a 32-bit format. All pixels were then divided by the brightest pixel value and converted to the reciprocal, giving each pixel in the mask image a value ranging from 1 (center region) to 67 (outer corners). Brain slice images were multiplied by this image mask prior to further analysis.

The mean pixel intensity was measured for an outlined subregion of cortex for each intensity-corrected image. The traced region included cingulate, motor and somatosensory cortex, and was defined as the area bounded dorsally by the pial surface and ventrally by the dorsal surface of the corpus callosum. The ventrolateral boundary of the cortical perimeter was arbitrarily defined as a horizontal line bisecting the brain slice at the midpoint between the most distal dorsal and ventral points in the coronal section. This line corresponds roughly to the boundary between somatosensory and insular cortex (Paxinos *et al.*, 2001). Measurements from the non-YFP-expressing brains were used to subtract background fluorescence. Corrected mean pixel intensity for each image was then normalized by dividing into the maximum 16-bit grayscale intensity value (65,535) and expressing the final value as a percentage. An average of the 5 replicates per mouse was used in the statistical analysis.

Statistical Analysis and Figures

Statistics were performed using Prism 5 v.5.0b (Graphpad Software, Inc.) and R v.2.9.2 (WU; Wien, Austria). Unless otherwise stated, all parameters were analyzed using the two-tailed unpaired student's t-test and results considered significant at $P < 0.05$, with measurements reported as mean ± SEM. Dataset distributions were tested for normality using D'Agostino & Pearson omnibus normality test. Figures were prepared using Prism 5, ImageJ, and Photoshop CS3 v.10.0 (Adobe; San Jose, CA).

Bibliography

Aber KM, Nori P, MacDonald SM, Bibat G, Jarrar MH, Kaufmann WE (2003) Methyl-CpG-binding protein 2 is localized in the postsynaptic compartment: an immunochemical study of subcellular fractions. Neuroscience 116:77-80.

Adler DA, Quaderi NA, Brown SD, Chapman VM, Moore J, Tate P, Disteche CM (1995) The X-linked methylated DNA binding protein, Mecp2, is subject to X inactivation in the mouse. Mamm Genome 6:491-492.

Altamura C, Dell'Acqua ML, Moessner R, Murphy DL, Lesch KP, Persico AM (2007) Altered neocortical cell density and layer thickness in serotonin transporter knockout mice: a quantitation study. Cereb Cortex 17:1394-1401.

Amir RE, Van den Veyver IB, Schultz R, Malicki DM, Tran CQ, Dahle EJ, Philippi A, Timar L, Percy AK, Motil KJ, Lichtarge O, Smith EO, Glaze DG, Zoghbi HY (2000) Influence of mutation type and X chromosome inactivation on Rett syndrome phenotypes. Ann Neurol 47:670-679.

Amir RE, Van den Veyver IB, Wan M, Tran CQ, Francke U, Zoghbi HY (1999) Rett syndrome is caused by mutations in X-linked MECP2, encoding methyl-CpG-binding protein 2. Nat Genet 23:185-188.

Armstrong D, Dunn JK, Antalffy B, Trivedi R (1995) Selective dendritic alterations in the cortex of Rett syndrome. J Neuropathol Exp Neurol 54:195-201.

Armstrong DD (2001) Rett syndrome neuropathology review 2000. Brain Dev 23 Suppl 1:S72-S76.

Armstrong DD (2005) Neuropathology of Rett syndrome. J Child Neurol 20:747-753.

Armstrong DD, Dunn K, Antalffy B (1998) Decreased dendritic branching in frontal, motor and limbic cortex in Rett syndrome compared with trisomy 21. J Neuropathol Exp Neurol 57:1013-1017.

Asaka Y, Jugloff DG, Zhang L, Eubanks JH, Fitzsimonds RM (2006) Hippocampal synaptic plasticity is impaired in the Mecp2-null mouse model of Rett syndrome. Neurobiol Dis 21:217-227.

Avalos AM, Arthur WT, Schneider P, Quest AF, Burridge K, Leyton L (2004) Aggregation of integrins and RhoA activation are required for Thy-1-induced morphological changes in astrocytes. J Biol Chem 279:39139-39145.

Avalos AM, Labra CV, Quest AF, Leyton L (2002) Signaling triggered by Thy-1 interaction with beta 3 integrin on astrocytes is an essential step towards unraveling neuronal Thy-1 function. Biol Res 35:231-238.

Ballas N, Lioy DT, Grunseich C, Mandel G (2009) Non-cell autonomous influence of MeCP2-deficient glia on neuronal dendritic morphology. Nat Neurosci 12:311-317.

Ballestar E, Wolffe AP (2001) Methyl-CpG-binding proteins. Targeting specific gene repression. Eur J Biochem 268:1-6.

Ballesteros-Yanez I, Benavides-Piccione R, Elston GN, Yuste R, DeFelipe J (2006) Density and morphology of dendritic spines in mouse neocortex. Neuroscience 138:403-409.

Balmer D, Goldstine J, Rao YM, LaSalle JM (2003) Elevated methyl-CpG-binding protein 2 expression is acquired during postnatal human brain development and is correlated with alternative polyadenylation. J Mol Med 81:61-68.

Bao XH, Pan H, Song FY, Wu XR (2004) [Clinical feature of Rett syndrome and MeCP2 genotype/phenotype correlation analysis]. Zhonghua Er Ke Za Zhi 42:252-255.

Barlow JZ, Huntley GW (2000) Developmentally regulated expression of Thy-1 in structures of the mouse sensory-motor system. J Comp Neurol 421:215-233.

Barlow JZ, Kelley KA, Bozdagi O, Huntley GW (2002) Testing the role of the cell-surface molecule Thy-1 in regeneration and plasticity of connectivity in the CNS. Neuroscience 111:837-852.

Bauman ML, Kemper TL, Arin DM (1995a) Microscopic observations of the brain in Rett syndrome. Neuropediatrics 26:105-108.

Bauman ML, Kemper TL, Arin DM (1995b) Pervasive neuroanatomic abnormalities of the brain in three cases of Rett's syndrome. Neurology 45:1581-1586.

Belichenko NP, Belichenko PV, Li HH, Mobley WC, Francke U (2008) Comparative study of brain morphology in Mecp2 mutant mouse models of Rett syndrome. J Comp Neurol 508:184-195.

Belichenko NP, Belichenko PV, Mobley WC (2009) Evidence for both neuronal cell autonomous and nonautonomous effects of methyl-CpG-binding protein 2 in the cerebral cortex of female mice with Mecp2 mutation. Neurobiol Dis 34:71-77.

Belichenko PV, Dahlstrom A (1995) Studies on the 3-dimensional architecture of dendritic spines and varicosities in human cortex by confocal laser scanning microscopy and Lucifer yellow microinjections. J Neurosci Methods 57:55-61.

Belichenko PV, Hagberg B, Dahlstrom A (1997) Morphological study of neocortical areas in Rett syndrome. Acta Neuropathol (Berl) 93:50-61.

Belichenko PV, Oldfors A, Hagberg B, Dahlstrom A (1994) Rett syndrome: 3-D confocal microscopy of cortical pyramidal dendrites and afferents. Neuroreport 5:1509-1513.

Belichenko PV, Wright EE, Belichenko NP, Masliah E, Li HH, Mobley WC, Francke U (2009) Widespread changes in dendritic and axonal morphology in Mecp2-mutant mouse models of Rett syndrome: evidence for disruption of neuronal networks. J Comp Neurol 514:240-258.

Ben-Shachar S, Chahrour M, Thaller C, Shaw CA, Zoghbi HY (2009) Mouse models of MeCP2 disorders share gene expression changes in the cerebellum and hypothalamus. Hum Mol Genet 18:2431-2442.

Benavides-Piccione R, Hamzei-Sichani F, Ballesteros-Yanez I, DeFelipe J, Yuste R (2006) Dendritic size of pyramidal neurons differs among mouse cortical regions. Cereb Cortex 16:990-1001.

Bienvenu T, Carrie A, de Roux N, Vinet MC, Jonveaux P, Couvert P, Villard L, Arzimanoglou A, Beldjord C, Fontes M, Tardieu M, Chelly J (2000) MECP2 mutations account for most cases of typical forms of Rett syndrome. Hum Mol Genet 9:1377-1384.

Bienvenu T, Chelly J (2006) Molecular genetics of Rett syndrome: when DNA methylation goes unrecognized. Nat Rev Genet 7:415-426.

Bolin LM, Rouse RV (1986) Localization of Thy-1 expression during postnatal development of the mouse cerebellar cortex. J Neurocytol 15:29-36.

Bota M, Dong HW, Swanson LW (2003) From gene networks to brain networks. Nat Neurosci 6:795-799.

Brown D, Waneck GL (1992) Glycosyl-phosphatidylinositol-anchored membrane proteins. J Am Soc Nephrol 3:895-906.

Buldyrev SV, Cruz L, Gomez-Isla T, Gomez-Tortosa E, Havlin S, Le R, Stanley HE, Urbanc B, Hyman BT (2000) Description of microcolumnar ensembles in association cortex and their disruption in Alzheimer and Lewy body dementias. Proc Natl Acad Sci U S A 97:5039-5043.

Buschdorf JP, Stratling WH (2004) A WW domain binding region in methyl-CpG-binding protein MeCP2: impact on Rett syndrome. J Mol Med 82:135-143.

Buxhoeveden DP, Casanova MF (2002) The minicolumn hypothesis in neuroscience. Brain 125:935-951.

Carney RM, Wolpert CM, Ravan SA, Shahbazian M, Ashley-Koch A, Cuccaro ML, Vance JM, Pericak-Vance MA (2003) Identification of MeCP2 mutations in a series of females with autistic disorder. Pediatr Neurol 28:205-211.

Caroni P (1997) Overexpression of growth-associated proteins in the neurons of adult transgenic mice. J Neurosci Methods 71:3-9.

Carter JC, Lanham DC, Pham D, Bibat G, Naidu S, Kaufmann WE (2008) Selective cerebral volume reduction in Rett syndrome: a multiple-approach MR imaging study. AJNR Am J Neuroradiol 29:436-441.

Casanova MF, Buxhoeveden D, Switala A, Roy E (2003) Rett syndrome as a minicolumnopathy. Clin Neuropathol 22:163-168.

Casanova MF, Naidu S, Goldberg TE, Moser HW, Khoromi S, Kumar A, Kleinman JE, Weinberger DR (1991) Quantitative magnetic resonance imaging in Rett syndrome. J Neuropsychiatry Clin Neurosci 3:66-72.

Cauller LJ, Clancy B, Connors BW (1998) Backward cortical projections to primary somatosensory cortex in rats extend long horizontal axons in layer I. J Comp Neurol 390:297-310.

Chagnac-Amitai Y, Luhmann HJ, Prince DA (1990) Burst generating and regular spiking layer 5 pyramidal neurons of rat neocortex have different morphological features. J Comp Neurol 296:598-613.

Chahrour M, Jung SY, Shaw C, Zhou X, Wong ST, Qin J, Zoghbi HY (2008) MeCP2, a key contributor to neurological disease, activates and represses transcription. Science 320:1224-1229.

Chandler SP, Guschin D, Landsberger N, Wolffe AP (1999) The methyl-CpG binding transcriptional repressor MeCP2 stably associates with nucleosomal DNA. Biochemistry 38:7008-7018.

Chao HT, Zoghbi HY (2009) The yin and yang of MeCP2 phosphorylation. Proc Natl Acad Sci U S A 106:4577-4578.

Chen BE, Lendvai B, Nimchinsky EA, Burbach B, Fox K, Svoboda K (2000) Imaging high-resolution structure of GFP-expressing neurons in neocortex in vivo. Learn Mem 7:433-441.

Chen RZ, Akbarian S, Tudor M, Jaenisch R (2001) Deficiency of methyl-CpG binding protein-2 in CNS neurons results in a Rett-like phenotype in mice. Nat Genet 27:327-331.

Chen WG, Chang Q, Lin Y, Meissner A, West AE, Griffith EC, Jaenisch R, Greenberg ME (2003) Derepression of BDNF transcription involves calcium-dependent phosphorylation of MeCP2. Science 302:885-889.

Chow JC, Yen Z, Ziesche SM, Brown CJ (2005) Silencing of the mammalian X chromosome. Annu Rev Genomics Hum Genet 6:69-92.

Christodoulou J, Grimm A, Maher T, Bennetts B (2003) RettBASE: The IRSA MECP2 variation database-a new mutation database in evolution. Hum Mutat 21:466-472.

Christodoulou J, Weaving LS (2003) MECP2 and beyond: phenotype-genotype correlations in Rett syndrome. J Child Neurol 18:669-674.

Connors BW, Gutnick MJ, Prince DA (1982) Electrophysiological properties of neocortical neurons in vitro. J Neurophysiol 48:1302-1320.

Couvert P, Bienvenu T, Aquaviva C, Poirier K, Moraine C, Gendrot C, Verloes A, Andres C, Le Fevre AC, Souville I, Steffann J, des Portes V, Ropers HH, Yntema HG, Fryns JP, Briault S, Chelly J, Cherif B (2001) MECP2 is highly mutated in X-linked mental retardation. Hum Mol Genet 10:941-946.

Coy JF, Sedlacek Z, Bachner D, Delius H, Poustka A (1999) A complex pattern of evolutionary conservation and alternative polyadenylation within the long 3"-untranslated region of the methyl-CpG-binding protein 2 gene (MeCP2) suggests a regulatory role in gene expression. Hum Mol Genet 8:1253-1262.

Crawley MJ (2007) The R book . Chichester, England ; Hoboken, N.J. : Wiley.

Cukier HN, Perez AM, Collins AL, Zhou Z, Zoghbi HY, Botas J (2008) Genetic modifiers of MeCP2 function in Drosophila. PLoS Genet 4:e1000179.

D'Esposito M, Quaderi NA, Ciccodicola A, Bruni P, Esposito T, D'Urso M, Brown SD (1996) Isolation, physical mapping, and northern analysis of the X-linked human gene encoding methyl CpG-binding protein, MECP2. Mamm Genome 7:533-535.

Dani VS, Chang Q, Maffei A, Turrigiano GG, Jaenisch R, Nelson SB (2005) Reduced cortical activity due to a shift in the balance between excitation and inhibition in a mouse model of Rett syndrome. Proc Natl Acad Sci U S A 102:12560-12565.

Dani VS, Nelson SB (2009) Intact long-term potentiation but reduced connectivity between neocortical layer 5 pyramidal neurons in a mouse model of Rett syndrome. J Neurosci 29:11263-11270.

Dobie K, Mehtali M, McClenaghan M, Lathe R (1997) Variegated gene expression in mice. Trends Genet 13:127-130.

Dobie KW, Lee M, Fantes JA, Graham E, Clark AJ, Springbett A, Lathe R, McClenaghan M (1996) Variegated transgene expression in mouse mammary gland is determined by the transgene integration locus. Proc Natl Acad Sci U S A 93:6659-6664.

Douglas RJ, Martin KA (2004) Neuronal circuits of the neocortex. Annu Rev Neurosci 27:419-451.

Douglas RJ, Martin KA (2007) Mapping the matrix: the ways of neocortex. Neuron 56:226-238.

Eisthen HL, Delay RJ, Wirsig-Wiechmann CR, Dionne VE (2000) Neuromodulatory effects of gonadotropin releasing hormone on olfactory receptor neurons. J Neurosci 20:3947-3955.

Elston GN, Rosa MG (2000) Pyramidal cells, patches, and cortical columns: a comparative study of infragranular neurons in TEO, TE, and the superior temporal polysensory area of the macaque monkey. J Neurosci 20:RC117.

Elston GN, Rosa MG, Calford MB (1996) Comparison of dendritic fields of layer III pyramidal neurons in striate and extrastriate visual areas of the marmoset: a Lucifer yellow intracellular injection. Cereb Cortex 6:807-813.

Eppig, JT (2006) The Mouse in Biomedical Research (Fox, J, Barthold, S, Davisson, M, Newcomer, C, Quimby, F, Smith, A, eds). Academic Press.

Fatemi M, Pao MM, Jeong S, Gal-Yam EN, Egger G, Weisenberger DJ, Jones PA (2005) Footprinting of mammalian promoters: use of a CpG DNA methyltransferase revealing nucleosome positions at a single molecule level. Nucleic Acids Res 33:e176.

Favorov OV, Kelly DG (1994) Minicolumnar organization within somatosensory cortical segregates: II. Emergent functional properties. Cereb Cortex 4:428-442.

Feng G, Mellor RH, Bernstein M, Keller-Peck C, Nguyen QT, Wallace M, Nerbonne JM, Lichtman JW, Sanes JR (2000) Imaging neuronal subsets in transgenic mice expressing multiple spectral variants of GFP. Neuron 28:41-51.

Festenstein R, Tolaini M, Corbella P, Mamalaki C, Parrington J, Fox M, Miliou A, Jones M, Kioussis D (1996) Locus control region function and heterochromatin-induced position effect variegation. Science 271:1123-1125.

Flaherty, L (1981) The Mouse in Biomedical Research (Foster HL, Small JD, Fox JG, eds). New York: Academic Press.

Fox KP (2008) Barrel cortex . Cambridge ; New York : Cambridge University Press.

Fyfe S, Cream A, de Klerk N, Christodoulou J, Leonard H (2003) InterRett and RettBASE: International Rett Syndrome Association databases for Rett syndrome. J Child Neurol 18:709-713.

Gardiner-Garden M, Frommer M (1987) CpG islands in vertebrate genomes. J Mol Biol 196:261-282.

Georgopoulos AP, Merchant H, Naselaris T, Amirikian B (2007) Mapping of the preferred direction in the motor cortex. Proc Natl Acad Sci U S A 104:11068-11072.

Graubert TA, Hug BA, Wesselschmidt R, Hsieh CL, Ryan TM, Townes TM, Ley TJ (1998) Stochastic, stage-specific mechanisms account for the variegation of a human globin transgene. Nucleic Acids Res 26:2849-2858.

Guy J, Gan J, Selfridge J, Cobb S, Bird A (2007) Reversal of neurological defects in a mouse model of Rett syndrome. Science 315:1143-1147.

Guy J, Hendrich B, Holmes M, Martin JE, Bird A (2001) A mouse Mecp2-null mutation causes neurological symptoms that mimic Rett syndrome. Nat Genet 27:322-326.

Hagberg B (1995) Clinical delineation of Rett syndrome variants. Neuropediatrics 26:62.

Hagberg B (2002) Clinical manifestations and stages of Rett syndrome. Ment Retard Dev Disabil Res Rev 8:61-65.

Hagberg B, Aicardi J, Dias K, Ramos O (1983) A progressive syndrome of autism, dementia, ataxia, and loss of purposeful hand use in girls: Rett's syndrome: report of 35 cases. Ann Neurol 14:471-479.

Hagberg B, Goutières F, Hanefeld F, Rett A, Wilson J (1985) Rett syndrome: criteria for inclusion and exclusion. Brain Dev 7:372-373.

Hattox AM, Nelson SB (2007) Layer V neurons in mouse cortex projecting to different targets have distinct physiological properties. J Neurophysiol 98:3330-3340.

Hendrich B, Bird A (1998) Identification and characterization of a family of mammalian methyl-CpG binding proteins. Mol Cell Biol 18:6538-6547.

Hitchins MP, Rickard S, Dhalla F, Fairbrother UL, de Vries BB, Winter R, Pembrey ME, Malcolm S (2004) Investigation of UBE3A and MECP2 in Angelman syndrome (AS) and patients with features of AS. Am J Med Genet A 125:167-172.

Hoffbuhr K, Devaney JM, LaFleur B, Sirianni N, Scacheri C, Giron J, Schuette J, Innis J, Marino M, Philippart M, Narayanan V, Umansky R, Kronn D, Hoffman EP, Naidu S

(2001) MeCP2 mutations in children with and without the phenotype of Rett syndrome. Neurology 56:1486-1495.

Hoffbuhr KC, Moses LM, Jerdonek MA, Naidu S, Hoffman EP (2002) Associations between MeCP2 mutations, X-chromosome inactivation, and phenotype. Ment Retard Dev Disabil Res Rev 8:99-105.

Huppke P, Köhler K, Brockmann K, Stettner GM, Gärtner J (2007) Treatment of epilepsy in Rett syndrome. Eur J Paediatr Neurol 11:10-16.

Huppke P, Maier EM, Warnke A, Brendel C, Laccone F, Gartner J (2006) Very mild cases of Rett syndrome with skewed X inactivation. J Med Genet.

Hurlbert SH (1984) Pseudoreplication and the design of ecological field experiments. Ecological monographs 54:187-211.

Jeng CJ, McCarroll SA, Martin TF, Floor E, Adams J, Krantz D, Butz S, Edwards R, Schweitzer ES (1998) Thy-1 is a component common to multiple populations of synaptic vesicles. J Cell Biol 140:685-698.

Jones EG (2000) Microcolumns in the cerebral cortex. Proc Natl Acad Sci U S A 97:5019-5021.

Jones PL, Veenstra GJ, Wade PA, Vermaak D, Kass SU, Landsberger N, Strouboulis J, Wolffe AP (1998) Methylated DNA and MeCP2 recruit histone deacetylase to repress transcription. Nat Genet 19:187-191.

Jordan C, Li HH, Kwan HC, Francke U (2007) Cerebellar gene expression profiles of mouse models for Rett syndrome reveal novel MeCP2 targets. BMC Med Genet 8:36.

Jorgensen HF, Bird A (2002) MeCP2 and other methyl-CpG binding proteins. Ment Retard Dev Disabil Res Rev 8:87-93.

Jugloff DG, Logan R, Eubanks JH (2006) Breeding and maintenance of an Mecp2-deficient mouse model of Rett syndrome. J Neurosci Methods 154:89-95.

Kaludov NK, Wolffe AP (2000) MeCP2 driven transcriptional repression in vitro: selectivity for methylated DNA, action at a distance and contacts with the basal transcription machinery. Nucleic Acids Res 28:1921-1928.

Kampa BM, Stuart GJ (2006) Calcium spikes in basal dendrites of layer 5 pyramidal neurons during action potential bursts. J Neurosci 26:7424-7432.

Kishi N, Macklis JD (2004) MECP2 is progressively expressed in post-migratory neurons and is involved in neuronal maturation rather than cell fate decisions. Mol Cell Neurosci 27:306-321.

Klose RJ, Bird AP (2004) MeCP2 behaves as an elongated monomer that does not stably associate with the Sin3a chromatin remodeling complex. J Biol Chem 279:46490-46496.

Kokura K, Kaul SC, Wadhwa R, Nomura T, Khan MM, Shinagawa T, Yasukawa T, Colmenares C, Ishii S (2001) The Ski protein family is required for MeCP2-mediated transcriptional repression. J Biol Chem 276:34115-34121.

Kriaucionis S, Bird A (2004) The major form of MeCP2 has a novel N-terminus generated by alternative splicing. Nucleic Acids Res 32:1818-1823.

Kuhn B, Denk W, Bruno RM (2008) In vivo two-photon voltage-sensitive dye imaging reveals top-down control of cortical layers 1 and 2 during wakefulness. Proc Natl Acad Sci U S A 105:7588-7593.

Larkman AU (1991) Dendritic morphology of pyramidal neurones of the visual cortex of the rat: III. Spine distributions. J Comp Neurol 306:332-343.

Larkum ME, Nevian T, Sandler M, Polsky A, Schiller J (2009) Synaptic integration in tuft dendrites of layer 5 pyramidal neurons: a new unifying principle. Science 325:756-760.

Larkum ME, Senn W, Lüscher HR (2004) Top-down dendritic input increases the gain of layer 5 pyramidal neurons. Cereb Cortex 14:1059-1070.

LaSalle JM, Goldstine J, Balmer D, Greco CM (2001) Quantitative localization of heterogeneous methyl-CpG-binding protein 2 (MeCP2) expression phenotypes in normal and Rett syndrome brain by laser scanning cytometry. Hum Mol Genet 10:1729-1740.

LaSalle JM, Hogart A, Thatcher KN (2005) Rett syndrome: a Rosetta stone for understanding the molecular pathogenesis of autism. Int Rev Neurobiol 71:131-165.

LeBlanc DC (2004) Statistics : concepts and applications for science . Boston : Jones and Bartlett.

Lev DL, White EL (1997) Organization of pyramidal cell apical dendrites and composition of dendritic clusters in the mouse: emphasis on primary motor cortex. Eur J Neurosci 9:280-290.

Lewis JD, Meehan RR, Henzel WJ, Maurer-Fogy I, Jeppesen P, Klein F, Bird A (1992) Purification, sequence, and cellular localization of a novel chromosomal protein that binds to methylated DNA. Cell 69:905-914.

Lipp HP, Wolfer DP (2003) Genetic background problems in the analysis of cognitive

and neuronal changes in genetically modified mice. Clinical Neuroscience Research 3: 223–231.

Luikenhuis S, Giacometti E, Beard CF, Jaenisch R (2004) Expression of MeCP2 in postmitotic neurons rescues Rett syndrome in mice. Proc Natl Acad Sci U S A 101:6033-6038.

Maezawa I, Swanberg S, Harvey D, LaSalle JM, Jin LW (2009) Rett syndrome astrocytes are abnormal and spread MeCP2 deficiency through gap junctions. J Neurosci 29:5051-5061.

Mahanthappa NK, Patterson PH (1992a) Thy-1 involvement in neurite outgrowth: perturbation by antibodies, phospholipase C, and mutation. Dev Biol 150:47-59.

Mahanthappa NK, Patterson PH (1992b) Thy-1 multimerization is correlated with neurite outgrowth. Dev Biol 150:60-71.

Mainen ZF, Sejnowski TJ (1996) Influence of dendritic structure on firing pattern in model neocortical neurons. Nature 382:363-366.

Markram H, Lübke J, Frotscher M, Roth A, Sakmann B (1997) Physiology and anatomy of synaptic connections between thick tufted pyramidal neurones in the developing rat neocortex. J Physiol 500 (Pt 2):409-440.

Matarazzo V, Ronnett GV (2004) Temporal and regional differences in the olfactory proteome as a consequence of MeCP2 deficiency. Proc Natl Acad Sci U S A 101:7763-7768.

Miltenberger-Miltenyi G, Laccone F (2003) Mutations and polymorphisms in the human methyl CpG-binding protein MECP2. Hum Mutat 22:107-115.

Miyake K, Nagai K (2007) Phosphorylation of methyl-CpG binding protein 2 (MeCP2) regulates the intracellular localization during neuronal cell differentiation. Neurochem Int 50:264-270.

Mnatzakanian GN, Lohi H, Munteanu I, Alfred SE, Yamada T, MacLeod PJ, Jones JR, Scherer SW, Schanen NC, Friez MJ, Vincent JB, Minassian BA (2004) A previously unidentified MECP2 open reading frame defines a new protein isoform relevant to Rett syndrome. Nat Genet 36:339-341.

Molnár Z, Cheung AF (2006) Towards the classification of subpopulations of layer V pyramidal projection neurons. Neurosci Res 55:105-115.

Moretti P, Levenson JM, Battaglia F, Atkinson R, Teague R, Antalffy B, Armstrong D, Arancio O, Sweatt JD, Zoghbi HY (2006) Learning and memory and synaptic plasticity are impaired in a mouse model of Rett syndrome. J Neurosci 26:319-327.

Morris R (1985) Thy-1 in developing nervous tissue. Dev Neurosci 7:133-160.

Morris RJ, Tiveron MC, Xue GP (1992) The relation of the expression and function of the neuronal glycoprotein Thy-1 to axonal growth. Biochem Soc Trans 20:401-405.

Mountcastle VB (1997) The columnar organization of the neocortex. Brain 120 (Pt 4):701-722.

Mountcastle VB (1998) Perceptual neuroscience: The cerebral cortex. Harvard University Press.

Mullaney BC, Johnston MV, Blue ME (2004) Developmental expression of methyl-CpG binding protein 2 is dynamically regulated in the rodent brain. Neuroscience 123:939-949.

Murakami JW, Courchesne E, Haas RH, Press GA, Yeung-Courchesne R (1992) Cerebellar and cerebral abnormalities in Rett syndrome: a quantitative MR analysis. AJR Am J Roentgenol 159:177-183.

Naidu S, Kaufmann WE, Abrams MT, Pearlson GD, Lanham DC, Fredericksen KA, Barker PB, Horska A, Golay X, Mori S, Wong DF, Yablonski M, Moser HW, Johnston MV (2001) Neuroimaging studies in Rett syndrome. Brain Dev 23 Suppl 1:S62-S71.

Nan X, Bird A (2001) The biological functions of the methyl-CpG-binding protein MeCP2 and its implication in Rett syndrome. Brain Dev 23 Suppl 1:S32-S37.

Nan X, Campoy FJ, Bird A (1997) MeCP2 is a transcriptional repressor with abundant binding sites in genomic chromatin. Cell 88:471-481.

Nan X, Meehan RR, Bird A (1993) Dissection of the methyl-CpG binding domain from the chromosomal protein MeCP2. Nucleic Acids Res 21:4886-4892.

Nan X, Ng HH, Johnson CA, Laherty CD, Turner BM, Eisenman RN, Bird A (1998) Transcriptional repression by the methyl-CpG-binding protein MeCP2 involves a histone deacetylase complex. Nature 393:386-389.

Nan X, Tate P, Li E, Bird A (1996) DNA methylation specifies chromosomal localization of MeCP2. Mol Cell Biol 16:414-421.

Neul JL, Fang P, Barrish J, Lane J, Caeg EB, Smith EO, Zoghbi H, Percy A, Glaze DG (2008) Specific mutations in methyl-CpG-binding protein 2 confer different severity in Rett syndrome. Neurology 70:1313-1321.

Nolte C, Matyash M, Pivneva T, Schipke CG, Ohlemeyer C, Hanisch UK, Kirchhoff F, Kettenmann H (2001) GFAP promoter-controlled EGFP-expressing transgenic mice: a tool to visualize astrocytes and astrogliosis in living brain tissue. Glia 33:72-86.

O'Donovan KJ, Darnell RB (2001) Neuronal signaling through alternative splicing: some exons CaRRE. Sci STKE 2001:PE2.

Opsahl ML, McClenaghan M, Springbett A, Reid S, Lathe R, Colman A, Whitelaw CB (2002) Multiple effects of genetic background on variegated transgene expression in mice. Genetics 160:1107-1112.

Paxinos G1, Franklin KBJ, Franklin KBJMBISC (2001) The mouse brain in stereotaxic coordinates . San Diego : Academic Press.

Petreanu L, Mao T, Sternson SM, Svoboda K (2009) The subcellular organization of neocortical excitatory connections. Nature 457:1142-1145.

Raff MC, Fields KL, Hakomori SI, Mirsky R, Pruss RM, Winter J (1979) Cell-type-specific markers for distinguishing and studying neurons and the major classes of glial cells in culture. Brain Res 174:283-308.

Rakic P (2008) Confusing cortical columns. Proc Natl Acad Sci U S A 105:12099-12100.

Reichwald K, Thiesen J, Wiehe T, Weitzel J, Poustka WA, Rosenthal A, Platzer M, Stratling WH, Kioschis P (2000) Comparative sequence analysis of the MECP2-locus in human and mouse reveals new transcribed regions. Mamm Genome 11:182-190.

Renieri A, Meloni I, Longo I, Ariani F, Mari F, Pescucci C, Cambi F (2003) Rett syndrome: the complex nature of a monogenic disease. J Mol Med 81:346-354.

Rett A (1966) [On a unusual brain atrophy syndrome in hyperammonemia in childhood]. Wien Med Wochenschr 116:723-726.

Robins E, Smith DE, EYDT KM (1956) The quantitative histochemistry of the cerebral cortex. I. Architectonic distribution of ten chemical constituents in the motor and visual cortices. J Neurochem 1:54-67.

Rubio-Garrido P, Pérez-de-Manzo F, Porrero C, Galazo MJ, Clascá F (2009) Thalamic Input to Distal Apical Dendrites in Neocortical Layer 1 Is Massive and Highly Convergent. Cereb Cortex.

Samaco RC, Nagarajan RP, Braunschweig D, LaSalle JM (2004) Multiple pathways regulate MeCP2 expression in normal brain development and exhibit defects in autism-spectrum disorders. Hum Mol Genet 13:629-639.

Saywell V, Viola A, Confort-Gouny S, Le Fur Y, Villard L, Cozzone PJ (2006) Brain magnetic resonance study of Mecp2 deletion effects on anatomy and metabolism. Biochem Biophys Res Commun 340:776-783.

Schaefer AT, Larkum ME, Sakmann B, Roth A (2003) Coincidence detection in pyramidal neurons is tuned by their dendritic branching pattern. J Neurophysiol 89:3143-3154.

Schanen C, Houwink EJ, Dorrani N, Lane J, Everett R, Feng A, Cantor RM, Percy A (2004) Phenotypic manifestations of MECP2 mutations in classical and atypical Rett syndrome. Am J Med Genet A 126:129-140.

Schubert D, Kötter R, Staiger JF (2007) Mapping functional connectivity in barrel-related columns reveals layer- and cell type-specific microcircuits. Brain Struct Funct 212:107-119.

Schubert D, Staiger JF, Cho N, Kötter R, Zilles K, Luhmann HJ (2001) Layer-specific intracolumnar and transcolumnar functional connectivity of layer V pyramidal cells in rat barrel cortex. J Neurosci 21:3580-3592.

Shahbazian M, Young J, Yuva-Paylor L, Spencer C, Antalffy B, Noebels J, Armstrong D, Paylor R, Zoghbi H (2002a) Mice with truncated MeCP2 recapitulate many Rett syndrome features and display hyperacetylation of histone H3. Neuron 35:243-254.

Shahbazian MD, Antalffy B, Armstrong DL, Zoghbi HY (2002b) Insight into Rett syndrome: MeCP2 levels display tissue- and cell-specific differences and correlate with neuronal maturation. Hum Mol Genet 11:115-124.

Shahbazian MD, Zoghbi HY (2001) Molecular genetics of Rett syndrome and clinical spectrum of MECP2 mutations. Curr Opin Neurol 14:171-176.

Shaner NC, Steinbach PA, Tsien RY (2005) A guide to choosing fluorescent proteins. Nat Methods 2:905-909.

Shepherd GM, Stepanyants A, Bureau I, Chklovskii D, Svoboda K (2005) Geometric and functional organization of cortical circuits. Nat Neurosci 8:782-790.

Shibayama A, Cook EHJ, Feng J, Glanzmann C, Yan J, Craddock N, Jones IR, Goldman D, Heston LL, Sommer SS (2004) MECP2 structural and 3'-UTR variants in schizophrenia, autism and other psychiatric diseases: a possible association with autism. Am J Med Genet B Neuropsychiatr Genet 128B:50-53.

Shipp S (2005) The importance of being agranular: a comparative account of visual and motor cortex. Philos Trans R Soc Lond B Biol Sci 360:797-814.

Sholl DA (1953) Dendritic organization in the neurons of the visual and motor cortices of the cat. J Anat 87:387-406.

Silva AJ, Simpson EM, Takahashi JS (1997) Mutant Mice and Neuroscience: Recommendations Concerning Genetic Background. Neuron 19:755-759.

Silver LM (1995) Mouse genetics : concepts and applications . New York : Oxford University Press.

Sirianni N, Naidu S, Pereira J, Pillotto RF, Hoffman EP (1998) Rett syndrome: confirmation of X-linked dominant inheritance, and localization of the gene to Xq28. Am J Hum Genet 63:1552-1558.

Sneller MC, Gunter KC (1987) DNA methylation alters chromatin structure and regulates Thy-1 expression in EL-4 T cells. J Immunol 138:3505-3512.

Spratling MW (2002) Cortical region interactions and the functional role of apical dendrites. Behav Cogn Neurosci Rev 1:219-228.

Stohl W, Gonatas NK (1977) Distribution of the thy-1 antigen in cellular and subcellular fractions of adult mouse brain. J Immunol 119:422-427.

Stuart G, Schiller J, Sakmann B (1997a) Action potential initiation and propagation in rat neocortical pyramidal neurons. J Physiol 505 (Pt 3):617-632.

Stuart G, Spruston N, Sakmann B, Häusser M (1997b) Action potential initiation and backpropagation in neurons of the mammalian CNS. Trends Neurosci 20:125-131.

Subramaniam B, Naidu S, Reiss AL (1997) Neuroanatomy in Rett syndrome: cerebral cortex and posterior fossa. Neurology 48:399-407.

Sugino K, Hempel CM, Miller MN, Hattox AM, Shapiro P, Wu C, Huang ZJ, Nelson SB (2006) Molecular taxonomy of major neuronal classes in the adult mouse forebrain. Nat Neurosci 9:99-107.

Swanson LW (2003) Brain architecture : understanding the basic plan . Oxford ; New York : Oxford University Press.

Szyf M, Tanigawa G, McCarthy PLJ (1990) A DNA signal from the Thy-1 gene defines de novo methylation patterns in embryonic stem cells. Mol Cell Biol 10:4396-4400.

Taneja P, Ogier M, Brooks-Harris G, Schmid DA, Katz DM, Nelson SB (2009) Pathophysiology of locus ceruleus neurons in a mouse model of Rett syndrome. J Neurosci 29:12187-12195.

Tao J, Hu K, Chang Q, Wu H, Sherman NE, Martinowich K, Klose RJ, Schanen C, Jaenisch R, Wang W, Sun YE (2009) Phosphorylation of MeCP2 at Serine 80 regulates

its chromatin association and neurological function. Proc Natl Acad Sci U S A 106:4882-4887.

Thambirajah AA, Eubanks JH, Ausió J (2009) MeCP2 post-translational regulation through PEST domains: two novel hypotheses: potential relevance and implications for Rett syndrome. Bioessays 31:561-569.

Traynor J, Agarwal P, Lazzeroni L, Francke U (2002) Gene expression patterns vary in clonal cell cultures from Rett syndrome females with eight different MECP2 mutations. BMC Med Genet 3:12.

Trevathan E, Naidu S (1988) The clinical recognition and differential diagnosis of Rett syndrome. J Child Neurol 3 Suppl:S6-16.

Tsien RY (1998) The green fluorescent protein. Annu Rev Biochem 67:509-544.

Tsiola A, Hamzei-Sichani F, Peterlin Z, Yuste R (2003) Quantitative morphologic classification of layer 5 neurons from mouse primary visual cortex. J Comp Neurol 461:415-428.

Tudor M, Akbarian S, Chen RZ, Jaenisch R (2002) Transcriptional profiling of a mouse model for Rett syndrome reveals subtle transcriptional changes in the brain. Proc Natl Acad Sci U S A 99:15536-15541.

Urdinguio RG, Lopez-Serra L, Lopez-Nieva P, Alaminos M, Diaz-Uriarte R, Fernandez AF, Esteller M (2008) Mecp2-null mice provide new neuronal targets for Rett syndrome. PLoS One 3:e3669.

Vetter P, Roth A, Häusser M (2001) Propagation of action potentials in dendrites depends on dendritic morphology. J Neurophysiol 85:926-937.

Viemari JC, Roux JC, Tryba AK, Saywell V, Burnet H, Peña F, Zanella S, Bévengut M, Barthelemy-Requin M, Herzing LB, Moncla A, Mancini J, Ramirez JM, Villard L, Hilaire G (2005) Mecp2 deficiency disrupts norepinephrine and respiratory systems in mice. J Neurosci 25:11521-11530.

Voelker CC, Garin N, Taylor JS, Gähwiler BH, Hornung JP, Molnár Z (2004) Selective neurofilament (SMI-32, FNP-7 and N200) expression in subpopulations of layer V pyramidal neurons in vivo and in vitro. Cereb Cortex 14:1276-1286.

Wachter RM, Elsliger MA, Kallio K, Hanson GT, Remington SJ (1998) Structural basis of spectral shifts in the yellow-emission variants of green fluorescent protein. Structure 6:1267-1277.

Wakefield RI, Smith BO, Nan X, Free A, Soteriou A, Uhrin D, Bird AP, Barlow PN (1999) The solution structure of the domain from MeCP2 that binds to methylated DNA. J Mol Biol 291:1055-1065.

Walters MC, Fiering S, Eidemiller J, Magis W, Groudine M, Martin DI (1995) Enhancers increase the probability but not the level of gene expression. Proc Natl Acad Sci U S A 92:7125-7129.

Watson P, Black G, Ramsden S, Barrow M, Super M, Kerr B, Clayton-Smith J (2001) Angelman syndrome phenotype associated with mutations in MECP2, a gene encoding a methyl CpG binding protein. J Med Genet 38:224-228.

Weaving LS, Williamson SL, Bennetts B, Davis M, Ellaway CJ, Leonard H, Thong MK, Delatycki M, Thompson EM, Laing N, Christodoulou J (2003) Effects of MECP2 mutation type, location and X-inactivation in modulating Rett syndrome phenotype. Am J Med Genet A 118:103-114.

Wolfer DP, Crusio WE, Lipp HP (2002) Knockout mice: simple solutions to the problems of genetic background and flanking genes. Trends Neurosci 25:336-340.

Wu L, Sluiter AA, Guo HF, Balesar RA, Swaab DF, Zhou JN, Verwer RW (2008) Neural stem cells improve neuronal survival in cultured postmortem brain tissue from aged and Alzheimer patients. J Cell Mol Med 12:1611-1621.

Xue GP, Calvert RA, Morris RJ (1990) Expression of the neuronal surface glycoprotein Thy-1 is under post-transcriptional control, and is spatially regulated, in the developing olfactory system. Development 109:851-864.

Xue GP, Morris R (1992) Expression of the neuronal surface glycoprotein Thy-1 does not follow appearance of its mRNA in developing mouse Purkinje cells. J Neurochem 58:430-440.

Xue GP, Rivero BP, Morris RJ (1991) The surface glycoprotein Thy-1 is excluded from growing axons during development: a study of the expression of Thy-1 during axogenesis in hippocampus and hindbrain. Development 112:161-176.

Young JI, Hong EP, Castle JC, Crespo-Barreto J, Bowman AB, Rose MF, Kang D, Richman R, Johnson JM, Berget S, Zoghbi HY (2005) Regulation of RNA splicing by the methylation-dependent transcriptional repressor methyl-CpG binding protein 2. Proc Natl Acad Sci U S A 102:17551-17558.

Young JI, Zoghbi HY (2004) X-chromosome inactivation patterns are unbalanced and affect the phenotypic outcome in a mouse model of rett syndrome. Am J Hum Genet 74:511-520.

Yu J, Anderson CT, Kiritani T, Sheets PL, Wokosin DL, Wood L, Shepherd GM (2008) Local-Circuit Phenotypes of Layer 5 Neurons in Motor-Frontal Cortex of YFP-H Mice. Front Neural Circuits 2:6.

Zappella M, Meloni I, Longo I, Canitano R, Hayek G, Rosaia L, Mari F, Renieri A (2003) Study of MECP2 gene in Rett syndrome variants and autistic girls. Am J Med Genet B Neuropsychiatr Genet 119B:102-107.

Zeev BB, Bebbington A, Ho G, Leonard H, de Klerk N, Gak E, Vecsler M, Vecksler M, Christodoulou J (2009) The common BDNF polymorphism may be a modifier of disease severity in Rett syndrome. Neurology 72:1242-1247.

Zhou Z, Hong EJ, Cohen S, Zhao WN, Ho HY, Schmidt L, Chen WG, Lin Y, Savner E, Griffith EC, Hu L, Steen JA, Weitz CJ, Greenberg ME (2006) Brain-specific phosphorylation of MeCP2 regulates activity-dependent Bdnf transcription, dendritic growth, and spine maturation. Neuron 52:255-269.

Zoghbi HY, Percy AK, Schultz RJ, Fill C (1990) Patterns of X chromosome inactivation in the Rett syndrome. Brain Dev 12:131-135.

Appendix I:
Replication and Pseudoreplication in Neuronal Analysis

Statistical analysis assumes that, in any given experiment, the measurements under consideration are independent observations drawn from a representative sample of the population of interest. Pseudoreplication may be defined as the error made by considering multiple non-independent measurements on the same individual in the same manner as multiple independent measures taken from different individuals (Hurlbert, 1984; LeBlanc, 2004). In studies of neuronal properties at the single-cell level, it is a common practice in neuroscience to take the individual neuron as the unit of replication, and pool measurements obtained from different animals. This is pseudoreplication in a strict sense: all measurements from neurons within a given brain are not independent, because they exist within the unique physiological and genetic environment particular to that animal.

In studies using congenic animals raised in controlled conditions, however, it can be plausibly argued that homogeneous genetic backgrounds and rearing environments minimize inter-animal variability to the extent that pooling neurons would not yield statistically invalid results. Indeed, this approach appears necessary if some purchase is to be made on the task of developing a biologically accurate classificatory system that describes the full complement of neuronal subtypes in the nervous system. The transcriptional, morphological, and physiological properties of neurons are so diverse, complex, and ordered that it is likely that any objective, quantitatively based taxonomy of neuronal subtypes can only be established by analyzing them as independent replicates.

In pragmatic considerations, however, this can present a considerable set of obstacles. A transgenic breeding line may be considered congenic after 10 generations of backcrossing to the background strain, at which point less than 1% of the residual unlinked donor genome is likely to remain (Flaherty, 1981; Silver, 1995). Even in optimal circumstances this is a substantial investment in time, effort, and expense. In cases like that seen with *Mecp2* mutant mice, which develop very poor breeding characteristics after only a couple generations of inbreeding, it may be impractical or even impossible. Some studies avoid

pseudoreplication by sampling very small numbers of neurons per animal (e.g. (Eisthen *et al.*, 2000)), but this approach can also be prohibitively costly in time and resources. A more conservative approach to avoid pseudoreplication takes an average measure of subsamples per animal (e.g. Wu *et al.* (2008)), which is the method used in the present study. As discussed in Chapter 2, however, this approach may mask significant and biologically salient heterogeneities if the cell type under study is not a unitary class. If the experimental treatment under consideration only affects one unidentified subtype that is subsumed into a larger group, then significant differences could be missed if the experiment lacks sufficient statistical power. For a given parameter, a 250% increase that affects only 10% of a population is reduced to a 15% increase when considered across that population as a whole, and this difference will only be detected by using very large sample sizes. This phenomenon has been clearly demonstrated in the progress of RTT gene expression studies using either whole-brain homogenates or more precisely fractionated brain regions (Traynor *et al.*, 2002; Tudor *et al.*, 2002; Matarazzo and Ronnett, 2004; Jordan *et al.*, 2007; Chahrour *et al.*, 2008; Urdinguio *et al.*, 2008; Ben-Shachar *et al.*, 2009), and this trend appears to continue to the level of neuronal subtypes within isolated brain regions.[9]

MeCP2 mutant RTT mouse models may represent a more extreme case of this phenomenon, in which a heterogeneous genetic background (among other factors) may modify the phenotypic effects caused by the mutation and lead to contradictory findings in the literature. Nevertheless, studies using transgenic or knockout mice in which the treatment has a substantial negative impact on breeding characteristics may inevitably require mixed genetic backgrounds. In such circumstances a high degree of physiological similarity between animals cannot be assumed, and pseudoreplication becomes a relevant concern. If there are large inter-animal differences within each genotype that contribute significantly to the total variance, then it is not statistically valid to pool the neurons across animals, and analyses should be conducted on measures of the "average neuron" per animal, with individual animals as the unit of replication. Once a sufficiently

[9]Based on unpublished data presented at the 2007 International Rett Syndrome Foundation Conference by Sasha Nelson (Brandeis University), which extend the data published by Sugino *et al.* (2006) to MeCP2 mutant mice.

restricted neuronal subtype can be identified and isolated by unbiased techniques, the experimental design must determine not only how many animals are needed for adequate statistical power, but also how many neurons per animal are required to give a reliable estimate of the mean for that animal. Two examples of how to approach this issue are presented below, based on a post-hoc analysis of data obtained in the present study. Sample program code written in the statistical software R is presented in Appendices II and III as suggested templates for use in planning experimental designs.

Figure 16 shows a plot of the 95% confidence intervals (C.I.) for different neuron sample sizes based on a bootstrap resampling of the pooled total basal dendritic length data from MeCP2 mutant mice.

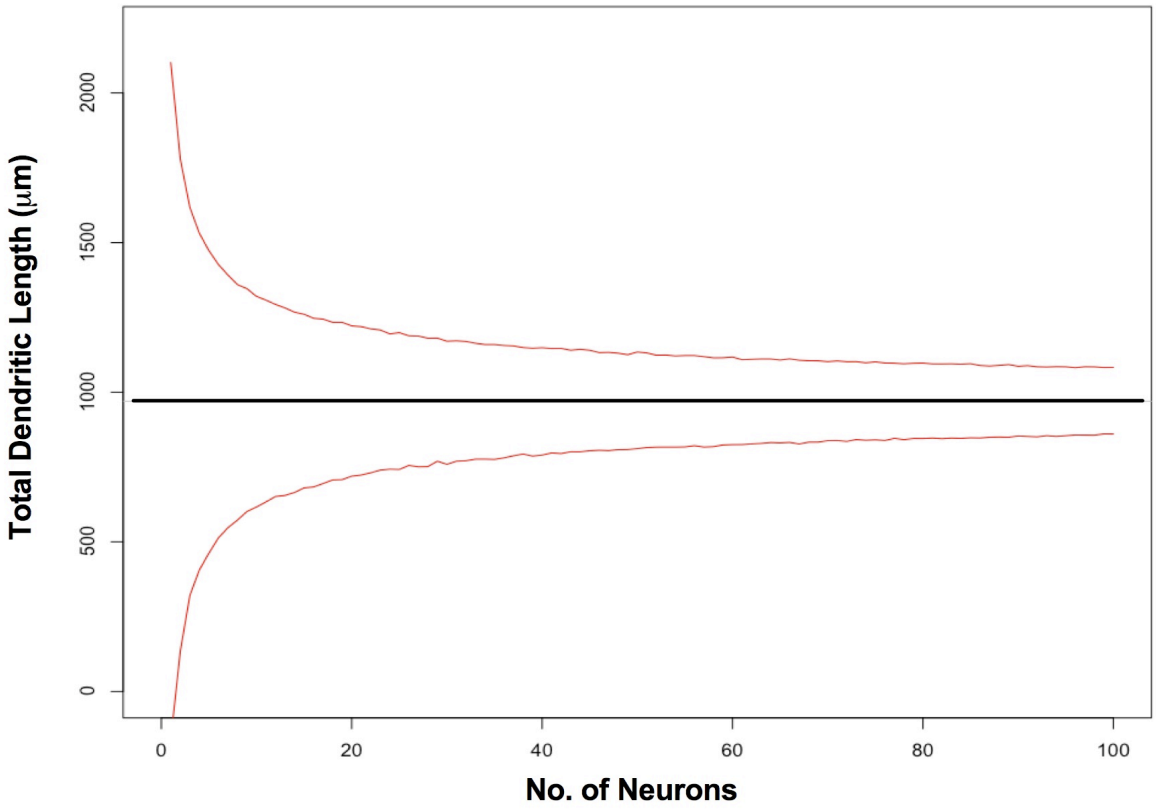

Figure 16. Confidence intervals for mean total basal dendritic length as a function of number of neurons sampled.
Confidence interval calculated by bootstrapping (10,000 iterations) from the pooled total basal dendritic length data from MeCP2 mutant mice (n = 5). Central black line indicates the true mean of the sample and red curves indicate the upper and lower limits of the 95% confidence interval.

This provides an approximation of how sampling error decreases by increasing the neuron sample size within a single animal. The test assumes there is no difference between mice in total basal dendritic length. The dataset had 260 neuron measurements (5 mice x 52 neuron traces / mouse) with mean 969.8 μm ± 573.4 (SD). Only one genotype was examined for the purposes of this example. A bootstrapping loop randomly sampled from 2 to 100 neurons (with replacement) from the pooled data and recorded the mean for each sample size. The sampling was repeated 10,000 times for each sample size, generating a bootstrapped distribution for the sample mean. The 2.5% and 97.5% quantiles of the distribution are reported in the graph. For the particular dataset used in Fig. 16, it is evident that no fewer than 10 neurons should be used to when trying to obtain a reasonable estimate of the mean. Depending on the size of the treatment effect under study, it is also possible to estimate the within-animal sample sizes required to discern that effect. As sampling error increases relative to effect size, more samples within a replicate are necessary to detect the treatment effect. The use of this bootstrapping approach can therefore provide an estimate of sample sizes that represent an appropriate trade-off between accuracy and effort.

If estimates are available for the mean and standard deviation of a parameter from the two treatment groups under study, an alternative approach is to plot statistical power as a function of the permutations of number of animals and number of neurons per animal. Statistical power refers to the probability of not making a false negative or Type II error—i.e., failing to detect a true difference between two populations. The convention is that if no significant difference is detected at 80% power for a given effect size and at a chosen *P*-value, then the populations are considered not different. As an example, if a statistical test detects a significant difference at $P \leq 0.05$ 80% of the time, then we may be confident that a true difference exists between the two populations. Statistical power is therefore a function of the magnitude of the difference to be detected, and can be increased in two ways: by increasing the number of replicates, or by increasing the *P*-value (e.g. from $P \leq 0.05$ to $P \leq 0.1$). Since the latter increases the risk of a Type I (false positive) error, increasing replicates is the only reliable way to increase statistical power. As illustrated in the example in Fig. 17, however, this also raises the question of how

many samples within each animal should be used to ensure a sufficiently precise estimate of the mean value for each animal, without oversampling and performing unnecessary work. Figure 17 shows two different graphical representations of how statistical power varies with different combinations of numbers of animals per genotype and numbers of neurons per animal in the total basal dendritic length datasets. The graphs display the results of an iterative randomization test based on the observed means and standard deviations obtained for both mutant and WT mice.

In this simulation, the data was pooled according to treatment and the sample means and standard deviations were used to randomly generate normal distributions. A one-way ANOVA was then performed with genotype as the predictor variable, and total dendritic length as the response variable. This was repeated for each combination of the number of animals and number of neurons per animal, and repeated 1000X for each genotype. The sample size of mice increased from 2 to 14 per genotype, and the number of neurons measured per mouse varied from 2 to 75. The proportion of times per 1000 iterations in which the ANOVA detected a significant effect of genotype at $P \leq 0.05$ for a given sample size was considered to be the statistical power of the test at that sample size (Crawley, 2007). In Fig. 17A, this is plotted in three dimensions, with the number of mice per genotype and number of neurons per mouse on the x and y axes, and statistical power on the z-axis. Fig. 17B plots the same data as a heat map with red bands representing ≤ 30% power and off-white bands representing 95 – 100% power. Both plots show that proportionally speaking, increasing the number of replicate animals increases statistical power much more rapidly than does increasing the number of neurons per mouse. Interestingly, the graphs also indicate that in order to detect a difference at 80% power, most of the permutations result in a total number of ~300 – 350 neurons—for example, 3 mice per treatment with 50 neurons per mouse or 8 mice per treatment with 20 neurons per mouse. On this basis, the 5 animals per genotype with 52 neurons per animal used in the present study was an unnecessary oversampling beyond what was necessary to detect a difference.

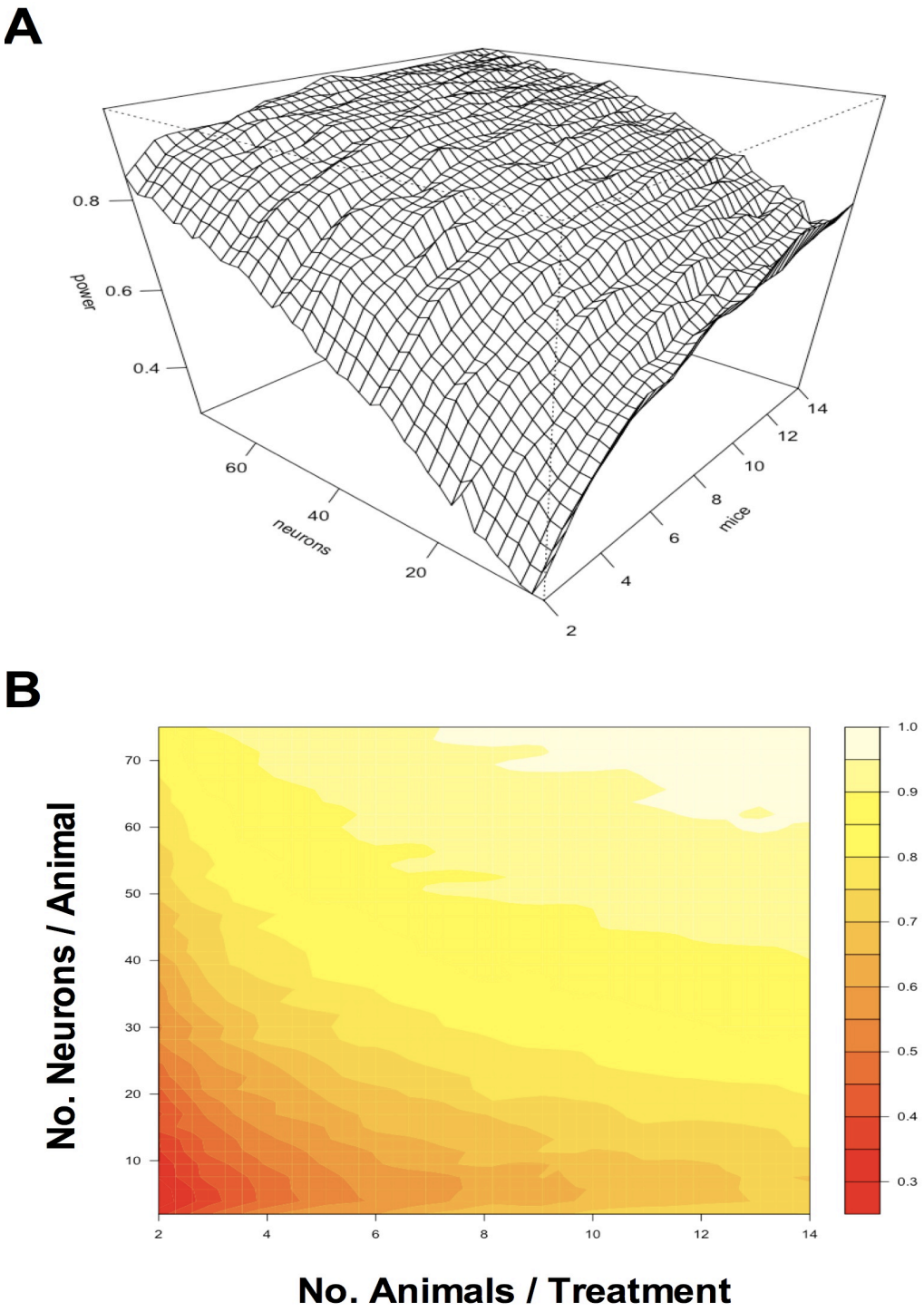

Figure 17. Statistical power from combinations of animals and number of neurons per animal.

A) 3D plot illustrating the relative increase in statistical power for number of neurons per animal vs. number of paired animals across treatments (i.e. genotype). Power increases sharply by increasing the number of animals relative to neurons per animal. B) Heat plot of the same dataset shown in A. Plots used pooled total basal dendritic length data from both mutant and WT mice.

An important shortcoming of the algorithm used to generate these graphs should be noted, which is that it does not take into account any difference in mice within each treatment. All mice in each genotype are sampled from the same distribution, which does not accurately reflect the observed differences between animals. This likely underestimates the effect of increasing the number of animals on statistical power. As such, the R code in Appendix III is presented with the intent that it be subject to further development so that it is better able to represent within-treatment variance.

Appendix II:
R Code for Bootstrapping of Confidence Intervals

```
ch<-numeric()
cl<-numeric()
boot<-numeric()
for(neur in 1:100) {
     for(b in 1:10000) {
     samp<-rnorm(neur,969.8,573.43)
     m<-mean(samp)
     boot[b]<-m
     }
     q<-quantile(boot,c(0.025,.975))
     cl[neur]<-q[1]
     ch[neur]<-q[2]
     }
     n<-seq(1,100)

# graph #
plot(c(0,100),c(0,2200),type="n")
     abline(h=969.8,col="gray")
     lines(ch~n,col=2)
      lines(cl~n,col=2)
```

Appendix III:
R Code for Calculating Statistical Power Using Randomization Tests

```
bootit<-function(mus,neur) {
for (boot in 1:1000) {
mutant<-rep(rnorm(neur,969.8,573.43),mus)
wild<-rep(rnorm(neur,1192.268,582.87),mus)
sim<-c(wild,mutant)
treats<-c(rep(0,length(wild)),rep(1,length(mutant)))
mice<-as.factor(rep(1:neur,each=mus))
set<-data.frame(sim,treats,mice)
model1<-lm(sim ~ treats)
s<-summary(model1)
c<-s$coef
p<-c[2,4]
prob[boot]<-p}
power<-sum(prob<0.05)/1000
return(power)
}


count<-1
prob<-numeric(1000)
pow<-numeric()
sim.mus<-numeric()
sim.neur<-numeric()
for(mus in 2:15){
    for(neur in 2:75){
        b<-bootit(mus,neur)
        pow[count]<-b[1]
        sim.mus[count]<-mus
        sim.neur[count]<-neur
        count<-count+1}
     }
```

Appendix IV:
List of Abbreviations

AA – amino acid

BDNF – brain-derived neurotrophic factor

C.I. – confidence interval

CpG – cytosine – phosphate - guanine

CNS – central nervous system

L*n* (n = 1-6) – cortical layers 1 through 6

MeCP2 – methyl-CpG-binding protein 2

MBD – methyl-DNA binding domain

MRI – magnetic resonance imagine

OMIM – Online Mendelian Inheritance in Man

PEST - proline, glutamate, serine, threonine

RTT – Rett Syndrome (OMIM designation)

TRD – transcriptional repression domain

UTR – untranslated region

WT – wildtype

XCI – random inactivation of the X chromosome

XFP (X = Y, G, C) – yellow, green or cyan fluorescent protein

YHM – YFP-H / MeCP2 hybrid mouse line

Y16M – YFP-16 / MeCP2 hybrid mouse line